Structural and thermal dependence of soft magnetic properties of FeCo-based nanocrystalline materials

Zsolt Gercsi

ENSC-2004 N°17

THESE DE DOCTORAT
DE L'ECOLE NORMALE SUPERIEURE DE CACHAN

Présentée par

Monsieur Zsolt GERCSI

pour obtenir le grade de

DOCTEUR DE L'ECOLE NORMALE SUPERIEURE DE CACHAN

Domaine :
ELECTRONIQUE

Sujet de la thèse :

Influence de la structure et de la temperature sur les propriétés magnétiques douces de matériaux nanostructuré à base de fer et de cobalt

Thèse présentée et soutenue à Cachan le 13 décembre devant le jury composé de :

Jean-Marc GRENECHE	(Directeur de Recherche)	Président, Rapporteur
Manuel VAZQUEZ	(Professeur des Universités)	Rapporteur
Olivier GEOFFROY	(Maître de Conférences)	Examinateur
Frederic MAZALEYRAT	(Maître de Conférences)	Examinateur
Jacques DEGAUQUE	(Professeur des Universités)	Examinateur
Richard BARRUE	(Professeur des Universités)	Directeur de thèse
Lajos K. VARGA	(Directeur de Recherche)	Co-Directeur de thèse

SATIE
ENS CACHAN/CNRS/UMR
61, avenue du Président Wilson, 94235 CACHAN CEDEX (France)

Structural and Thermal Dependence of Soft Magnetic Properties of FeCo-based Nanocrystalline Materials

Thesis by

Zsolt Gercsi

In Partial Fullfillment of the Requirements for the Degree of
Doctor of Philosophy at Ecole Normale Superieure de Cachan
Cachan, France, 2004

Contents

Acknowledgement **3**

Abstract **5**

1 Soft Magnetic Materials **11**
1.1 Iron and silicon steels . . . 11
1.2 Iron-nickel alloys (Permalloys) . . . 11
1.3 Iron-cobalt alloys . . . 12
1.4 Soft spinel ferrites . . . 12
1.5 Amorphous and nanocrystalline alloys . . . 12
1.5.1 Glassy metals . . . 12
1.5.2 Nanocrystalline alloys . . . 15

2 Thermodynamic and transformation kinetics considerations for nanocrystalline soft magnetic alloys **19**
2.1 Types of crystallization (polymorphic, eutectic, primary) . . . 19
2.2 Models of crystallization kinetics . . . 21
2.2.1 Kissinger's model of crystallization kinetics . . . 21
2.2.2 Johnson-Mehl-Avrami model . . . 22
2.3 Avrami exponent . . . 22
2.4 Crystallization of Finemet, Nanoperm and Hitperm type soft magnetic alloys . 23

3 Magnetic properties of nanocrystalline soft magnetic alloys **27**
3.1 Magnetic energies of a ferromagnetic material . . . 27
3.1.1 Zeeman energy . . . 27
3.1.2 Energy of demagnetization field . . . 27
3.1.3 Energy of exchange interaction . . . 28
3.1.4 Magnetocrystalline anisotropy energy . . . 28
3.1.5 Magnetoelastic energy . . . 29
3.2 Magnetic behavior in small structures . . . 29
3.2.1 Superparamagnetism . . . 29
3.2.2 Single domain state . . . 30
3.2.3 Origin of softness of amorphous and nanocrystalline magnetic materials (RAM) . . . 31
3.2.4 Exchange interaction through amorphous matrix (effective exchange stiffness) . . . 33
3.3 Tailoring of hysteresis loop . . . 34
3.3.1 Chemical composition dependence of magnetic energies . . . 34

3.3.2 Tailoring loops by demagnetization factor . . . 35
3.3.3 Tailoring loops by uniaxial induced magnetic anisotropy . . . 35
3.4 Determination of transversal induced magnetic anisotropy . . . 37

4 Experimental Techniques 41
4.1 X-ray diffractometry . . . 41
4.2 Mössbauer spectroscopy . . . 44
4.3 Transmission electron microscopy (TEM) . . . 48
4.4 Vibrating sample magnetometer (VSM) . . . 49
4.5 Small angle magnetization rotation (SAMR) . . . 50
4.6 Hysteresis measurements on single ribbon (single sheet tester) . . . 52
4.7 Low frequency hysteresis measurements as a function of temperature . . . 52
4.8 Faraday Balance . . . 54
4.9 Differential thermal analysis (DTA) . . . 54
4.10 Elongation measurements of soft magnetic ribbons during stress annealing . . . 55

5 Results and Discussion 57
5.1 Crystallization and structure . . . 57
5.1.1 $(Fe_{100-x}Co_x)_{73.5}Si_{13.5}Nb_3B_9Cu_1$ . . . 57
5.1.2 $(Fe_{100-x}Co_x)_{78}Si_9Nb_3B_9Cu_1$ . . . 63
5.1.3 $(Fe_{100-x}Co_x)_{84}Nb_{3.5}Zr_{3.5}B_8Cu_1$ . . . 64
5.2 Magnetic properties . . . 69
5.2.1 $(Fe_{100-x}Co_x)_{73.5}Si_{13.5}Nb_3B_9Cu_1$ . . . 69
5.2.2 $(Fe_{100-x}Co_x)_{78}Si_9Nb_3B_9Cu_1$ . . . 72
5.2.3 $(Fe_{100-x}Co_x)_{84}Nb_{3.5}Zr_{3.5}B_8Cu_1$ . . . 72
5.2.4 Conclusion . . . 73
5.3 Temperature-time evolution of magnetic properties . . . 75
5.3.1 Results . . . 75
5.3.2 Discussion . . . 76
5.3.3 Conclusions . . . 88
5.4 Induced magnetic anisotropy . . . 89
5.4.1 A novel method for determining longitudinally induced anisotropy . . . 89
5.4.2 Results . . . 93
5.4.2.1 Magnetic field induced anisotropy . . . 94
5.4.2.2 Stress induced anisotropy . . . 95
5.4.3 Conclusion . . . 102

6 Conclusions 103

7 Appendices 107

Bibliography 113

Acknowledgement

The work within this thesis has been extensive and trying, but in the first place instructive, exciting and fun. Without help, support, and encouragement from several people, I would never have been able to complete this work.

Most work in the thesis was carried out in the laboratory of SATIE (Système et Applications des Technologies de l'Information et de l'Energie, UMR 8029) at ENS (Ecole Normale Superieure de Cachan) in Cachan, France. Therefore, I would like to thank for Mr. Sylvain Allano, director of SATIE, who gave me opportunity to work in the laboratory.

I am deeply grateful to my supervisor, Mr. Richard Barrué, head of magnetic materials group in SATIE, for his confidence and important support during my work. I have always tried to deserve it.

I owe my most sincere gratitude to my french co-supervisor, Mr. Frédéric Mazaleyrat. Without his patient, long-suffering and extensive discussions whenever I asked him, this work would never have been finished. Thank you.

I wish to express my warm and sincere thanks to my hungarian supervisor, Mr. Lajos K. Varga (Head of Metallurgy and Magnetism Group, Research Institude for Solide State Physics and Optics of Hungarian Academy of Sciences) for his inexhaustible ideas, which always kept the log rolling.

I will also give a special thanks to Mr. Shashank N. Kane for a fruitful collaboration during his 1 year stay in Cachan.

I am grateful to Mr. Francisco Alves, Mr. Fabien Simon and Mr. Yacine Amara who helped me to get over some practical affairs in the beginning of my work, when my French was "rather" poor.

I wish to thank Ms. Angela Quinlan, for revising the English of my manuscript.

The financial support of European Commission GROWTH program, reseach project "HiT-F core, Soft magnetic nanomaterial for high temperature and high frequency functional application in power electronics", contract n° G5RD-CT-2001-03009 is greatefully acknowledged.

Cachan, France, October 2004.

Acknowledgement

Abstract

Structural and magnetic investigations of three families of alloys were carried out, derived from Finemet©(FeSiNbBCu) type [1] and Nanoperm^{TM} type (FeNbBCu) [2] alloys by cobalt addition, which is supposed to increase the thermal stability (higher crystallization and Curie temperature) of the material. The frequency limit can be increased by reducing the effective permeablity as a consequence of transversal induced anisotropies by stress and/or transversal magnetic field annealing, which can preserve the low coercivity (and power loss) of these materials.

In-situ hysteresis measurements during nanocrystallization of various selected alloys is presented and interpreted. These invetigations pointed out that the precipitating nanocrystalline phase can be in different magnetic states during isothermal annealing depending on several parameters. It is determinative whether the amorphous phase is still ferromagnetic or already in paramagnetic state when crystallization occurs.

Simulated results using dipolar interaction modified random anisotropy model [3] are in good agreement with the in-situ measured data demonstrating that the increasing dipole-dipole interaction between nanograins during crystallization can effectively replace the role of exchange interaction in the random anisotropy model [4] averaging out the local magnetocrystalline anisotropy.

An experimental method was developped in order to measure the longitudinally induced anisotropy. This method allows for the first time direct measurement of the longitudinal induced anisotropy in amorphous or nanocrystalline ribbons and wires.

Lastly, the tensile back-stress model is applied to explain the mechanism of stress-induced anisotropy in two-phase nanocrystalline soft magnetic materials. It is pointed out, that the large transverse anisotropy found in $(Fe_{100-x}Co_x)_{73.5}Si_{13.5}Nb_3B_9Cu_1$ x=0 and x=10 alloys results from a combination of the sign of magnetostriction coefficients and stresses, adding the contributions of the two phases.

Keywords: Nanocrystalline; Soft Magnetic; Induced anisotropy; High temperature;

Abstract

Résumé

Nous avons mené des investigations structurales et magnétiques sur les trois familles d'alliages nanocristallins, Finemet, Nanoperm et Hitperm, dans lesquels le cobalt ajouté est supposé accroître la stabilité thermique (température de cristallisation et température Curie plus élevées).

En mesurant les cycles d'hystérésis des différents alliages en temps réel durant la cristallisation, nous avons trouvé que l'état magnétique de la phase nanocristalline est différent en fonction de l'anisotropie locale des nanograins, de leur taille et de leur fraction volumique. Le comportement magnétique global est fortement affecté par le fait que la phase amorphe reste ferromagnétique ou devient paramagnétique lorsque la cristallisation se développe. Alors que la cristallisation du Finemet se produit dans une phase superparamagnétique, nous avons mis en évidence, pour la première fois, la mise en place progressive de l'anisotropie aléatoire au cours de la cristallisation.

Nous avons modélisé le phénomène, à partir de la théorie de l'anisotropie aléatoire, en prenant en compte les interactions dipolaires entre grains. Les résultats de simulation numérique concordent assez bien avec les résultats de mesures, au moins sur le plan qualitatif.

La limite de fréquence peut être augmentée en réduisant la perméabilité effective. Cette diminution peut être le résultat de l'anisotropie transversale induite par un champ magnétique ou une contrainte mécanique appliquée durant le recuit.

Le modèle "back-stress" a été appliqué pour expliquer l'anisotropie induite par la contrainte dans ces alliages biphasés. Nous avons montré que la grande anisotropie mesurée dans les alliages

$(Fe_{100-x}Co_x)_{73.5}Si_{13.5}Nb_3B_9Cu_1$ où x=0 et x=10 est essentiellement due à une combinaison entre le signe du coefficient de magnétostriction et le signe de la contrainte résiduelle (traction ou compression).

Nous avons développé une méthode originale permettant de mesurer l'anisotropie longitudinale induite, qui nous a permis de mesurer directement cette anisotropie dans les rubans et les fils amorphes ou nanocristallins.

Mots clés: Matériaux nanocristalline; Proprieté magnétique doux; L'anisotropie induite; Temperature éléveé;

Introduction

This work is done under the reseach program "HiT-F core, Soft magnetic nanomaterial for high temperature and high frequency functional application in power electronics", in the frame of European Commission GROWTH. This project aimed to develop technology for the production of iron-based amorphous ribbons and nanocrystalline cores. Application of these cores in power electronic devices instead of ferrite or permalloy cores should reduce their weight, overall dimensions, energy consumption, and improve their performance.

The project included basic research into crystallisation process taking place in amorphous ribbons and determination of their magnetic properties, development of technology for the production of amorphous ribbons and nanocrystalline cores, and development of prototype power electronic devices using soft magnetic nanocrystalline cores. The expected results include commercial production of amorphous ribbons, nanocrystalline cores and power electronic devices. Several laboratories, institutes and industrial partners all over Europe were involved in this research project.

My contribution to this project concerns the structural and magnetic investigations of three family of alloys, derived from Finemet ©(FeSiNbBCu) type [1] and Nanoperm^{TM} type (FeNbBCu) [2] alloys by cobalt addition, which is supposed to increase the thermal stability (higher crystallization and Curie temperature) of the material. The frequency limit can be increased by reducing the effective permeablity as a consequence of transversal induced anisotropies by stress and/or transversal magnetic field annealing, which can preserve the low coercivity (and power loss) of these materials.

In order to understand the high temperature behaviour of these materials, the magnetic phase transitions have been studied through the time-temperature dependnece of the hysteresis loop. These magnetic transitions have been simulated taking into account the classical RAM [4, 5] and the newly developped dipolar softening model [3].

This work was carried out in the laboratory SATIE (Système et Applications des Technologies de l'Information et de l'Energie, UMR 8029) in France, partly shared with the Research Institude for Solide State Physics and Optics of Hungarian Academy of Sciences in Hungary.

The structure of this thesis is the following:

- Chapter 1 summarizes the existing soft magnetic materials, with particular attention given to the evolution of amorphous and nanocrystalline materials.
- In chapter 2, basic thermodynamic and transformation kinetics considerations for obtaining amorphous and partially nanocrystallized alloys are presented. Crystallization events in the three families of nanocrystalline alloys are also discussed here.
- Chapter 3, the five fundamental energy terms determining the magnetic properties of a ferromagnetic material are summarized, followed by the explanation of "ultra" soft

behaviours of nanocrystalline alloys (random anisotropy model). Various methods to control systematically the anisotropy term, i.e. tailoring the hysteresis loop, in order to obtain suitable hysteresis properties for the given application are also investigated.

- Chapter 4, presents the various methods used for investigations of both the structural and magnetic properties of present samples.
- in Chapter 5, results and discussions will be presented, particularly:

  ▷ sturcture and magnetic properties of investigated alloys.
  ▷ magnetic behavior of samples during crystallization as a function of various magnetic state of the amorphous and the new precipitating nanocrystalline phases.
  ▷ effective magnetic anisotropy evolution during crystallization in the frame of dipolar interaction extended random anisotropy model.
  ▷ a novel method for obtaining longitudinally induced magnetic anisotropy in ribbons and amorphous wires.
  ▷ interpretation of stress induced magnetic anisotropy results in terms of back-stress theory.

- Finally in Chapter 6, a summary of the main results of the thesis is given.

To the author's knowledge, in-situ hysteresis measurements during nanocrystallization of various selected alloys is firstly presented in this thesis. The interpretation of results taking into account the *interacting* nanoparticles in various magnetic states, helps to better understand the excellent soft magnetic properties of nanocrystalline materials.

1 Soft Magnetic Materials

This chapter summarizes the variety of soft magnetic materials (SMM) in order to reveal the related alloys for the reader. First of all, a clear definition must be given to assign the group of SMM. A very simple but categorical, and therefore easy-applicable definition is given by O'Handley [6]:

"When the magnetization processes (domain wall motion and domain magnetization rotation) occur in weak fields, $H_c \leq 10^3 \frac{A}{m}$ (readily generated by a modest current through a few turns of wire), the material is called a soft magnet."

The materials in this category can be divided into the below mentioned five main groups.

1.1 Iron and silicon steels

Of the three ferromagnetic transition elements only the iron has extensively wide applications. The "pure iron" term is for the minimum 99.8 % purity iron alloys. The pure iron is the most known, "typical" SMM with a very high saturation magnetization (2.2 T) and a relatively low magnetocrystalline ($K_1 = 48 \frac{kJ}{m^3}$) and magnetosriction ($\lambda \sim +5$ ppm for applied magnetic fields $< \sim 40 \frac{kA}{m}$). After casting a hydrogen annealing (750-800°C) is often applied to reduce the high mobility interstitial elements, like carbon, nitrogen and oxygen, in the BCC lattice. These elements are responsible for the well-known metallurgical phenomenon, the *strain-aging*. As a result of aging, the segregated fine particles perturb the preferred form of domain structures and the wall motions. Due to the high purity, its electrical resistivity is very low ($\sim 10 \mu \Omega cm$), hindering the applications at elevated frequencies.

In order to increase the electrical resistivity and to improve the mechanical properties, a small amount of selected elements (substitutional solving) can be added. 4% Si addition increases the electrical resistivity by a factor of 4 and reduces K_1 and λ at the same time, but unfortunately J_s decreases by about 10%. Beyond the 4% limit, the alloy becomes brittle due to the formation of B2 or DO_3 inter-metallic (Fe_3Si) phases. Al addition (Sendust$\Rightarrow \sim$ 85%Fe, Si10%, Al5%) is used to reduce the value of K_1 and λ_s.

1.2 Iron-nickel alloys (Permalloys)

FCC ($FeNi_3$) lattice is formed in the range from 35% to 100% Ni. K_1 has a strong dependence on the rate of ordering. The high value of K_1 if $FeNi_3$ is ordered, can be compensated by field induced anisotropy (K_U).

This group has four major compositions of technical interest:

- 78% nickel permalloy (Supermalloy). K_1 and λ pass through zero near this composition. This alloy exhibits high initial permeability and is used in differential transformers.

- 65% nickel permalloy. Sensitive for magnetic field annealing, so various loop shapes can be achieved.
- 50% nickel permalloy (Deltamax). Higher, J_s=1.6T saturation, and strong response to field annealing. Used for small motors (watches, etc.).
- 36% nickel permalloy (Invar). Its thermal dilatation is exactly compensated by volume magnetostriction. Used for metrological applications.

1.3 Iron-cobalt alloys

The equiatomic FeCo alloys (BCC), called Permendur, has very high magnetic saturation (J_s=2.4T!) and a relatively low magnetic anisotropy, $K_1 = -10^4 \frac{J}{m^3}$, in disordered state. In the ordered (CsCl) phase, K_1 is close to zero. The order-disorder transition is about 730°C, so the magnetic properties depend on the annealing temperatures and on cooling rate. Addition of 2% vanadium (Hiperco) can increase the laminability during production, at the same time it decreases the high magnetostriction ($\lambda \sim 60\,ppm$) and increases the electrical resistivity (from $10\mu\Omega cm$ to $40\mu\Omega cm$). These alloys are used in generators and transformers, where high magnetic flux density is more important than loss or cost (e.g. aircrafts).

1.4 Soft spinel ferrites

The soft ferrites can still offer some great advantages in magnetic properties. The electrical resistivity is five - fifteen orders of magnitude higher than that of metallic SMM. This is a very important parameter for high frequency applications (eddy current). The other notable advantage is the high corrosion resistance. However, ferrites have serious disadvantages too, such as low Curie temperature, low magnetic saturation and poor mechanical properties. The ferrites are based on the spinel structure of Fe_3O_4. The two most common soft spinel ferrite families are the manganese-zinc and nickel-zinc ferrites:

$$(Fe^{3+})_A(T^{2+}Fe^{3+})_BO_4$$

where T is a transition metal, Mn or Ni. The Zn^{2+}can form a tetrahedral coordination more easily than Fe^{3+}. With more Fe^{3+}at this sublattice, which represents a higher local magnetic moment, the magnetic moment per cell will also increases. The magnetic coupling in ferrites is due to the *superexchange* interaction.

1.5 Amorphous and nanocrystalline alloys

1.5.1 Glassy metals

The first metallic glass was made by KRAMER [7] in 1934. This was based on chemical vapour deposition. In 1946, Brenner and Riddel fistly observed noncrystalline metallic structure on NiP electrodeposits [8]. The great breakthrough happened in 1960, when DUWEZ and his coworkers discovered a method preparing amorphous metals by direct quenching from the melt [9]. In this technique a drop of molten metal was projected to a cold substrate. During the same period, MIROSHNINENKO and SALLI [10] presented a setup for preparing amorphous

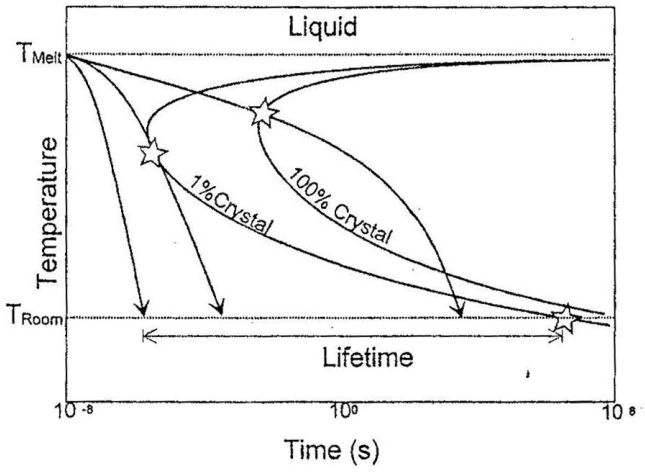

Figure 1.1: TTT diagram (after [13])

alloys. In this setup (splat-cooling) the molten metal alloy drop was rapidly flattened on to a cold surface. By this method very large cooling rates (over million degrees per second) can be reached, yielding a completely new, *highly supersaturated solid solution*. Finally, this idea helped POND and MADDIN [11] to invent the first device to prepare continuous long ribbons. This setup proved that these materials can be manufactured in industrial quantities and can be profitable for commercial exploitation.

From the theoretical side, it was believed for years that ferromagnetism could not exist in amorphous state because of the lack of atomic ordering. In 1960, GUBANOV [12] predicted that in ferromagnetism the short-range order plays the dominant role and not the longer-range one, so the glassy metals can be ferromagnetic.

The vitreous state is approached as an extension of the liquid state, with solid aspects. Generally it can be said that, all the alloys can exist in vitreous state if the cooling rate ($\dot{T}$) is fast enough to freeze the topological disordered substance. The TTT (time, temperature, transition) diagram can illustrate the crystallized phase fraction (see Fig.1.1). The cooling rate must not cross the 1% crystallized phase fraction line to obtain a fully amorphous metal. Although the driving force for nucleation increases dramatically with the dropping temperature, the mobility of atoms decreases even faster, therefore the diffusion controlled nucleation can not succeed at low temperature.

The glass-transition temperature (T_g) is a characteristic parameter of the amorphous metals. Above this temperature, the glass is in the so-called *supercooled-liquid state*, where it behaves mechanically like a very viscous liquid up to the crystallization temperature (T_x). At T_g, the temperature dependence of enthalpy (H) starts to increase discontinuously and the specific heat (C_p) also has a break on the temperature dependence (Fig.1.2).

The most important parameter in the metallurgy of amorphous alloys is the glass forming ability (GFA), which gives information about the willingness of vitrification in the given alloy. The smaller the gap between liquidus temperature T_l and T_g, the higher the GFA, because the probability of crystallization is smaller during overcooling. The ratio $\frac{T_g}{T_l}$, called reduced glass temperature (T_{rg}), is about 0.45 generally, but in some cases it can reach the value of 0.69 [14].

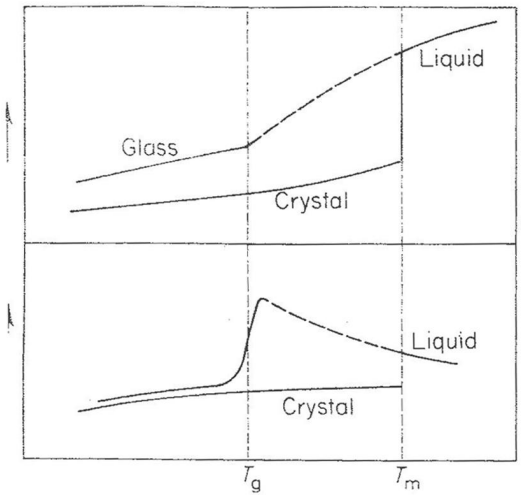

Figure 1.2: The temperature dependence of enthalpy (upper box) and specific heat in glassy metals (after [14]).

The amorphous alloys can also be categorized by their physical extents. Of course this extent depends on the GFA of the given composition. From this characteristic, we must distinguish the following families of amorphous alloys:

Bulk Amorphous Alloys (>100μm)
The material can be considered as bulk when its thickness exceeds $100\mu m$. The first ferromagnetic bulk amorphous alloy was produced by Inoue et. al. [15, 16] in 1995. The large supercooled-liquid region (50-90K) is responsible for this high glass forming ability (GFA). The three empirical rules, proposed by Inoue [15], must be kept in order to obtain bulk glassy metals:

- The multicomponent alloy system must contain more than 3 elements.
- Significant difference in atomic size ratios above $\sim$ 12% among the main three elements.
- Some elements must have negative heat of mixing with the main ferromagnetic metal.

From the composition point of view, we distinguish two groups [13]:

- $Fe_{74-80}LM_{0-6}NM_{20}$ with LM (late metall) = Al,Ga and NM (non-metal) = B,P,Si,C.
- $Fe_{55-60}B_{15-20}FM_{8-14}EM_{10-17}$ with FM (ferromagnetic metal) = Co,Ni and EM (early transition metal) = Zr,Mo,Nb,Ta,W,Hf.

Bulk amorphous alloys should be produced by melt-spinning to obtain ribbon form with a well-controlled thickness of 25-200μm. In some cases, where the supercooled liquid region is large enough ($\sim 90K$), the simple copper mold-cast is a possible method of producing bulk glasses. 2-6 mm (!) thickness can be reached without any sign of crystallization. This large value of thickness corresponds to a quite low cooling rate ($< 10^{-2}\frac{K}{s}$).

Ribbons (<100μm)

For the ferromagnetic ribbons, the supercooled liquid region is much smaller than the bulk ones ($\sim 10K$). The magnetic properties have higher priorities than the large GFA in terms of design because by melt-spinning technique even $\dot{T} = 10^6 \frac{K}{s}$ can be achieved. Evidently, the composition must be optimized for lower $\dot{T}$, which means smaller residual stress after quenching and also necessary for industrial production in air.

In the industry, three families of produced ribbons have evolved since 1970s:

- Iron-based alloys containing 74-80% Fe, 15-20% B and Si with a few percentage of C and Cr.
- Cobalt-based alloys composed of 65-75% Co, 10-15% B, 5-15% Si and a small percentage of several element such as Fe, Ni, Mo, Mn.
- Iron-Nickel alloys made of about 80% Fe and Ni, 15-18% of B and other elements such as Mo, Si.

Amorphous wires (50-200μm)

The wires are manufactured from molten alloy being blown into a wheel, filled with water, from a circular cross-sectioned nozzle (in-rotation water spinning). The resulting filament has a quasi-circular cross-section but due to the small heat conductivity of water the obtained wires are not completly amorphous but partially crystallized.

Glass covered amorphous microwires (3-30μm)

The manufacturing process of microwires consists of melting the alloy in a glass nozzle at a high temperature in order to melt the nozzle together with the alloy. The filament is stretched under a water jet, thus a cylindrical wire with diameter of 3 to 30 μm is obtained. The glass coat around the amorphous alloy has a thickness of 1 to 15 μm. This process produces wires in a large range of composition, which otherwise could not be obtained in amorphous state by the above mentioned methods.

Thin layers

Another important group of soft magnetic material must also be mentioned, namely the thin magnetic films. In these materials, the fundamental magnetic properties are linked to the local enviromental, which can be different on the surface as compared to bulk (for instance the lattice parameter is usually smaller near surface). These materials can be produced by sputtering , where the impact of an accelerated atom or ion on a surface produces sputtering from the surface as a result of the momentum transfer from the in-coming particle. Unlike many other vapour phase techniques there is no melting of the material. This technique permits metastable amorphous materials to be obtained, which could not be cast by melt spinning method such as oxides.

1.5.2 Nanocrystalline alloys

For about 30 years, from the early sixties until the late eighties an extremely large variation of compositions, sample preparation techniques and annealing methods were developed and investigated to improve the soft magnetic properties. This aim seemed to be successfully achieved (see chapter above) in the mid 80's and therefore the number of new develpments

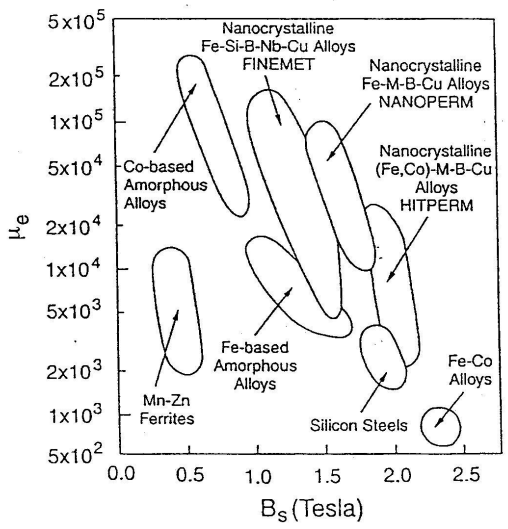

Figure 1.3: The relation between permeability (at 1kHz) and saturation polarization for soft magnetic materials (after [17]).

decreased in the mid 80's. Looking back on this period, it can be seen that further evolution was delayed by the amorphous structure.

Due to very fast casting process the frozen glass structure is far from the thermodynamic equilibrium state. The amorphous material always endeavors to reach the most stable state possible, by diffusion of atoms. Generally, the transformed fraction (V) can be expressed by the Avrami equation:

$$V = 1 - e^{(-Kt^n)}. \tag{1.1}$$

K is a temperature dependent parameter, n can vary from 1 to 4 depending on the statistical model of crystallization. The endeavour to obtain partially crystallized structure was led by the desire to stabilize the magnetic properties (which corresponds to the structure) for elevated temperatures. The other consideration was to minimize the magnetostriction creating a two phase system where the magnetostriction values cancel each other resulting almost zero global magnetostriction.

Preliminary efforts to obtain a partial crystallized structure were unsuccessfull [18]. For the very first time, a nanocrystalline soft magnetic material was reported in the work of Y. YOSHIZAWA et. al. in 1988 [1]. This discovery introduced a new family of SMM and gave a new impetus to its research. The new composition was named FINEMET (trademark) and the composition is derivated from Fe-Si-B amorphous alloys. In Hitachi Metals Lab, hundreds of compositions were made and measured to obtain "the smoothest" structure and magnetic properties. The original composition $Fe_{73.5}Si_{13.5}Nb_3B_9Cu_1$ is worldwide patented. The heat treatment (540°C, 1h) results in nanocrystalline structure (12nm) in the residual amorphous matrix. The SMM properties of this composite are very impressive: Hc=0.53 A/m, $\mu = 100.000$ at 1kHz, T_c=573°C and $B_s = 1.24T$. The Si content of the precipitated grain is around 18-20 at% Si (at saturation) in the DO_3 superstructure.

In 1991, K. SUZUKI et. al. investigated an other type of nanocrystalline alloys, called

NANOPERM (Fe-Zr-B-Cu) [2, 19]. Due to the lack of Si and greater amount of Fe ($\sim 85\%$) as compared to Finemet, higher saturation magnetization is reached (1.5-1.7T). The nanograins have $\alpha - Fe$ structure with an average size of 10 nm.

Most recently M. A. WILLARD et. al. presented a high Co content nanocrystalline alloy, denominated HITPERM [20, 21]. $(Fe_{0.5}Co_{0.5})_{88}Zr_7B_4Cu_1$ alloy was directly derived from the Nanoperm, made with the aim to improve the high temperature magnetic properties. This goal was successfully achieved and the highest induction SMM (at elevated temperature B_s>1T at 500°C) was obtained. The most important characteristic properties of these materials are summarized in Table 7.1.

The soft magnetic alloys can be classified by their saturation polarization and permeability in order to consider them in a different manner (after [17]). This kind of summary enables the different material for a given application to be chosen at the design state. The crystallization processes of these alloys are detailed in Sec. 2.4.

2 Thermodynamic and transformation kinetics considerations for nanocrystalline soft magnetic alloys

The thermodynamic properties of magnetic amorphous and nanocrystalline alloys are important for different reasons. Since the excellent magnetic properties are related to the two phase structure, the crystallization kinetics account for the microstructure, i.e. the amount and size of the nanocrystallites, within the amorphous matrix. The developing microstructure depends on several parameters, such as the diffusion coefficients, the probability of nucleation sites, the free energy difference between amorphous and possible crystalline phases and the thermal history of alloy. The residual amorphous phase is in a metastable thermodynamic state, so it always tries to transform to a more stable crystalline state. In order to choose the proper chemical composition, all these parameters must be considered, because the magnetic properties are connected to the physical structure.

The beginning of this chapter will describe the possible crystallization modes in these alloys: primary, polymorphic and eutectic crystallization. The willingness of crystallization and its driving force will be explained by free energy diagrams. Later sections give a review of the common crystallization kinetic models used to analyze the time evolution of transformed fractions, such as Kissinger [22, 23] or Johnson-Mehl-Avrami model (JMA). Finally, the related alloys such as Finemet, Nanoperm and Hitperm will be discussed by the concerning studies found in the literature.

2.1 Types of crystallization (polymorphic, eutectic, primary)

In the classical metallurgical terminology, the "crystallization" expression is used for the processes when the liquid metal solidifies from the melt. At this point, the quantitative properties of that metal change drastically in a very limited timescale. For the cases when the changes take place in the solid material, the terminology should be "transformation". Nevertheless in the amorphous metals, there is no long range order i.e. the liquid structure is frozen in due to the extremely high cooling rate. From this point of view the changes in the glassy metals can be called "crystallization".

In metallic glasses the driving force for crystallization is the free energy difference between the glass and the new forming phase. The crystallization can be either *interface controlled*, which means the rate of transfer of atoms across the advancing interface is limited, or *diffusion controlled* so that the rate of diffusion of atoms are towards or away from the growing phase is narrow. To date all the evidence shows that the crystallization of glassy metals is diffusion controlled. Fig. 2.1 shows an hypothetical free energy [25] diagram to interpret the possible devitrification reaction in these systems at a chosen (annealing) temperature. The G curve

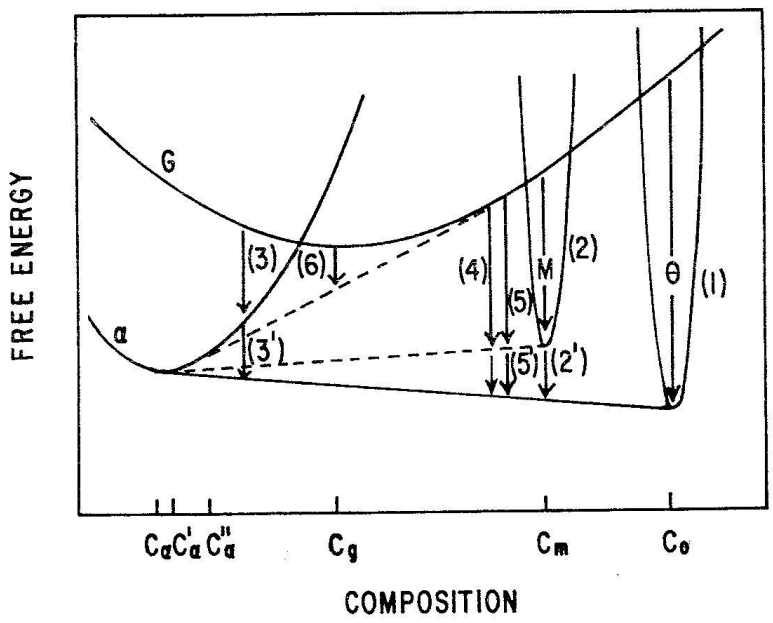

Figure 2.1: Schematic free energy curves to describe the types of crystallization in amorphous alloys (after [24]). The solid lines represent the stable equilibrium, the dashed ones show the metastable states.

corresponds to the glass, assuming that the amorphous phase is metastable, so its curve is always above the stable crystalline ones. In this figure two stable phases are included: an intermetallic θ and a solid solution α. Also a metastable (M) phase can exist, denoting a lower free energy than that of the glass, with respects to the equilibrium mixture of α and θ. It can co-exist in metastable equilibrium with α of composition c'_α, determined by the connected line of tangent points of α and M curves. The possible types of devitrification are the polymorph, eutectic and primary crystallization.

In the case of *polymorphous crystallization* there is no composition difference between the original phase and the developing new phase. The new composition can be a supersaturated solid solution (α) or a metastable compound (θ, M) representing a lower free energy than that of original phase (see Fig. 2.1). In the reaction front, the concentration is similar to the new compound. Polymorphous crystallization of the α phase is indicated by the arrow labeled 3. Further on, the crystallization can be finished reaching the equilibrium state (c_α,c_θ) indicated by arrow 3'. The metastable M phase can be in metastable equilibrium with α ($c_{\alpha'}$,c_M) but the system endeavors to further transform to the stable equilibrium state (c_α,c_θ), see the arrow labeled 2'.

As for *primary crystallization*, arrow labeled 6 shows the crystallization from the glass of α supersaturated solid solution. The concentrations ($c_{\alpha''}$,$c_{res.g.}$) can be obtained by the common tangential line of their free energy curves (see the dashed line corresponding to 6 in Fig.2.1).

The third mechanism of crystallization of glassy metals is the *eutectic crystallization* when the glass reduces its free energy growing two crystalline phases in a coupled way. (In the classic terminology it should be named *eutectoid* reaction since it occurs entirely within the solid state.) The glass can crystallize to the metastable equilibrium state of $\alpha(c_{\alpha'})$ and M(c_M)

indicated by arrow 5 in Fig. 2.1. Latter crystallization to the stable state (5') can occurr. Eutectic crystallization can lead directly to stable thermodynamic state (4) forming the glass with concentrations of c_α and c_θ, respectively, as is shown by arrow labeled 4. Either the way labeled 4 or 5 will be realized, the crystallized two phase system will have a unique texture due to the common crystallization of two phases.

2.2 Models of crystallization kinetics

The free energy diagrams take account of the reaction paths for crystallization as a function of chemistry, but the rate of crystallization is still unknown using only these curves although the magnitude of free energy differences (ΔG) -which is the driving force of crystallization- can refer indirectly to the measure of reaction. To understand the rate of reaction, at which these crystallizations proceed, is also a very important factor. In the following sections the crystallization kinetic models for constant heating rate and isothermal treatments are interpreted.

2.2.1 Kissinger's model of crystallization kinetics

The Kissinger model describes the crystallization kinetics in the condition of continuous heating. The Kissinger equation is:

$$ln(\frac{\phi}{T_p^2}) = -\frac{Q_K}{RT_p} + const. \tag{2.1}$$

where ϕ is the heating rate, T_P is the temperature value of the peak in Kelvin (given from DSC), Q_K is the activation energy and R is the ideal gas constant. In the first model of Kissinger in 1956 [22] T_P was dependent on the heating rate (ϕ) and that was used to determinate activation energy (Q_K) using different heating rates for first order reactions. Later on, he extended the model for more general cases, i.e. reactions of any order [23].

Eq.2.1 was derived from the following reaction rate expression:

$$\frac{dx}{dt} = k_K^0(1-x)^{n_K} e^{\frac{-Q_K}{RT_P}} \tag{2.2}$$

where $\frac{dx}{dt}$ is the reaction rate, x is the fraction reacted and n_K (K index is to distinguish from Avrami exponent used in JMA, see Section 2.2.2) the empirical order of reaction. This function has a maximum and returns to zero indicating the end of the reaction. The value of $\frac{dx}{dt}$ is equal to zero when the reaction rate reaches a maximum. If the temperature increases at a constant rate (ϕ) Eq. 2.2 can be written as the following:

$$0 = \frac{Q_K\phi}{RT_P^2} - k_K^0 n(1-x)^{n_K-1} e^{\frac{-Q_K}{RT_P}}. \tag{2.3}$$

Small quantities can be neglected substituting 1 for $n(1-x)^{n_K-1}$. Moreover after differentiation of Eq. 2.3, the final form of Kissinger's equation is given as:

$$\frac{d(ln\frac{\phi}{T_P^2})}{d(\frac{1}{T_P})} = -\frac{Q_K}{R}. \tag{2.4}$$

The activation energy Q_K can be determined by taking the differential thermal analysis curves at different heating rates.

2.2.2 Johnson-Mehl-Avrami model

In the Johnson-Mehl-Avrami (JMA) model, crystallization kinetics are discussed in isothermal conditions. The model can be applied for crystallization processes, assuming that the following conditions are satisfied:

- Isothermal crystallization, i.e. nucleation and growth occur at a constant temperature
- Crystal growth is isotropic until they are not reached by each other
- The activation energy of crystallization is independent on temperature and time
- Nucleation is random overall the bulk of the sample which is supposed to be infinitie

The volume fraction transformed during crystallization is given as:

$$x(t) = 1 - exp\left[-(kt)^n\right], \tag{2.5}$$

where x is the volume fraction transformed as a function of time (t), k is the rate constant and n is the so called morphology index. The value of that morphology index (n) gives information about the dimensionality. The rate constant k can be written:

$$k(T) = k^0_{JMA} e^{(\frac{-Q_{JMA}}{RT})} \tag{2.6}$$

in which k^0_{JMA} is the rate constant and Q_{JMA} is the activation energy. In order to calculate the value of Q_{JMA} it is conventional to rearrange Eq. 2.5 into an Arrhenius type equation, such as:

$$\frac{1}{t_1} - \frac{1}{t_2} \approx \frac{-Q_{JMA}}{R} e^{(\frac{1}{T_1} - \frac{1}{T_2})}, \tag{2.7}$$

where $t_1$and t_2 are the times needed to transform by a certain amount at temperature T_1 and T_2, respectively. This model is valid for linear rate growth where the crystallization rate is constant and for cases of diffusion controlled growth. The Avrami exponent (n) has been found to be constant over a substantial range of temperature.

2.3 Avrami exponent

The exponent (n) provides information about the nucleation and growth process. For instance n=3 if all nuclei are present at t=0 and the particles grow in a constant rate with a spherical shape. On the other hand, if all nuclei are already present at t=0 but growth of the spherical crystalline particles is parabolic, then the time exponent n=3/2 is expected.

Johnson and Mehl treated the problem and gave a general expression for growth exponent of particles:

$$n = p + q \tag{2.8}$$

Nucleation Type	Growth Geometry	n for chemical reaction (linear)	n for diffusion (parabolic)
Instantaneous Nucleation Site Saturation	Bulk 1-D growth	1	1/2
	Bulk 2-D growth	2	1
	Bulk 3-D growth	3	3/2
Homogeneous Nucleation Constant Rate	Bulk 1-D growth	2	3/2
	Bulk 2-D growth	3	2
	Bulk 3-D growth	4	5/2
Decreasing Nucleation Rate	(n-1)<n_{dec}<n		
Heterogeneous Nucleation	(n-1)<n_{het}<n		
Increasing Nucleation Rate	n<n_{inc}<(n+1)		

Table 2.1: Nucleation types, growth geometries and mechanisms with the corresponding Avrami exponents (after [26])

In this expression p=0 when the nucleation is immediate, p=1 for constant nucleation with time, q=3/2 for parabolic growth of spherical particles and q=3 for linear crystal growth. Thus, constant random nucleation with a parabolic growth of spherical particles results in a value of n=5/2. The fastest nucleation occurs (n=4), when the nucleation is immediate and the rate of growth is parabolic. Other values of n are possible as well, for instance when the growth is not spherical but oriented in preferred directions.

By this consideration, the fitted values (n) of experimental curves describe the kinetics quantitatively. The possible nucleation types, growth mechanisms and geometries correspond to morphology index (n) is summarized in Tab. 2.1.

2.4 Crystallization of Finemet, Nanoperm and Hitperm type soft magnetic alloys

This section tries to review the structural properties of the relevant family of alloys. Crystallization mechanism, the precipitated phases, the morphology and microstructural changes are summarized from related publications.

- FINEMET ($Fe_{73.5}Si_{13.5}Nb_3B_9Cu_1$)

The first time Cu and Nb were added to Fe-Si-B alloys to investigate the development of a new type Fe-based soft magnetic alloys by Yoshizawa et al. in 1988 [1]. A ferromagnetic alloy system of $Fe_{74.5-x}Si_{13.5}Nb_3B_9Cu_x$ with x=0, 0.5 ,1 ,1.5 was annealed at different temperatures to optimize the magnetic properties. The annealing temperatures were determined by DSC method. They observed the smallest coercive field (0.53A/m) and highest permeability ($\sim$ 100000) in the samples, where the Cu content was 1 at% and the annealing temperature was 823 K. The lattice parameter was given about 2.84Å by XRD, which is smaller than that of the pure bcc Fe. The Cu was supposed to be the responsible of the fine structure (10-12 nm), due to its tendency of segregation from the Fe and the nucleating effect. The role of Cu in the very first stage of crystallization was cleared up by Hono et al. [27, 28]. The following stages of crystallization were observed (after [17]):

1. The initial precursor material is fully amorphous
2. At the initial stages of crystallization, Cu enriched clusters of a few nm in size form
3. $\alpha - FeSi$ nucleates at the site of incipient Cu clustering
4. $\alpha - FeSi$ nanocrystals grow while expelling Nb, B and Cu to the inter-granular amorphous phase
5. The expelled Cu atoms are again active nucleating agents. New copper clusters form, go to 3.

MÜLLER et al. [29] studied the effect of Si in Finemet type (FeSiNbBCu) amorphous alloys. They observed that in alloys Si < 12 % the precipitated phase is Fe-Si solid solution and for the cases where Si > 12 % ordered superstructure of DO_3 was observed. NOH et al. [30] have investigated the influence of B substitution for Si in $Fe_{73.5}(B_{100-x}Si_x)_{22.5}Nb_3Cu_1$ alloys. The B addition led to the nanocrystallization of two different phases: the first $\alpha - FeSi$ with a high Curie temperature and the second interfacial B-rich with a lower Curie temperature. KULIK et al. [31] have also studied the B substitutions for Si in $Fe_{73.5}Si_{22-x}B_xNb_3Cu_1$ composition. The softest magnetic properties were observed in the alloys where primary crystallization of $\alpha - FeSi$ was occurred. The secondary crystallization of Fe_2B leads to the hardening of magnetic properties. ZHANG et al. [32] have studied the developing and transformation to DO_3 superstructure of $\alpha - FeSi$ nanocrystals by XRD. They observed that the BCC structured FeSi phase starts to crystallize at 490°C and transforming to DO_3 progressively. The Curie temperature of amorphous phase is $\sim 325°C$ while the nanocrystalline one is 600°C. At 590°C nearly all the nanocrystallites have ordered superstructure in the alloy. The crystallization stages in Finemet, as the temperature increases are the following:

$$Amorphous \Rightarrow \alpha - FeSi + amorphous' \ (470°C) \Rightarrow FeSi(DO_3) + amorphous' \ (490°C) \Rightarrow FeSi(DO_3) + Fe_2B + Fe_3B \ (620°C)$$

- NANOPERM ($Fe_{86}Zr_7B_6Cu_1$)

SUZUKI et al. [2, 19] have investigated the magnetic properties and microstructure after crystallization of $Fe_{86}Zr_7B_6Cu_1$ amorphous alloy. The resulting nanostructure had a grain size of BCC Fe about 10-12 nm after annealing for 1h in a wide annealing temperature range of 500-650°C. The grain size of precipitated nanophase depends very little on T_a in this temperature range. The crystallization reactions have been identified as:

$$Amorphous \Rightarrow \alpha - Fe + amorphous' \ (504°C) \Rightarrow \alpha - Fe + Fe_3Zr + X' \ (747°C) \Rightarrow \alpha - Fe + Fe_2Zr + Fe_3Zr + ZrB_2 \ (877°C)$$

The primary crystallization starts at $\sim 504°C$ with the developing of pure Fe from the amorphous precursor. It is followed by secondary crystallization of the Fe_3Zr and an unknown X labeled phase at 747°C. At elevated temperature (877°C) new phases appeared such as Fe_2Zr and the refractory ZrB_2.

ZHANG et al. [33] have concluded (after the structural studies of $Fe_{90}Zr_7B_3$) that the initial crystallization step of Nanoperm proceeds by the expulsion of Zr from the $\alpha - Fe$

nanocrystals to the B and Zr rich residual amorphous matrix. The role of Cu as nucleation agent is still questionable in these alloys. ZHANG et al. [33] have tried to add Si to the Nanoperm type alloys to obtain nanocrystalline Fe-Si grains. They showed that the Si is expelled from $\alpha - Fe$ to the amorphous matrix and FeSi particles did not occur. This is explained by the difference between the enthalpy of mixing (ΔH_{mix}). For FeSi ΔH_{mix}= -9.423 kcal/mol while for ZrSi this value is -18.5 kcal/mol, thus the ZrSi interaction is preferable for Si than FeSi.

- HITPERM ($Fe_{44}Co_{44}Zr_7B_4Cu_1$)

WILLARD et al. [20, 21] have determined the crystallization stages and temperatures of Hitperm alloy using differential scanning calorimetry and X-ray investigations. In $Fe_{44}Co_{44}Zr_7B_4Cu_1$ alloy a two-stage crystallization was observed [17]:

$$Amorphous \Rightarrow Amorphous' + \alpha' - FeCo\,(510°C) \Rightarrow FeCo - B2 + (FeCo)_3Zr\,(700°C)$$

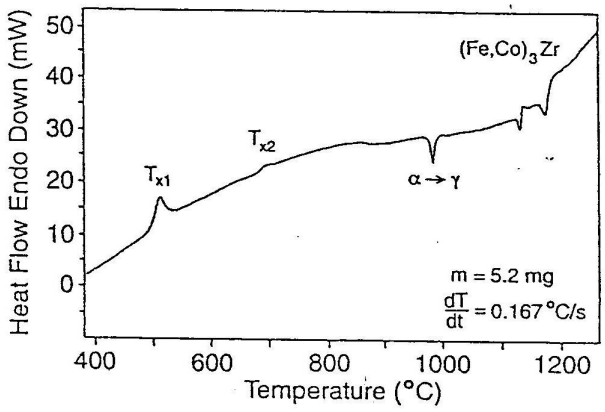

Figure 2.2: Differential thermal analysis plot (DTA) of $Fe_{44}Co_{44}Zr_7B_4Cu_1$ Hitperm alloy (after [17])

The $\alpha' - FeCo$ consists of B2-body centered superlatticed crystallites. Second crystallization of $(Fe, Co)_3Zr$ occurs at 700°C. The primary crystallization of $\alpha' - FeCo$ occurs from the still ferromagnetic amorphous phase due to the high amount of Co. (It is not the case for Finemet.) The nanocrystallized Hitperm alloy exhibits a very impressive magnetic saturation as a function of temperature: only at 980°C the magnetization drops to zero due to the allotropie transformation of nanocrystalline phase ($\alpha \Rightarrow \gamma$). Fig. 2.2 (after [20, 21]) shows the DTA curve marks the crystallization events which occurs as a function of temperature in Hitperm.

3 Magnetic properties of nanocrystalline soft magnetic alloys

3.1 Magnetic energies of a ferromagnetic material

The form of hysteresis curves testifies the domain structure and the magnetic processes by which the material always tries to minimize its free enthalpy (Φ). Micro-magnetic free enthalpy density ($\Phi' = \frac{\partial \Phi}{\partial V}$) of a unit volume is composed by the 5 following parts:

$$\Phi' = \Phi'_{ef} + \Phi'_{dm} + \Phi'_{ex} + \Phi'_{k} + \Phi'_{ml}, \tag{3.1}$$

where Φ'_{ef} is the external field energy density or rather Zeeman energy density, Φ'_{dm} is the demagnetization energy density, Φ'_{ex} is exchange energy density, Φ'_{k} is magnetocrystalline anisotropy energy density and Φ'_{ml} is the magnetoelastic energy density.

Nature always tries to minimize the free enthalpy, thus domain structure is always created in such a way as to minimize the magnetic free enthalpy ($\Phi = \int \Phi' dV$) in the material.

3.1.1 Zeeman energy

Zeeman energy density describes the relation between magnetization of a ferromagnetic material ($\overrightarrow{M}$) with an applied external magnetic field ($\overrightarrow{H_{ext}}$):

$$\Phi'_{ef} = -\overrightarrow{H_{ext}} \times \overrightarrow{J},$$

where $\overrightarrow{J} = \mu_0 \overrightarrow{M}$ is the magnetic polarization. Φ'_{ef} is minimal when the magnetization is parallel with the applied external field.

3.1.2 Energy of demagnetization field

Energy density of demagnetization field (Φ'_{dm}) can be written as

$$\Phi'_{dm} = -\overrightarrow{\frac{1}{2} H_s} \times \overrightarrow{J},$$

where $\overrightarrow{H_s}$ is the external magnetic field $\overrightarrow{H_s} = NH_{ext}$ and N is the demagnetizing factor (tensor) whose value is a function of position and magnetization orientation inside the sample. The value of $\frac{1}{2}$ is reduced when domain structure is formed.

3.1.3 Energy of exchange interaction

Exchange interaction, thus exchange energy (Φ'_{ex}) is the real origin of ordered spin structure, i.e. of the ferromagnetic phenomena. As it is well known from Pauli's exclusion principle, two fermions cannot fill the same quantum mechanical state. Consequently two electrons with parallel spin try to escape each other while two electrons with anti-paralell spin are willing to approach each other. The electrostatic Coulomb energy is smaller for parallel ordered spins compared to anti-parallel ones. This energy difference is called exchange energy. It must be emphasised that the exchange interaction is an electrostatic phenomenon and not an interaction between magnetic moments of electrons. At the same time, the parallel configuration of electron spins represents a higher kinetic energy which exceeds the benefits of smaller Coulomb energy, thus there are only 4 pure elements that show ferromagnetic behavior (at room temperature): Fe, Co, Ni and Gd.

Exchange energy density can be deduced from the gradient (∇) of directional cosine (γ_i,where i=1,2,3) of spontaneous magnetization of material ($\overrightarrow{M_S}$). Expressing the $\Phi'_{ex}(\nabla\gamma_i)$ energies in terms of the Taylor series and keeping only the first element (only the next neighbor is considered in calculations), it can be written as

$$\Phi'_{ex} = A\sum_i (\nabla\gamma_i)^2,$$

where A is the exchange stiffness. In magnetic processes the exchange energy has a fundamental role. Declination of local moment is going to provoke alteration in other spins directions due to exchange interaction but this effect decays exponentially with distance. From this consideration a characteristic interval can be introduced. The distance on which the local moment declines by a factor of $\frac{1}{e}$ is called exchange length. Depending on the declination is occurred by internal magnetic field (H_i) or crystal anisotropy (K_1) one can distinguish $l_H = \sqrt{\frac{2A}{H_i J_s}}$ or $l_k = \sqrt{\frac{A}{K_1}}$. The magnitude of both l_H and l_k decreases with higher internal magnetic field and also with higher crystal anisotropy values.

3.1.4 Magnetocrystalline anisotropy energy

Magnetization in condensed matter is spontaneously oriented to certain crystallographic directions, which is called easy direction of magnetization. Evidently, the material can be easily magnetized in these directions, i.e. a squared hysteresis loop is observed. Directions by which it needs more effort to saturate the ferromagnetic substance are called hard directions, i.e. measured hysteresis loops are flat. Magnetocrystalline anisotropy energy density is calculated as the difference between the two energies invested to saturate the material because the applied field must work against the anisotropy force to turn the magnetization vector away from the easy direction. The magnetocrystalline anisotropy energy density can be expressed in terms of a series expansion of the direction cosines of M_s relative to crystal axes. In cubic crystals if M_s has angles between <100>, <010> and <001>, furthermore the cosines of these angles are $\alpha_1, \alpha_2, \alpha_3$, then

$$\Phi'_k = K_0 + K_1(\alpha_1^2\alpha_2^2 + \alpha_1^2\alpha_3^2 + \alpha_2^2\alpha_3^2) + K_2(\alpha_1^2\alpha_2^2\alpha_3^2), \tag{3.2}$$

where K_1, K_2 are first and second ordered anisotropy constants, which depend on lattice and electron i.e. structure of atoms. In most cases K_2 is negligible compared to K_1 values.

Moreover K_0 is usually ignored because it does not depend on angle and normally we are interested in the changes in the value of Φ'_k when M_s rotates from one direction to another.

The physical origin of crystal anisotropy is mainly the *spin-orbit* coupling. The strongest coupling, which keeps spins parallel or antiparallel is the exchange interaction, can also be called *spin-spin* coupling. When the external field tries to reorient the spin of an electron the orbit of that electron also tends to be reoriented. Since the orbit is strongly coupled to lattice, the spin axis is therefore resisted and the energy which is required to overcome the spin-orbit coupling is the crystal energy.

3.1.5 Magnetoelastic energy

Magnetoelastic energy density (Φ'_{ml}) is due to magnetostriction (λ_s). Magnetostriction means dimension changes of ferromagnetic material due to an applied external magnetic field. The sign of magnetostriction is said to be positive if the material elongates parallel to magnetic field direction and negative if the elongation is perpendicular. Taking account of internal and external stresses which interact with spontaneous magnetization the following equation can be deduced

$$\Phi'_{ml} = -\frac{3}{2}\lambda_s \sigma cos^2\vartheta, \tag{3.3}$$

where σ is tensile stress or compression and ϑ is the angle between spontaneous magnetization and direction of stress. In addition the value of magnetostriction varies with crystallographic directions. For cubic lattice, where the easy direction of magnetization is <100> and the hard direction of magnetization is <111>, λ_s can be expressed as

$$\lambda_s = \frac{3}{2}\lambda_{100}(\alpha_1^2\beta_1^2 + \alpha_2^2\beta_2^2 + \alpha_3^2\beta_3^2 - \frac{1}{3}) + 3\lambda_{111}(\alpha_1\alpha_2\beta_1\beta_2 + \alpha_1\alpha_3\beta_1\beta_3 + \alpha_2\alpha_3\beta_2\beta_3), \tag{3.4}$$

where $\beta_1, \beta_2, \beta_3$ are the direction cosines of strain and $\alpha_1, \alpha_2, \alpha_3$ are the direction cosines of magnetization relative to crystal axes. Often strain is in the same direction as the magnetization ($\alpha_1, \alpha_2, \alpha_3 = \beta_1, \beta_2, \beta_3$), thus Eq. 3.4 becomes

$$\lambda_s = \lambda_{100} + 3(\lambda_{111} - \lambda_{100})(\alpha_1^2\alpha_2^2 + \alpha_1^2\alpha_3^2 + \alpha_2^2\alpha_3^2).$$

3.2 Magnetic behavior in small structures

3.2.1 Superparamagnetism

In 1949 Néel pointed out that, below a certain size the magnetic moment of a particle is no longer fixed in one direction. If the thermal energy can overcome the anisotropy energy, the magnetization of a particle can flip from one easy direction to another even in the absence of applied field. In this case the material behaves just like a normal paramagnet (no remanence) with an important exception: the magnetic moment per atom is enormous compared to paramagnets. One can say that a material in superparamagnetic (SP) state is an ideal soft magnetic material because it has no coercivity, i.e. no magnetic loss. Standing against the magnetocrystalline energy, which must be overcome by thermal fluctuation, it can be written as

$$K_1 V = 25 k_B T, \tag{3.5}$$

where V is the volume of particle, k_B is the Boltzmann constant. For non-elongated form particles the shape anisotropy should also be included into Eq. 3.5. It should be noted that the transition from SP to single domain (SD) state (discussed below) is continuous and depends on the time window used for observation. For instance, a magnetization curve without hysteresis is obtained by VSM of solid state material, meanwhile Mössbauer spectroscopy may show sextet in spectra reflecting ferromagnetic behavior. This is because the observation time is long enough for spins to disalign (flip-flop) during the VSM measurement, but in a shorter time window, they are not relaxed and ferromagnetic behavior is found. A range for relaxation time (τ) is defined as 100 sec in classical theory for a particle to be stable, and taking the frequency factor (f_0) equal to 1GHz, the value of 25 in Eq. 3.5 is deduced as $ln(\frac{\frac{1}{100}}{e^{-9}}) =\sim 25$ as is discussed in detail in [34]. One can see, that the smaller the observation time the less the thermal energy can overcome the magnetostatic energy barrier, and the material exhibits superparamagnetic behavior. When superparamagnetism prevails, the coercivity is suppressed as

$$H_c = \frac{2K_1}{M_s}\left[1 - \left(\frac{25k_BT}{K_1V}\right)^{1/2}\right]. \tag{3.6}$$

Renormalizing Eq. 3.6 with $H_{c,0} = 2K_1/M_s$ (the coercivity, when the field is unaided by thermal energy), the so called reduced coercivity h_{ci} can be expressed as follows

$$h_{ci} = \frac{H_c}{H_{c,0}} = 1 - \left(\frac{V_p}{V}\right)^{1/2} = 1 - \left(\frac{D_p}{D}\right)^{3/2} = 1 - \left(\frac{T}{T_B}\right)^{1/2}.$$

As it is generally observed, the magnetostatic interactions between particles (*interacting* particles) suppress the coercive field, however it is very difficult to account for this interaction. Néel in 1947 derived a form $H_c(p) = H_{c,0}(1-p)$ (where p is the packing fraction), which is often followed experimentally.

3.2.2 Single domain state

As a compromise of magnetic energies, the particle can be in single domain state, if it costs less energy to support the higher magnetostatic state instead of creating a domain wall within the grain. This state is very important from an application sense of view, since fine particles in SD state exhibit high coercivity (hard magnets), thus they are used in magnetic recording media, permanent magnets, etc. In these materials, the presence of domain walls must be avoided, which thus lowers the coercivity and the source of noise in recording media.

The diameter of the particle must be smaller than the domain wall width for SD state, thus $D < \delta_{dw} = \pi\sqrt{\frac{A}{K_1}}$. Expressing later criteria with corresponding energies, one can write the wall energy as $\sigma_{dw}\pi r^2 = 4\pi r^2\sqrt{AK_1}$ (where σ_{dw} is the wall energy density), which must be exceeded by the magnetostatic energy saved to multidomain (MD) state, thus $\Delta E_{ms} \approx \frac{1}{3}\mu_0 M_s^2 V = \frac{4}{9}\mu_0 M_s^2 \pi r^3$. Standing against these energies, the critical radius (r_c) can be expressed as

$$r_c \approx 9\frac{(AK_1)^{1/2}}{\mu_0 M_s^0} \qquad (for\, large\, K_1\, values). \tag{3.7}$$

Eq. 3.7 is only valid, if the domain wall has the same structure as in infinite material. This means that the value of K_1 is large enough to maintain the orientation of magnetic moment in the direction of K_1 (easy axis) against surface poles, thus $K_1 \geq \frac{\mu_0 M_s^2}{6}$.

If K_1 is small the magnetic moment tries to minimize the magnetostatic energy of poles, and therefore tries to follow the surface of particle. When magnetization curls among the surface, the critical radius size can be given as (see details in [6]):

$$r_c = \sqrt{\frac{9A}{\mu_0 M_s^2}\left[ln\left(\frac{2r_c}{a}\right) - 1\right]}, \qquad (for\, small\, K_1\, values) \tag{3.8}$$

where a is the lattice constant.

Magnetization reversal in fine particles in SD state can be divided into two main groups, namely coherent or incoherent mode. In coherent or Stoner-Wohlfarth (SW) reversal (It should be called Akulov-Néel-Stoner, who presented the first solution for this problem [35]), the change of magnetization depends on the angle between the easy direction and applied field (θ_0). As a function of θ_0, magnetization can occur by rotation and a jump of flux at a critical field (switching field) resulting in various hysteresis loops. For instance, where $\theta_0 = 0$, squared loop with $M/M_s = 1$ can be obtained, while for $\theta_0 = \pi/2$ linear dependence of magnetization on applied field (with no remanence) can be observed. The remanence depends on θ_0 and given as $r_c = cos\theta_0$. For SW particles with randomly oriented easy axes M/M_s is calculated to be 0.5. For detailed interpretation of SW problem see for instance [34] or [6].

The most important incoherent reversal is the curling (or recently it is called vortex), where the magnetization in the particle is not strictly parallel during switching, but there are spins pointing away from the easy axis. This mode of magnetization saves magnetostatic energy but due to disalignment of spins it costs exchange-energy. The coercive field for curling is given as (after [6]) $H_c \approx a/r^2 - b$, where a and b are aspect ratios for an ellipsoid of revolution and $r < r_c$ (Eq. 3.8). Recently, in [36] it is pointed out by micromagnetic simulations that non-interacting $Fe_{80}Si_{20}$ fine particles (Finemet alloy) are in monodomain state up to 35 nm, where a new hard-axis oriented vortex state was found [37] and only above d=50 nm the particle is the "normal" easy-axis oriented vortex.

3.2.3 Origin of softness of amorphous and nanocrystalline magnetic materials (RAM)

In the multidomain (MD) state of magnetic particles the magnetostatic energy is diminished by the creation of magnetic domains. The magnetization changes with domain wall motion where the coercivity is mainly due to magnetic defects (strong local anisotropy) posing a barrier to domain wall (pinning). O'Handley et. al. pointed out that coercivity changes 1/D with grain size in MD state. Later on, in 1989 Herzer predicted that there is an intermediate region, where the grain size is smaller than wall thickness ($D < \delta_{dw}$) and the coercivity depends on D^6. For amorphous and nanocrystalline alloys the above mentioned criteria are satisfied, therefore they are in the so-called random anisotropy model (RAM) region.

RAM was originally proposed by Alben et. al. [38], which explains the soft magnetic properties of ferromagnetic amorphous structures. This model was used for nanocrystalline materials by Herzer [4, 39]. The model is based on the following considerations: If the grain size of crystal is large the magnetization can follow the easy magnetic direction, thus the magnetization process is determined by the magnitude of magnetocrystalline anisotropy (K_1).

For grains with very small size (< 20nm), the exchange interaction also forces the magnetic moments to align in parallel, thus hindering them from following the easy directions of each individual grains. Consequently the effective anisotropy is an average of several magnetically coupled nanograins, thus it is reduced in magnitude. The number of nanograins (N) in a coupled volume can be written as

$$N = (l_k/D)^3, \tag{3.9}$$

where l_k is the exchange length and D is the average grain size. Using random-walk statistical consideration the effective anisotropy (K_{eff}) can be given as $K_{eff} = (K_1 \cdot \sqrt{N})/N$, thus

$$K_{eff} = \frac{K_1}{\sqrt{N}}. \tag{3.10}$$

The dividing line between these regions is given by the ferromagnetic exchange length

$$l_k = \varphi\sqrt{\frac{A}{K_1}}, \tag{3.11}$$

where $\varphi = \sqrt{4/3}$ for amorphous metals and $\varphi = 1$ is assumed by Herzer. φ is a parameter which reflects both the symmetry of K_{eff} and the total spin rotation angle over the exchange-correlated coupling through amorphous-nanocrystalline chain.

Further improvement was induced by taking account of the nanocrystallized (v) / amorphous ($1 - v$) fractions and to the anisotropy of residual amorphous phase (K_{am}), thus Eq. 3.10 becomes

$$K_{eff} = v\frac{K_1}{\sqrt{N}} + (1 - v)K_{am}.$$

For most of the cases K_{am} can be neglected, using Eq. 3.9 one can thus write

$$N = \frac{v\varphi^3 A^{3/2}}{< K >^{3/2} D^3}$$

and finally

$$K_{eff} = \frac{v^2 K_1^4 D^6}{\varphi^6 A^3}. \tag{3.12}$$

Another important contribution is the effect of long-range uniaxial anisotropy (K_U) which increases the magnitude of effective anisotropy as follows

$$K_{eff} = K_U + \frac{\sqrt{K_U} K_1^2 D^3}{2A^{3/2}}. \tag{3.13}$$

If coercivity is related to effective anisotropy K_{eff}, then using the results for coherent spin rotation, taking Eq. 3.12 we can find

$$H_c = \frac{2K_{eff}}{J_s} = \frac{2v^2 K_1^4 D^6}{\varphi^6 A^3}. \tag{3.14}$$

It must be noted that the grain size dependence at the power 6 was found to be matched with experimental data [39]. Substituting Eq. 3.13 into Eq. 3.14 coercivity dependence is reduced at the 3rd power of average grain size, however it is not experimentally confirmed for the time being.

3.2.4 Exchange interaction through amorphous matrix (effective exchange stiffness)

Magnetic nanocrystalline alloys are usually prepared from amorphous precursor by partial crystallization. The magnetic softness of two phase structure is explained in terms of the reduction of effective anisotropy due to exchange coupled randomly oriented nanograins situated in the residual amorphous matrix (see Sec. 3.2.3).

The weakest link of these coupled systems is the amorphous interphase which usually has smaller Curie temperature compared to the nanocrystalline one, thus above this temperature the particles are decoupled and the averaging mechanism of RAM can not be effective. Interestingly experimental results show that this rise of coercivity occurs much above the Curie temperature of amorphous matrix [40]. Since the composition of residual amorphous phase after crystallization is certainly different than the T_C of as-quenched ribbon thus their Curie temperature, which also depends on the chemical composition must be dissimilar too.

Systematic investigation of decoupling behavior was carried out in [41, 42] by A. HERNANDO et. al. They pointed out that the exchange stiffness can be effective even above the T_C of amorphous intergranular phase and introducing a phenomenological parameter γ and substituting $A\gamma$ for A (so called effective exchange stiffness) into Eq. 3.14 the magnetic hardening at an early stage of crystallization can be explained. In other words γ is the capability of amorphous matrix and interphase to transmit exchange interaction between crystallites. It is calculated as

$$\gamma = e^{-t/l_{am}},$$

where t is the thickness of the intergranular layer $t = D/(v^{-1/3} - 1)$ and l_{am} is the exchange correlation length in the amorphous matrix.

The model mentioned above explains the temperature dependence of early stage of crystallization well, but it produces positive temperature dependence of γ below T_C^{am} [41] which can not explain the experimental results of $Fe_{91}Zr_7B_2$ alloy reported by K. SUZUKI and J. M. CADOGAN [43]. They tried to explain the increase of coercivity with T below T_C^{am} by taking into account the two local exchange stiffness in the random anisotropy model. The effective exchange stiffness is approached as a contribution of the crystallized and amorphous part:

$$\frac{1}{\sqrt{A}} = \frac{1}{\sqrt{A_{cr}}} + \frac{t/D}{\sqrt{A_{am}}}. \tag{3.15}$$

Using Eq. 3.15 the effective anisotropy in the new model is given by

$$K_{eff} \approx \frac{1}{\varphi^6} v^4 K_1^4 D^6 \left[\frac{1}{\sqrt{A_{cr}}} + \frac{v^{-1/3} - 1}{\sqrt{A_{am}}} \right]^6 . \tag{3.16}$$

Under the condition $A_{cr} = A_{am}$, the HERZER's original model (Eq. 3.12) can be deduced.

Another important phenomenon, namely the dipolar interaction must be relevant around the temperature where the intergranular phase becomes paramagnetic and the nanograins are supposed to be, at least partially, in superparamagnetic state. The simple dipolar coupling of otherwise superparamagnetic particles is able to account for the values of superparamagnetic transition temperature as it was shown by G. HERZER [44]. Quantitative evaluation of coercivity increases at the decoupling temperature, was firstly given by L. K. VARGA and F. MAZALEYRAT [3]. They pointed out that the collective response of the ensembles of

dipolar-coupled nanoparticles can give rise to magnetization processes which show the general characteristics of ferromagnetic behaviors such as remanence and coercivity. A so called dipolar stiffness A_d is deduced taking into account the magnetostatic dipolar interaction of particles in t intergranular distance from each other:

$$A_d = \frac{J_s^2 D^2}{16\pi\mu_0} v^{4/3}. \tag{3.17}$$

Introducing the dipolar stiffness into Eq. 3.15 the effective exchange stiffness can be written as

$$\frac{1}{\sqrt{A}} = \frac{1}{\sqrt{A_{cr}}} + \frac{t/D}{\sqrt{A_{am} + A_d}}. \tag{3.18}$$

Calculations point out that magnetostatic interaction between nanograins could efficiently replace the role of exchange interaction in averaging out the local magnetocrystalline anisotropy.

3.3 Tailoring of hysteresis loop

Amorphous and nanocrystalline soft magnetic materials are used widely in electronics and power electronics. They are employed in filters, chokes, transformers, inductors, motors, generators, sensors in magnetic recording, etc. Fortunately the diversity of SMM is very broad too. Therefore it is always important to choose the appropriate material for the given application. In order to have some rough guidelines about the alloy properties, the type of hysteresis loops are cataloged by the manufacturers (see Table 3.1 after [13]). Applications sorted by required hysteresis properties is given in Tab. 7.2 in Sec. 7.

These selected magnetic behaviors demanded for different applications can be achieved by various methods. Tailoring the hysteresis loop means systematically changing the Sec. 3.1 explained magnetic energies in order to obtain suitable hysteresis properties for the given application.

Sign of loop	μ_i	$\frac{B_R}{B_S}$	Shape of loop	Produced by
F	Between 10^3 and 10^4	$\ll 10\%$	Flat	Transverse field annealing
Z	$>3 * 10^5$	$>90\%$	Square	Longitudinal field annealing
X	Between 30k and 200k	$\approx 50\%$	Round	Conventional annealing
G	≈ 100	*	Flat	Localized air gap or compacted powder

Table 3.1: Hysteresis loops summarized by magnetic behaviors [after [13]].

3.3.1 Chemical composition dependence of magnetic energies

Casting alloys as a special composition of different elements can improve exchange-, crystal-anisotropy- and magnetoelastic energies. The best results in minimizing the sum of corresponding energies were achieved in Finemet alloy [1]. Namely, magnetoelastic energy in Eq. 3.3 depends on λ_s (among σ, which is supposed to be nearly 0 in optimally relaxed materials), which can be expressed as a balance between the nanocrystallized and amorphous phases

$$\lambda_s \approx v_{FeSi}\lambda_s^{FeSi} + (1 - v_{FeSi})\lambda_s^{am},$$

where $\lambda_s^{FeSi} \approx -6 \times 10^{-6}$ and $\lambda_s^{am} \approx +20 \times 10^{-6}$. Taking $v_{FeSi} \approx 0.7 - 0.8$ the global magnetostriction was found to be very close to zero. As for crystal-anisotropy and exchange energies, $K_1^{FeSi} = 8kJm^{-3}$ and $A = 10^{-11}Jm^{-1}$ respectively, thus using Eq. 3.10 the effective anisotropy is reduced to about $K_{eff} = 10 - 20Jm^{-3}$. Moreover the exchange length given by Eq. 3.11 is found to be $\approx 35nm$ in Finemet [45] which is far higher than the average grain size D=12 nm, thus criterion of random anisotropy model ($l_{ex} \gg D$) is satisfied. Thermal stability is determined by the exchange stiffness (A), since

$$A \propto \frac{T_c S^2}{a}, \tag{3.19}$$

where a is the lattice parameter and S is the spin.

This is where current work comes into the picture. This work involves increasing the value of A by Co addition in Finemet type alloys in order to improve its Curie temperature and magnetic stability of these materials. As it is well established FeCo alloys have the highest T_c , having maximum value at around Co=50% with $T_c^{virtual} \sim 1230°C$ and $A \approx 2.4 \times 10^{-11}Jm^{-1}$. Adding Co into Finemet alloy could lead to FeCoSi composed precipitated nanograins with elevated Curie temperature, which may retain a low value of K_1.

3.3.2 Tailoring loops by demagnetization factor

Besides tailoring alloys for optimal value by the composition dependent energies (Eq. 3.1), another way to modify the behavior of magnetic hysteresis, is to increase the demagnetization energy density (Φ'_{dm}). For this purpose, cut cores are mostly used. Introducing a discrete air gap in the core can drastically reduce the permeability, makes the core suitable for chokes. Disadvantages of these magnetic elements are the environmental noise and other inhomogeneous inductance distribution, close to the gap, which can provoke overheating in electric component [46]. These effects can be avoided if the gap is distributed in the material. However the filling factor of magnetic component is around 50-80%, thus magnetic moment per volume (magnetization) is reduced. Moreover, magnetic loss of compacted powders is always found to be higher compared to "one piece" magnetic components [47].

3.3.3 Tailoring loops by uniaxial induced magnetic anisotropy

The form of magnetic hysteresis can also be tailored by inducing long range magnetic anisotropy (K_u) in a preferred (longitudinal or transversal) direction. This method allows the original saturation values (no magnetic mass loss, compared to compacted powders) without electric noise or magnetic inhomogeneity to be maintained. Moreover the in-plane anisotropy can increase the magnetic resonance frequency and produce a linear permability response in broad frequency region ($\mu - f$). At the present time, there are thus two different approaches to inducing magnetic anisotropy in soft magnetic ribbons: applying magnetic field or mechanical stress during the annealing treatment.

Annealing of nanocrystalline materials under magnetic field was firstly reported in [48, 49]. Magnitude of magnetic field induced anisotropy was compared for both as-prepared and nanocrystalline Finemet materials. It was found that it is difficult to induce anisotropy in nanocrystallized samples at low temperature. Later on, investigations carried out by HERZER [50] showed that the larger amount of induced anisotropy is induced if the field is applied during crystallization. This phenomena is explained by the pair ordering of Fe-Fe atoms in

FeSi nanograins, at elevated temperature. Due to the higher mobility of Fe atoms they can be oriented in the direction of the applied field forming a distinguished magnetic direction in the material. First calculations about magnetic anisotropy for laminated FeCo alloys was made by NÉEL [51] and adapted for Finemet alloys by HOFMANN [52]. *Pair ordering model* seems to be suitable to explain the phenomena of field annealing, however field induced anisotropy was found in metallic glasses annealed above T_c. Moreover $K_u = 50Jm^{-3}$ was reported in nanocrystalline $Fe_{86}Zr_6B_7Cu_1$ (Nanoperm) alloys where the nanocrystals contain only iron, so the pair ordering is not possible.

Stress annealing on Finemet nanocrystalline alloys was firstly reported by GLASER et. al. [53]. Mechanically induced magnetic anisotropy can be found in Finemet alloys 2 order of magnitude higher ($K_u^{stress} \sim 8000Jm^{-3}$) than the field induced one ($K_u^{field} \sim 25Jm^{-3}$) and one order of magnitude higher than in amorphous glassy metals ($K_{u,amorph}^{stress} \sim 150-300Jm^{-3}$). Indeed, OHNUMA et. al. [54] observed structural changes in stress annealed Finemet, namely the lattice parameter has higher value of about 0.2% in the direction of ribbon's axe.

For the time being, two concurrent explanations exist for stress-induced anisotropy: the tensile back-stress theory proposed by HERZER [50] and NÉEL's model of atomic pair ordering adapted by Hofmann and Kronmüller [55].

HERZER attributes it to the magnetoelastic effect. In amorphous alloys the sign of induced anisotropy correlates with the sign of magnetostriction coefficient. From Eq. 3.3, one can write

$$K_u = -\frac{3}{2}\lambda_s\sigma.$$

In nanocrystalline alloys, the problem becomes more complex since the external stress generated internal stresses are heterogeneously distributed in the two-phase material, thus the induced magnetoelastic anisotropy is deduced as [56]

$$K_u = -\frac{3}{2}(v\lambda_c\sigma_c + (1-v)\lambda_a\sigma_a),$$

where σ_c and σ_a denote the stresses located in the volume fraction of nanograins and amorphous phase, respectively.

HOFMANN and KRONMÜLLER gave an other interpretation, which is based on the same phenomena discussed above for field annealed materials, namely NÉEL's model of atomic pair ordering. In this case the applied stress can provoke an anisotropy in pair ordering of Fe-Fe atoms in FeSi nanograins. Here again a contradiction can be found regarding Nanoperm alloys, because atom pair ordering is not possible since nanograins are only composed by Fe atoms.

As a consequence, the origin of stress-induced anisotropy is still not well known and the present work tries to contribute to further interpretation of this phenomenon.

3.4 Determination of transversal induced magnetic anisotropy

1. From torque curves

For this method a thin disk of sample is required. We consider a uniaxial crystal such as hexagonal crystal with an easy axis parallel to c axis (Fig. 3.1) and the disk is suspended by a torsion wire at its center, thus the applied strong magnetic field is horizontal and parallel to the plane of the disk. Now, if the torsion wire is turned clockwise, the c axis rotates away from the field direction by an angle of θ. If the applied field saturates the material, then M_s and H are parallel and the angle between them will also be θ. The crystal anisotropy energy (E) can be expressed (if K_2 is negligible) as

$$E = K_1 sin^2\theta.$$

The derivative of the energy with respect to the angle θ is a torque (L), thus

$$L = -\frac{dE}{d\theta} = -2K_1 sin\theta cos\theta = -K_1 sin2\theta.$$

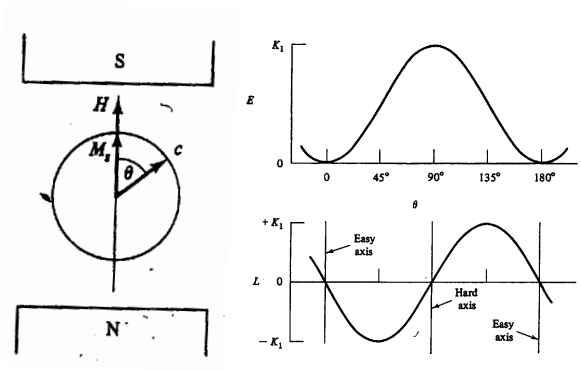

Figure 3.1: On the left: Horizontal section of the disk shaped sample in the magnetic field, c = easy axis. On the right: Variation with θ (angle between M_s and easy axis) of the anisotropy energy and torque L (after [34]).

Fig. 3.1 shows how E and L vary with angle. The slope of torque curve is negative in stable position ($\theta = 0$) and positive for unstable one ($\theta = 90°$). The value of K_1 is the amplitude of the torque curve. For cases, when K_2 is also relevant, the experimentally obtained torque curve has a component of that energy. Long range induced anisotropy (K_u) also contributes to torque curve.

In the experimental torque curve taken from macroscopic scaled nanocrystalline sample, the K_1 and K_2 values would have no contribution in the plot due to the randomly oriented nanocrystals in the material. Therefore only the long range magnetic anisotropy (K_u), induced by various methods could be measured. Unfortunately in order to avoid the shape anisotropy contribution to torque curve, the measured sample must have strictly disk form, which cannot be made from nanocrystalline sample. Therefore the value of K_u has to be determined from hysteresis curve.

2. From magnetization curves

Magnetic energy density (W) stored in the material can be calculated as the area between the hysteresis loop and vertical ($J = \mu_0 M$) axis. In mathematical form it can be expressed as

$$W = \int_0^{J_s} H dJ. \tag{3.20}$$

The applied external magnetic field must work against this volumic energy to align the magnetic moment to the direction of field in the material. If the induced anisotropy is the dominant energy it can be deduced using Eq. 3.20.

It is important to say that induced anisotropy is always calculated as a difference between magnetic energies. Since the effect of applied stress or magnetic field annealing on magnetic properties was investigated, hence another sample (of same composition) was always annealed under the same conditions but without stress or field in order to have it as reference. This allows us to compare the results of two different treatments.

If one supposes that the saturation occurs mainly by magnetization rotation, the result is a linear hysteresis curve up to saturation (see Fig. 3.2) and anisotropy can be obtained as

$$K_u = \frac{1}{2} J_s H_k,$$

where H_k is the field at which the external applied field becomes perpendicular to the uniaxial anisotropy direction. This magnetic field H_k is characteristic to uniaxial anisotropy thus called anisotropy field. However this method to obtain K_u is valid for flat loops only.

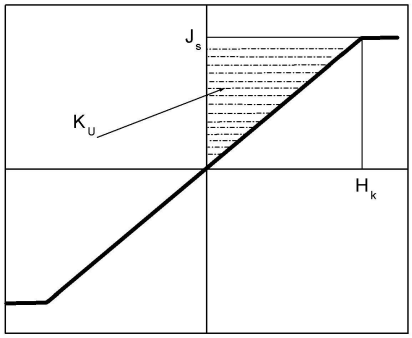

Figure 3.2: Uniaxial anisotropy energy density (K_u) calculated from hysteresis curve.

Using a sophisticated method reported by BARANDIARAN et al. [57] which deals with the second derivative of measured hysteresis cycle results in a distribution of anisotropy field $P(H_k)$ which can be calculated as

$$P(H_k) = -H(\frac{d^2 m}{dH^2}) \tag{3.21}$$

where $m = \frac{J}{J_s}$. For this calculation hysteresis curve from J_r up to saturation (J_s) is taken and the mean value of distribution is considered as H_k (see Fig. 3.3). This method

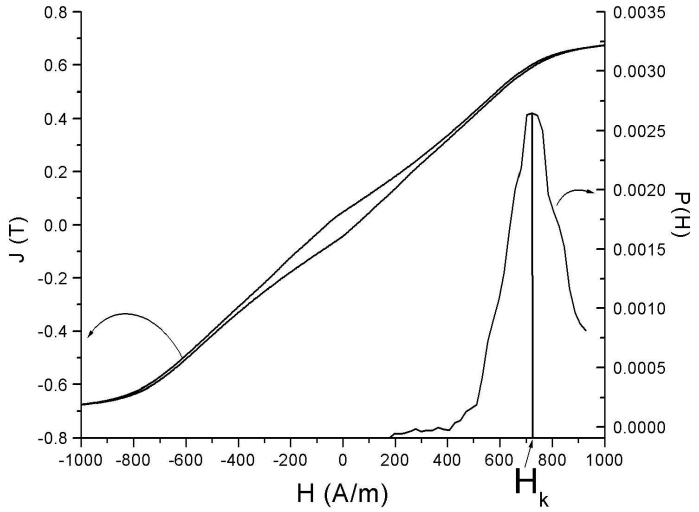

Figure 3.3: Anisotropy field distribution obtained from Eq. 3.21.

is valid for any loop having a perpendicular component of anisotropy, thus applying it for ribbons having transversal anisotropy gives the value of K_u and information about the nature of anisotropy as well. Namely, the narrower the width of anisotropy distribution, the more the uniaxial anisotropy is aligned in one discrete direction. This actually means higher amplitude of $P(H_k)$ too. In other words a broadening in the anisotropy distribution indicates a higher deviation of spontaneous magnetization from the transversal direction.

In the case of longitudinal induced anisotropy, the square hysteresis loop is clearly unsuitable for these evaluations. For this purpose a novel method determining longitudinally induced magnetic anisotropy ($K_u < 0$) has been developed. This method is discussed in details in Sec. 5.4.1.

4 Experimental Techniques

4.1 X-ray diffractometry

X-ray diffractometry is one of the most important characterization methods in materials science. The X-ray is a kind of electromagnetic radiation with a wavelength of a few tenth of a nanometer. The X-ray beam is produced in a vacuum tube. From the heated cathode (negative pole) the thermoionic excited electrons are accelerated by an acceleration voltage of a few 10kV, between the two poles in the tube. The high velocity electrons impact the anode

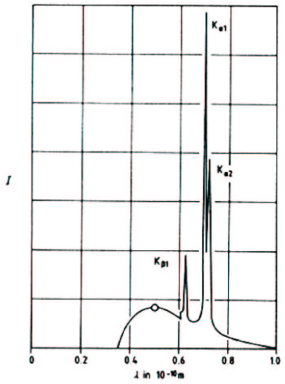

Figure 4.1: A typical energy spectrum of X-ray tube.

(positive pole) and the main part of energy transforms into heat. The rest (the important part) became a electromagnetic radiation with high penetration ability. The exiting radiation has two parts: a continuous so called "white radiation" and a discreet peak showed characteristic one (see in Fig. 4.1). The electron beam typically ejects core electrons from the target metal, making the atoms unstable. The atoms relax from these positions by dropping an outer valence electron to the core level (K,L shell). This large decrease in energy required for an electron to be able to drop to the core level, requires the emission of the excess energy in the form of a photon. These photons have the typical energy of X-rays. As a function of distance between the outer and core level the emissions have different values like $K_{\alpha 1}$,$K_{\alpha 2}$,$K_{\beta 1}$, etc. and which are practically monochromatic. To suppress the less intensive peaks, filters can be used. The energy emitted (wavelength) depends on the material of anode. The most employed anodes are made of Cu, Co, Mo, W, Au and Ag having high melting point and good conductivity. It must be noticed, that the copper based tube has fluorescence on Fe, thus secondary monochromator is used (which reduces the intensity). Using cobalt cathode X-ray tube the effect can be avoided, nevertheless $K_{\alpha 2}$ is more intense as compared to Cu and very close to $K_{\alpha 1}$, which can result double peaks (or broad peaks) in diffraction without employing filters.

The interaction between the X-ray and the solid state material can be approached like the light scattering on an optical lattice. Considering the crystal composed of parallel atomic planes at a distance d, one part of the beam is completely reflected while the other part is scattered in θ angles. The condition of interference of the parallel beams is that the path differences must be half integer multiples of wavelength (see Fig.4.2). If the path differences of diffracted beams is $2sin\theta$, the condition for maximal reinforcing interference is

$$2dsin\theta = n\lambda, \tag{4.1}$$

where the λ is the wave length and equal to 0.1788965 and 0.1540598 nm for Co and Cu anode, respectively. This is the Bragg law, the basic relationship in X-ray diffractometry [58].

The distance between given planes is related to the lattice parameters and to Miller (hkl) indexes. Using the spatial Pythagoras theory for cubic crystal, the following equation is deduced:

$$d = \frac{a}{\sqrt{s}}, \tag{4.2}$$

where $s = h^2 + k^2 + l^2$. Using both Eq. 4.1 and Eq. 4.2 the so called "squared" form can be obtained:

$$sin^2\theta = \frac{n^2\lambda^2 s}{4a^2}. \tag{4.3}$$

The interference of a *hkl* plane does not only depend on the θ scattering angle but the scattered intensity of the given orientation. The F_{hkl} structure factor is given:

$$F_{hkl} = \Sigma_j f_j e^{2\pi(hx_j+ky_j+lz_j)}, \tag{4.4}$$

where f_j is the j-th atom, f atomic form factor which is proportional to the atomic number. The intensity of the diffraction lines has a dependence on the squared structure factor: $I_{hkl} \sim |F_{hkl}|^2$. As long as the crystal lattice is primitive, all the crystalline planes come to diffracted position. For the case, when the lattice has a high degree of symmetry (BCC or FCC), some planes produce destructive interferences as a consequence of Eq. 4.4. This phenomenon is called *extinction rule*. Hence the diffractometry image of a complex lattice has systematical lacks compared to the primitive one, which helps us to determinate the exact structure after indexing.

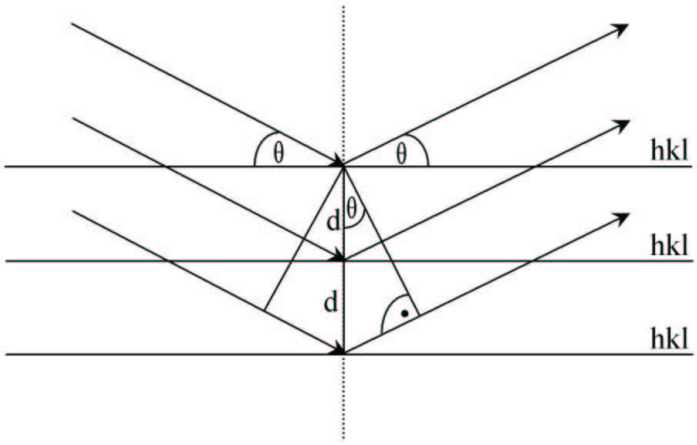

Figure 4.2: Scheme explaining Bragg's law

Considerations for amorphous-nanocrystalline diffractograms

The evaluation of structural parameters of an amorphous-nanocrystalline system from X-ray diffractometer results needs careful investigations. The broad amorphous halo usually overlaps with the highest intensity of Fe, reflected form the (110) plan. For cases, where the size of nanograin (D) is very small ($< 10nm$), due to the enlargement of line width of the crystalline component, it is difficult to clearly separate the two phases. However, in Finemet type alloys, the nanograins are higher than 10 nm and the peak of [110] plane of BCC lattice is a bit shifted from the amorphous one. Various peak fitting softwares (Origin, Matlab) can be used to treat these diffractograms if the amorphous contribution is relevant ($> 40\%$), nevertheless the evaluated phase fractions depend strongly on the chosen baseline: the second and third peaks of amorphous phase can be confused with the baseline.

For a more appropriate phase deconvolution and parameter evaluation, a user friendly simulation program called BERTA was written by F. Mazaleyrat [59] taking into account the below mentioned physical considerations (see the program in action in Ch. 7, Fig. 7.1).

The crystalline fraction is presented in theory (no stress and default in crystal) by a Gaussian profile in the diffractogram:

$$\mathrm{G}_{\phi,\beta}(\theta) = \frac{2}{\pi} \cdot \frac{\beta}{4(\theta-\phi)^2+\beta^2},$$

where $\beta = \frac{\lambda}{2Dcos\varphi}$, D is the nanograin size (domain size of coherent reflection) and $\phi = arcsin(\frac{\lambda}{2d})$. In a diffractogram of BCC lattice (from 20° to 140°) the visible peaks from different plans, one after the other are (110), (200), (211), (220), (310) with s=2,4,6,8,10 and leaving the other parameters constant, only the intensity of these parameters must be adjusted, which depends on the texture of material.

As for the contribution of amorphous phase, it can be considered as a perfectly homogeneous solid state in long scale, while the short range order depends on the composition. Therefore the position and intensities linked to amorphous phase are a priori known. The reflection plans of amorphous matter has constant relative distances: 1, 5/3 and 2, assuming a structure close to tetrahedral. The intensities can also be predicted due to the homogeneity in large scale: 1, 1/5 and 1/7. Heavy distortion and defaults in the structure presumes Lorentzian peak profile:

$$L_{\phi,\beta}(\theta) = \frac{2}{\beta}\sqrt{\frac{ln2}{\pi}} exp\left[\frac{-4ln2(\theta-\phi)^2}{\beta^2}\right],$$

with $\sqrt{s} = 1.25\,1.25/1.67\,1.25/2$ for the amorphous plane.

The atomic distance x_m in amorphous can be expressed as $x_m = d\sqrt{s}$, which can be considered as the lattice parameter of amorphous structure.

In practice, the profile of crystalline peaks must be fitted by pseudo-Voigt function, which is a sum of Gaussian and Lorentzian functions:

$$pV(\phi,\beta,\xi) = \xi L(\phi,\beta) + (1-\xi)G(\phi,\beta),$$

where $\xi \approx 0.3 - 0.5$. If the sample is not perfectly positioned in the focus plan of measurement, a shift in the peak position is observed. The Nelson-Taylor-Sinclair formula gives a correction for the present problem:

$$\frac{1}{\theta_{cor}} = \frac{1}{sin\theta} - \frac{k}{\lambda} cos^2\theta \left(\frac{1}{sin\theta} - \theta \right).$$

The crystalline fraction v is calculated from the area ratio of crystalline (110) and the main peak of amorphous phases. However, this calculation also needs a correction because the crystalline phase is usually overestimated. The amorphous phase is rich in the light element (B), and in Eq. 4.4 presented f form factor depends on the atomic number, moreover $I_{hkl} \sim \mid F_{hkl} \mid^2$. If c is the concentration of light elements in the amorphous and its diffusion is very small in the amorphous phase, the correction can be expressed as:

$$\Delta v = \frac{(1-c)(1-v)}{(1-c)(1-v)+v}.$$

The value of c after annealing does not exceed 0.3, which brings a $\Delta v \approx \pm 10\%$ at $v = 50\%$.

The principle of powder technique was used to carry out the X-ray measurements. This technique requires the crystalline sample in fine powder form or in a plane surfaced polycrystalline sample. The instrument used for investigations was a Phillips (model '68) type X-ray with water cooled Cu anode. The performance of electron tube is 1200W (40kV accelerator voltage with 30mA anode current). The surface oxidation of the ribbons was removed using superfine emery paper. The measurements were taken on the shiny side (the side which does not contact the wheel during quenching) of the ribbons in every case.

Wide angle X-ray radiation (WAXS) measurements were carried out in the European Synchrotron Radiation Facility (ESRF) in Grenoble, France. In this technique, the synchrotron radiation is emitted by the charged particles (electrons), moving at speed close to the light speed, when their trajectory is altered. The advantages of WAXS compared to conventional XRD are the high intensity of beam line, which is much better collimated and its wavelength (energy) is tunable (E=12.46kV $\Rightarrow \lambda = 0.995181$Å).

4.2 Mössbauer spectroscopy

Mössbauer spectroscopy [60, 61, 62] is based on the recoil-free resonance fluorescence of γ-photons observed with certain atomic nuclei. Using this method it is possible to measure the energy of nuclear levels with a very high accuracy. This accuracy is required to determine the slight variation of nuclear energy caused by electric monopole, electric dipole and magnetic dipole interactions between nucleus and electrons. These interactions express the electronic and magnetic changes, but geometric and defect structure can also be measured. The two conventional methods to take Mössbauer spectra are the transmission Mössbauer spectroscopy (TMS) and the conversion electron Mössbauer spectroscopy (CEMS). TMS gives information mainly from the bulk ($\sim 10 - 20\mu m$) while by CEMS information can be obtained from the surface ($\sim 0.1 - 0.4\mu m$). In a typical MS experiment Doppler effect is used to modify the energy of the emitted γ-ray by moving the source. This source contains the excited states of nuclei of a Mössbauer-active nuclide 'frozen' in a solid matrix in order to satisfy the recoilless condition. Practically the nuclei of the Mössbauer-active element (^{57}Fe,^{119}Sn,^{151}Eu) are diffused into a thin metallic matrix (Rh,Pd or Pt). This modified energy is used to scan the absorption characteristics of the studied sample. The counts are recorded as a function of Doppler velocity by a scintillation or proportional detector placed behind the absorber

(sample). The velocity calibration of the spectra is performed by measuring the spectrum of standard materials (usually pure $\alpha - Fe$).

In the case of CEMS, 6.4keV X-rays are detected as a result of inner conversion of the Mössbauer-active element after resonant absorption and re-emission. These X-rays are detected using $Ar - CH_4 - flowed$ proportional detector.

From an analytical point of view the most important Mössbauer parameters of an investigated sample are:

- Mössbauer-Lamb factor (f)
- Mössbauer line width (Γ)
- Isomer shift (δ)
- Quadrupole splitting (ΔE_Q)
- Quadrupole shift (2ε)
- Magnetic splitting (ΔE_m)

The Mössbauer-Lamb factor gives the probability of the recoil-free γ-photons emission (or the absorption) of the nuclei:

$$f = exp\left[-\frac{E_R}{k\Theta_D}\left(\frac{3}{2} + \frac{\pi^2 T^2}{\Theta_D^2}\right)\right], \tag{4.5}$$

if $T << \Theta_D$, where Θ_D is the Debye temperature of that solid state metal. The interaction has smaller probability with increasing temperature (T). Furthermore, Eq. 4.5 shows that the higher Debye temperature (Θ_D) the higher probability of Mössbauer effect. On the contrary, the value of Mössbauer-Lamb factor decreases with the higher energies of γ-quanta (E_R).

The line width (Γ) depends on the lifetime of excited states. For appropriate thin absorbers the form of the Mössbauer line can be described by the Lorentz function:

$$I(E) = const\frac{\Gamma}{(E - E_0)^2 + \frac{\Gamma^2}{4}},$$

where E_0 is the emitted energy of γ-photons.

The chemical isomer shift arises due to the non-zero volume of the nucleus and the electron charge density due to -electrons within it leading to an electric monopole (Coulomb) interaction which alters the nuclear energy levels. The volume of the nucleus in its ground and excited states are different and the s-electron densities are affected by the chemical environment. This relationship between s-electron density and nuclear radius is given by

$$\delta = \frac{2\pi}{5} Ze^2(R_e^2 - R_{gr}^2)\left\{|\Psi_A(0)|^2 - |\Psi_E(0)|^2\right\}, \tag{4.6}$$

where R_e^2 and R_{gr}^2 are the radii of the excited and ground nuclear states of Mössbauer nuclei, $|\Psi_A(0)|^2$and $|\Psi_E(0)|^2$are the electron densities at the absorbing and emitting nuclei and Z is the atomic number.

Any difference in the s-electron environment between emitter and absorber thus produces a shift in the resonance energy of the transition. This shift cannot be measured directly and

so a suitable reference (generally $\alpha - Fe$) is necessary, such as a specific source or an absorber. The Isomer Shift is good for probing the valency state of the Mössbauer atom. As the wave functions of the s-electrons penetrate into outer shells, changes in these shells will directly alter the s-electron charge density at the nucleus. For example, $Fe^{2+}$and Fe^{3+} have electron configurations of $(3d)^6$and $(3d)^5$ respectively. The ferrous ions have less s-electron density at the nucleus due to the greater screening of the d-electrons. This produces a positive Isomer Shift greater in ferrous iron than in ferric in high spin state.

In the case of electric quadrupole splitting the nucleus has a spin quantum number I>1/2 which means it has a non-spherical charge distribution. The magnitude of the charge deformation,Q , is given by

$$eQ = \int \rho r^2 (3cos^2\theta - 1) d\tau, \tag{4.7}$$

where e is the charge of the proton, is ρ the charge density in a volume element $d\tau$ at a distance r from the center of the nucleus and making an angle θ to the nuclear spin quantization axis. The sign of Q indicates the shape of the deformation. Negative Q value is due to the nucleus being flattened along the spin axis, whereas an elongated nucleus gives a positive Q value.

An asymmetric charge distribution around the nucleus causes an asymmetric electric field at the nucleus, characterized by a tensor quantity called the Electric Field Gradient (EFG) ∇E, and can be given as

$$\nabla E = -\frac{\partial V}{\partial x_i \partial x_j} = -V_{ij},$$

where $\{x_i, x_j\} = \{x, y, z\}$and V is the electrostatic potential.

There are two contributions to the EFG i) lattice contributions from charges on distant ions and ii) valence contributions due to incompletely filled electron shells. If a suitable coordinate system is chosen the EFG can be represented by three principal axes V_{xx}, V_{yy}, and V_{zz}. If an asymmetry parameter is defined using these axes as $\eta = \frac{V_{xx} - V_{yy}}{V_{zz}}$, and choosing the indexes as $V_{zz} \geq V_{yy} \geq V_{xx}$ the EFG can be specified by two parameters: V_{zz} and η. The excited state of ^{57}Fe has a spin I=3/2. The EFG has no effect on the I=1/2 ground state but does remove degeneracy in the excited state, splitting it into two sub-states $m_I = \pm\frac{1}{2}$ and $m_I = \pm\frac{3}{2}$ where the $m_I = \pm\frac{3}{2}$ states are higher in energy for positive V_{zz}. Finally the separation between the lines (Δ), is known as the quadrupole splitting and is given by

$$\Delta = \frac{1}{2} eQV_{zz} \sqrt{1 + \frac{1}{3}\eta^2}.$$

Magnetic hyperfine splitting is caused by the dipole interaction between the nuclear spin moment and a magnetic field. The effective magnetic field experienced by the nucleus is a combination of fields from the atom itself, from the lattice through crystal field effects and from external applied fields. This can be considered for now as a single field, H, whose direction specifies the principal z axis.

The magnetic splitting can be written as

$$\Delta E_m = -g\mu_N H m_I,$$

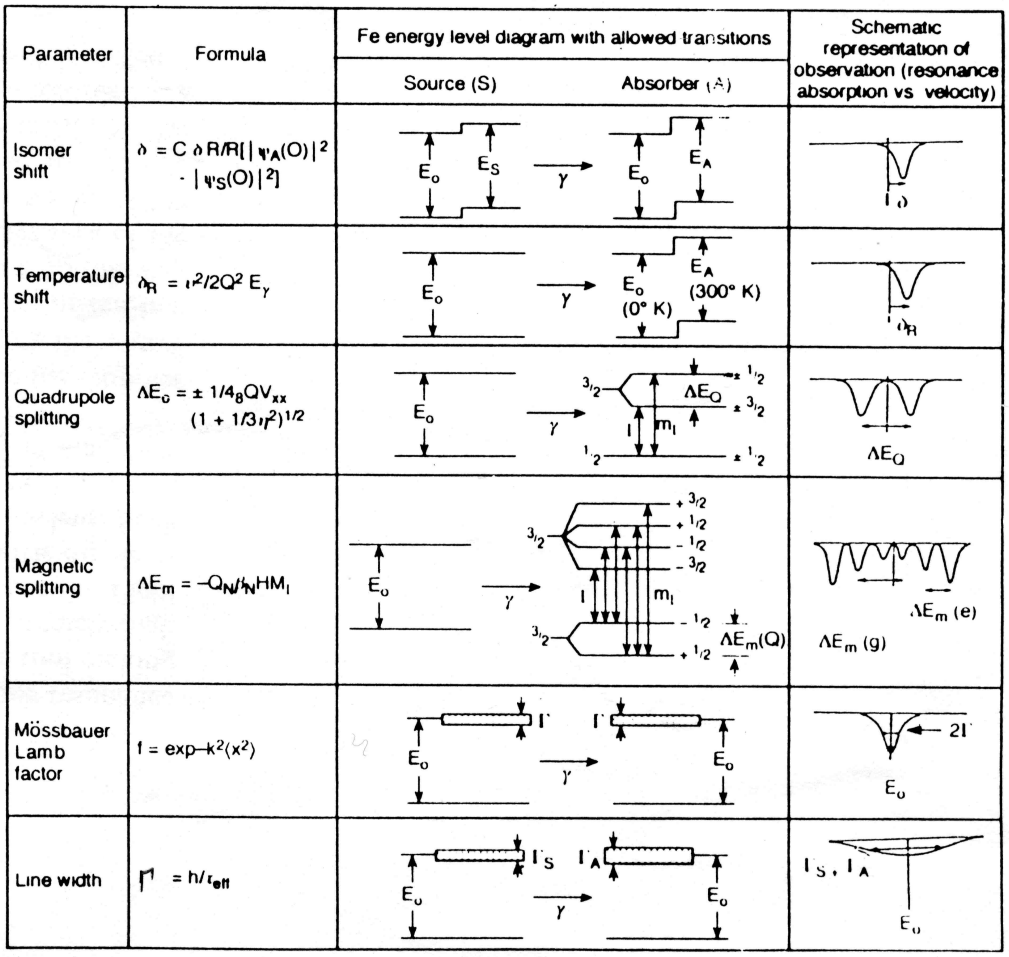

Figure 4.3: The main Mössbauer parameters (after [63])

where μ_N is the nuclear Bohr magneton, g is the nuclear g-factor, H is the effective magnetic field at the nucleus, m_I (I, I-1 ,... ,-I) is the magnetic quantum number. The magnetic field splits the nuclear level of spin I into (2I+1) equispaced non-degenerate substance. This and the selection rule of $\Delta m = 0, \pm 1$ produces splitting and a resultant spectrum as shown in Fig. 4.3 for a $I = \frac{3}{2} \Longrightarrow \frac{1}{2}$ (^{57}Fe) transition.

The intensities of absorption lines depend on the angle (Θ) between the magnetic orientation and the direction of γ-rays:

$$R = \frac{I_{2,5}}{I_{1,6}} = \frac{4sin^2\Theta}{3(1+cos^2\Theta)}, \tag{4.8}$$

where $I_{2,5}$ is the second and fifth, $I_{1,6}$ is the first and sixth line intensities (labelled as the energy increases). Mössbauer investigations were carried on in the Laboratory of Solid State Physics (LPEC) at University of Maine by the courtesy of PROF. J.-M. GRENÈCHE and in the Faculty of Science at Eotvos Lorand University by the courtesy of PROF. E. KUZMANN and PROF. A. VÉRTES.

4.3 Transmission electron microscopy (TEM)

The TEM is based on electron-specimen interaction. The high energy electrons impact on the material provoking a couple of physical quantum-physics interactions (Fig. 4.4). The

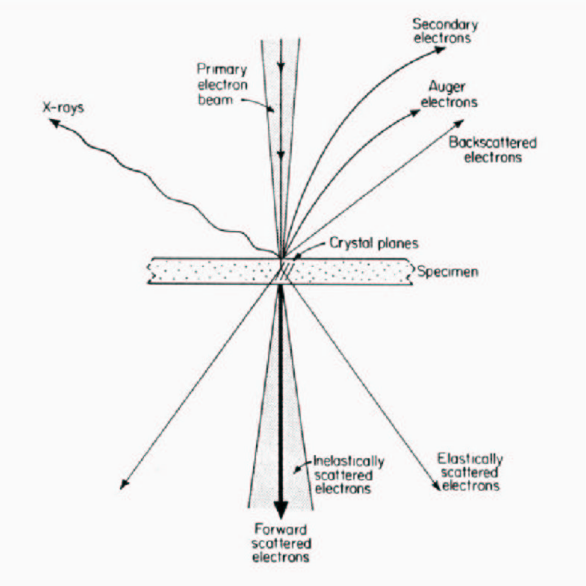

Figure 4.4: Electron-specimen interactions

accelerated electrons generated effects are the following:

1. Forward scattered electrons. There is no energy loss and no direction change. It is used for creating bright-field (BF) image in TEM.

2. Inelastically scattered electrons. There is only a small energy loss, and the scattering is in small angles. It is used for special image creations.

3. Elastically scattered electrons. There is no energy loss but fairly high direction change. This is described by the Bragg's law. It is used for dark-field (DF) in TEM and high resolution electron microscopy (HREM).

4. Secondary electrons. These are the weakly bounded outer electrons, knocked out by the beam. They give information from the surface in scanning electron microscopy (SEM).

5. Backscattered electrons. They are scattered in large angles (elastically and inelastically too). They are used in SEM technique.

6. Auger-electrons. These come from the inner shells of atom as a consequence of beam impact (electron⇒X-ray photon ⇒Auger-electron). They are used for investigation of the chemical composition.

7. X-ray radiation. The beam causes vacancy on the inner shell. The atom relaxes from this position by dropping an outer valence electron to the core level during an X-ray photon emits. Used in analytical electron microscopy (AEM) for determination of chemical compositions.

The two essential methods for TEM are the BF and DF image constructions. Generally it can be said that the BF image gives information about the global structure while in the DF one only the specific crystallographic orientations will be highlighted. All TEM investigations were

made at Faculty of Materials Science and Engineering in Warsaw University of Technology by the courtesy of J. FERENC PhD.

4.4 Vibrating sample magnetometer (VSM)

The VSM uses an induction technique, and is widely used for characterization of ferromagnetic materials. (Sometimes called Foner, after the inventor [64].) The sample is fixed at one end of a rod oscillating in a pick up coil set, in a homogeneous and adjustable transversal magnetic field. The vibrating sample generates a change in magnetic flux (φ), thus inducing an AC voltage in the measuring coils, directly proportional to the magnetization of the sample.

If the specimen is considered as a dimensionless object and $\vec{M}$ is its magnetic moment, the induction $\vec{B}$ ('far' from the magnetic object) can be expressed as the following:

$$\vec{B} = \frac{\mu_0}{4\pi r^3} \cdot \left[\frac{3(\vec{M} \cdot \vec{r}) \cdot \vec{r}}{r^2} - \vec{M} \right]. \tag{4.9}$$

When the sample vibrates (in one dimension (z)), the variation of $\vec{B}$ induces a voltage in a well-positioned coil:

$$V(t) = I \cdot \omega \cdot \frac{d\varphi}{dz} \cdot sin(\omega t), \tag{4.10}$$

where I is the amplitude of oscillation. Using Eq. 4.9 and knowing that $d\varphi = \vec{B} \cdot d\vec{S}$, the instrument constant (K) can be obtained by integration. This parameter depends only on the practical realization (geometry) of the system. The induced voltage can be written as:

$$V(t) = K \cdot n \cdot I \cdot f \cdot M \cdot \mu_0 \cdot sin(\omega t). \tag{4.11}$$

The $\vec{M}$ $[Am^2]$ represents the whole magnetic moment in the sample, but a more characteristic unit is the mass specific magnetic moment σ $[\frac{Am^2}{kg}]$:

$$\sigma = \frac{\left|\vec{M}\right|}{m}, \tag{4.12}$$

If ρ is the density of the sample, the magnetic polarization J $[T]$ comes as:

$$J = \mu_0 \cdot \rho \cdot \sigma. \tag{4.13}$$

The measured parameters are:

1. The frequency of vibration (f [Hz])
2. The amplitude of induced voltage (U [V])
3. The external magnetic field (H_{ext} [T])
4. The mass of sample (m $[g \times 10^{-3}]$).

The relation between σ and the above mentioned parameters is:

$$\sigma = \beta \cdot \frac{U}{f \cdot m}. \tag{4.14}$$

β is a coefficient, it comes from the instrument calibration. It does not depend on the magnetic properties of sample. The calibration process was made with well-known materials like pure

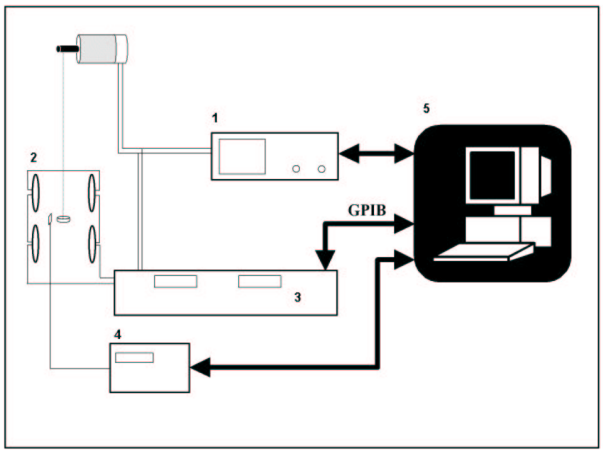

Figure 4.5: The scheme of VSM measurement

Ni, iron powder or amorphous Finemet (15.5% Si). It is worth noticing that the pure Ni is the most preferred, due to its high resistance against oxidation.

The scheme of VSM set-up can be seen in Fig. 4.5:

1. Motor supply. Controls the frequency of the motor (sample vibration) and gives reference for Lock-in.

2. Pick-up coils. To measure the vibrated sample induced voltage. For a better characteristic, 4 of them were employed.

3. Lock-in amplifier. To capture the amplitude of induced voltage. Synchronized to the sample vibration in order to decrease the noise.

4. Tesla meter. To measure the excitation magnetic field.

5. PC. The whole set-up is computer controlled by GPIB standard.

All the measurement were carried out at room temperature. The maximum value of magnetic field (produced by the water cooled electromagnetic coils) was 0.9T≈700 kA/m. Further information about the instrument built at SATIE can be found in [65].

4.5 Small angle magnetization rotation (SAMR)

The determination of saturation magnetostriction (λ_s) by SAMR is based on the measurement of induced voltage in a sense coil, wound around the sample, when it is submitted to a particular bi-axial excitation [66]. A dc field is applied to saturate the ribbon along its long axis ($H_{||}$). An other perpendicular ac field ($H_{\perp} = H_{\perp max} \cdot sin(\omega t)$) is also applied to force out the spins with θ angle from the ribbon plane. The induced voltage can be written as the following:

$$e_{\omega} = -\mu_0 \cdot N \cdot M_S \cdot S \cdot sin\theta \cdot \frac{d\theta}{dt} \approx -\mu_0 \cdot N \cdot M_S \cdot S \cdot \theta \cdot \frac{d\theta}{dt}, \tag{4.15}$$

where N is the number of turns and S is the cross-section. The consideration (right side of Eq. 4.15) is valid only for small value of θ. The stable state of spins is where $\frac{dE}{d\theta} = 0$. Induced voltage can be re-written as (see the development explications for instance in [67]):

$$e_{2\omega} = \frac{N}{2} \cdot M_S \cdot S \cdot \omega \cdot (\frac{H_{\perp max}}{H_{||} + H_K + H_d})^2 \cdot sin(2\omega t), \tag{4.16}$$

where $H_K = \frac{3 \cdot \lambda_S \cdot \sigma}{\mu_0 \cdot M_S}$ is the anisotropy field and $H_d = (N_\perp - N_{||}) \cdot M_S$ is the demagnetizing field.

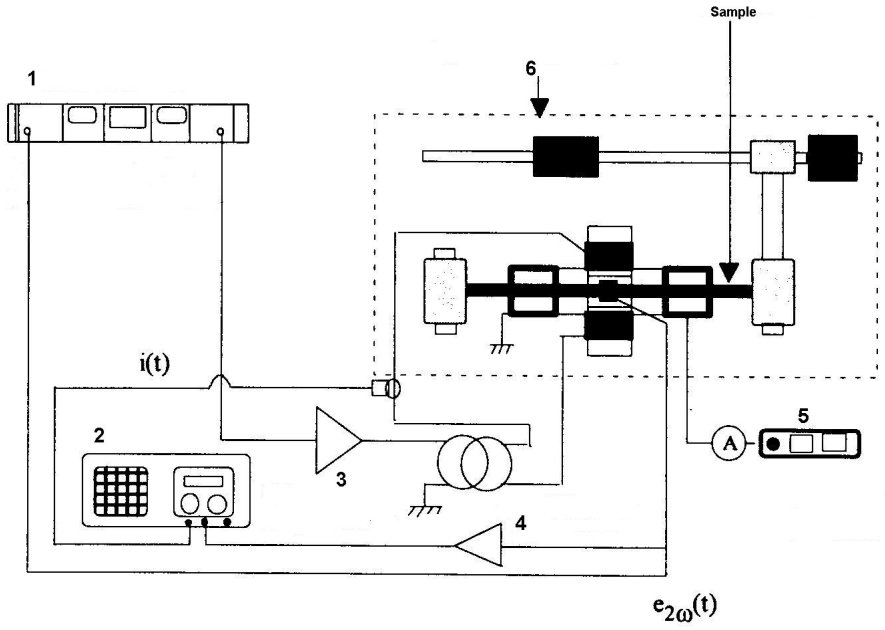

Figure 4.6: The arrangement of SAMR measurement

Fortunately, there are several parameters which remain constant during the practical realization that makes it easier to obtain the λ_s values. For instance, when a tensile stress is applied and when $\lambda_s > 0$ the anisotropy field is going to increase $\Rightarrow$ $e_{2\omega}$ will increase (see Eq. 4.16). This change can be compensated by the increase of $H_{||}$ to keep $e_{2\omega}$ constant. Supposing, there is a linearity between the applied stress (σ) and $H_{||}$ furthermore $e_{2\omega}$ and $H_\perp$ are constants the λ_s can be written as:

$$\lambda_S = -\frac{1}{3} \cdot \mu_0 \cdot M_S \cdot \frac{\Delta H_{||}}{\Delta \sigma}. \tag{4.17}$$

Fig. 4.6 shows the scheme of SAMR measurement:

1. In order to be able to detect the very small value of $e_{2\omega}$, a lock-in amplifier is employed. Its internal oscillator is used as phase reference and provides the transverse sinusoidal magnetic field ($H_\perp$).
2. Oscillograph to visualize $2f$ signal. When $H_\perp$ is excited by f Hz the captured signal has a frequency of $2f$.
3. Power amplifier.
4. Linear amplifier.
5. DC current source to produce the $H_{||}$ ($H_{||} = 350 \cdot I_{||}$).
6. Magnetic circuit. The stress is applied by means of lever arm.

4.6 Hysteresis measurements on single ribbon (single sheet tester)

In most of the cases, the ribbons were annealed under magnetic field or under stress in a single ribbon form (10-30 cm) respectively, due to the thermal properties (different homogeneity) of furnaces employed (see Sec. 4.10 and 4.7). In addition, all ribbons were quite brittle after annealing, preventing them from being reeled into toroidal form. Furthermore the winding can induce stress in the ribbon, perturbing the hysteresis behaviors.

Hence the hysteresis investigations were carried out on single ribbon form using the "single sheet tester" technique. This experimental set-up consists (Fig. 4.7):

1. Signal generator (oscillator).
2. Power amplifier.
3. Impedance matching transformer.
4. Magnetic circuit.
5. Oscillograph with a resolution of 12 bits.
6. PC. The measurement is computer automatized by GPIB standard.

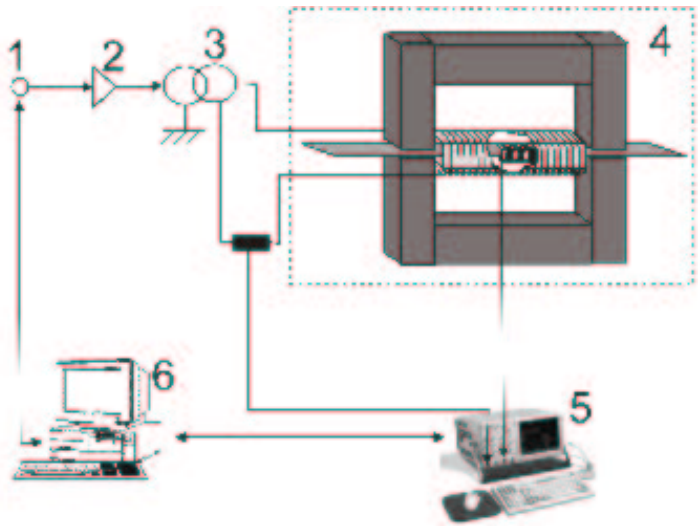

Figure 4.7: Schematic diagram of single sheet tester.

4.7 Low frequency hysteresis measurements as a function of temperature

An arrangement was designed and built in order to measure hysteresis cycles as a function of temperature. The measurement allows us to investigate the coercive field (H_C), the magnetic remanence (B_r), the magnetic saturation at the applied external magnetic field $\sim 800\,A/m$ (B_s), the magnetic losses (P) and the permeability (μ). All the measurements were done at 37 Hz using this arrangement. The in-situ hysteresis measurements were realized during the whole heating-cooling annealing process. The temperature is limited by the physical structure of the furnace (water cooled, bifilar winded, stainless steel tube) up to about 600°C.

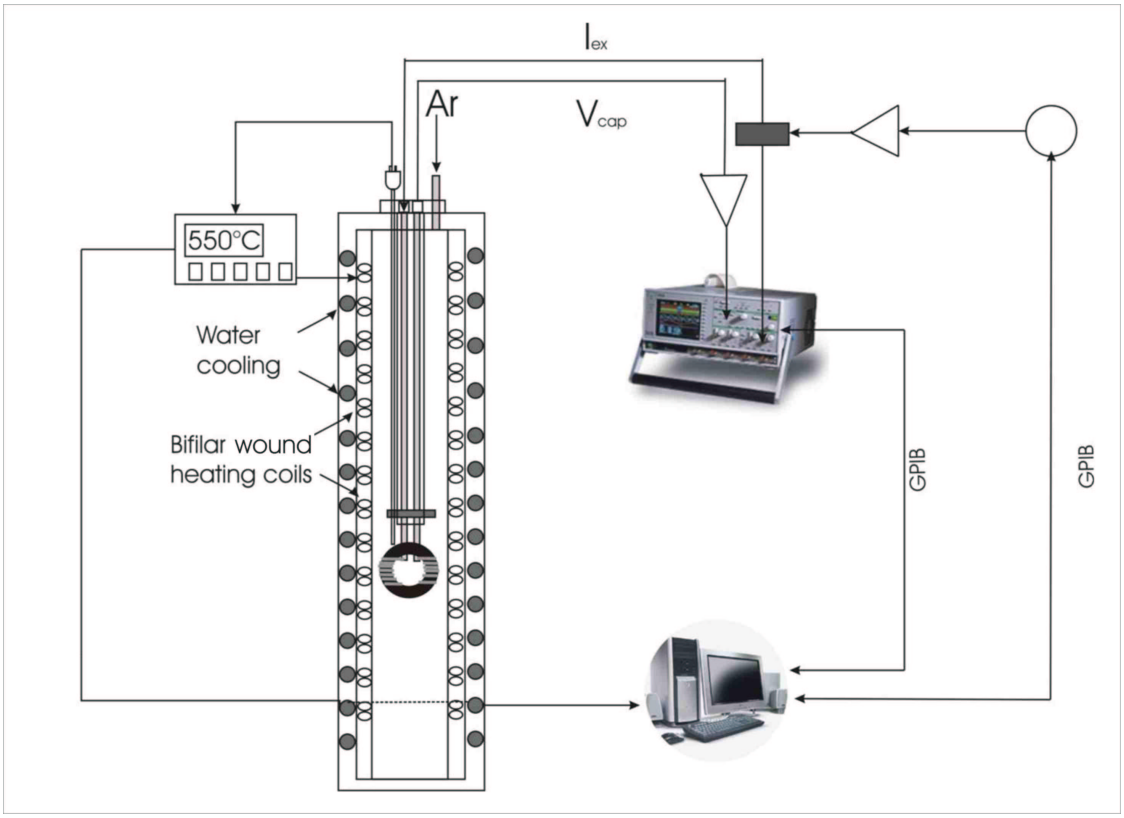

Figure 4.8: The schematic diagram of high temperature in-situ hysteresis measurement arrangement.

The arrangement (see Fig. 4.8) is composed of a wave function generator, which provides the frequency and shape of wave signal. In our case the exciting field always had triangular form, because the distribution of points in the hysteresis loop is more homogeneous compared to sine wave form, for which the density of points is low around the coercive field. A power amplifier (Kepco 400W) can ensure the required exciting current. The samples were always investigated in toroidal form. Insulation of exciting and measuring coils against electrical contact was solved using high temperature fiber quartz coat. The primary winding produces the exciting magnetic field which can be written as $H_{ex} = \frac{N_1 i}{l}$, where N_1 is the number of primary turns, i is the applied current and l is the core average length. A known resistance (R) is used to measure the applied current using a 12 bit oscilloscope. The secondary voltage (U) is proportional to the number of secondary turns (N_2) and the cross-section of sample (S_{sample}). The magnetic induction in the sample is calculated as: $U = -\frac{d\phi}{dt}$ and $B = \frac{\phi}{S_{sample} N_2}$, thus $B = \int \frac{U}{N_2 S_{sample}} dt$. The calculation is made by the controller program using the current timebase and calibers of oscilloscope. All the heating-cooling cycle is automatized by MATLAB [68] using GPIB standards. A hysteresis cycle was taken at each 7 seconds to provide some relaxation time for the material in order to minimize the influence of applied magnetic field during annealing.

A vertical tubular furnace was used to heat the samples, controlled by a digital thermo

regulator. A bifilar heating coil was wound around the stainless steel tube, in order to extinguish the magnetic field produced by heating current. Furthermore this whole structure is enclosed in a water cooled outer shield in order to control accurately the heating and cooling rate and to minimize the temperature overshoots at plateau. The magnetic core was situated in the homogeneous zone of furnace and the thermocouple was always touching the surface of the investigated sample during measurement.

It should be noted that transversal magnetic field annealing can be carried out with the same furnace using a perpendicular 0.3 m in diameter Helmholtz coils attachment. In our case this coil set is about 35 kg which can provide a homogeneous perpendicular magnetic field to the furnace axis with a maximum value of 20 kA/m (see Fig. 7.5). In such cases the samples were always in single ribbon form with a length of 12 cm, positioned in the homogeneous zone of temperature and magnetic field.

4.8 Faraday Balance

A Faraday Balance is an apparatus for the detection of magnetization by measuring the force on a sample in a homogeneous gradient magnetic field generated by an electromagnet between two pole caps with dedicated design (Faraday pole caps). The force can be measured with an analytical balance (resolution of the order of 10^{-2} milligram or better) at which the sample is suspended. The quartz sample holder is suspended by a silver chain whose parts are resistive against high temperature and has no magnetic contributions. The sample heating is done by a current heated tubular furnace.

The force induced by the magnetic moment (M) in the inhomogeneous field can be calculated as

$$F = M * \frac{dB_{\mathrm{x}}}{dz}.$$

As the gradient $\frac{dB_x}{dz}$ is known from geometry of poles and applied exciting current (the calibrating constant proportional with these parameters), the moment is determined from the force. The results presented in this work were realized by an apparatus which withstands measurements up to 800°C.

4.9 Differential thermal analysis (DTA)

The DTA method is used to obtain information of chemical reactions, phase transformations, and structural changes that occur in a sample during a heat-up or a cool-down cycle. The DTA measures the differences in energies released or absorbed, and the changes in heat capacity of materials as a function of temperature.

The sample holder cup (made of high purity alumina) is made for the thermocouple to be well surrounded by the sample without physical contact (see Fig. 4.10). The measured signal is due to the temperature difference (ΔT) between the reference and sample thermocouple. When an endothermic reaction is encountered, the temperature of the material decreases while the energy is absorbed. As for the exothermic reactions, the temperature of the sample starts to rise quickly above the outer temperature. The observed signals are showed in Fig.4.10. The area A on Fig. 4.10 is proportional to the heat of the reaction:

$$\Delta H = K \cdot A = K \int \Delta T dt. \tag{4.18}$$

The constant K comprises many factors, including the thermal properties of the sample (heating rate, etc.), and varies with temperature. All DTA investigations were made at Faculty of Materials Science and Engineering in Warsaw University of Technology by the courtesy of E. Fazakas MSc.

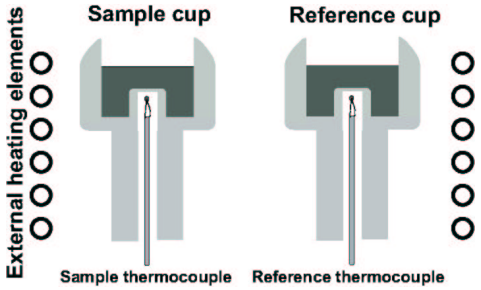

Figure 4.9: Sketch of DTA cell

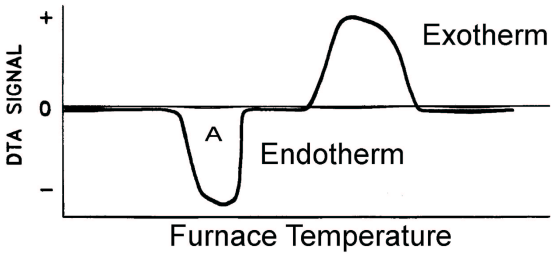

Figure 4.10: The various reactions generated signals in DTA.

4.10 Elongation measurements of soft magnetic ribbons during stress annealing

Elongation ($\frac{dl}{l}$) investigations of single ribbons under applied mechanical stress during annealing were carried out in a horizontal tubular furnace. The instrument is available in CNAM (Conservatoire National des Arts et Métiers), Paris. The furnace shown in Fig. 4.11 is composed of a 2 m long and 60 mm in diameter stainless steel tube. The two ends of the tube are fixed by screws and removable in order to easily take in and out the investigated sample. Sample heating is made in a 12 mm wide copper bore in the middle of the furnace surrounded by a non-inductive heating coil. The ribbon is located in the middle of this bore. The furnace structure ensures a favorable temperature profile along the furnace axis (for further details see in [69]). Practically, the homogeneous temperature zone is about 25-30 cm considering the fact that the furnace temperature deviation is about -2 °C in 20 cm. The above mentioned copper bore is simultaneously wound by another single coil which can produce a longitudinal magnetic field with a maximum value of about 800 A/m, so longitudinal magnetic and/or stress annealing could be carried out during thermal annealing. Even if that maximum value

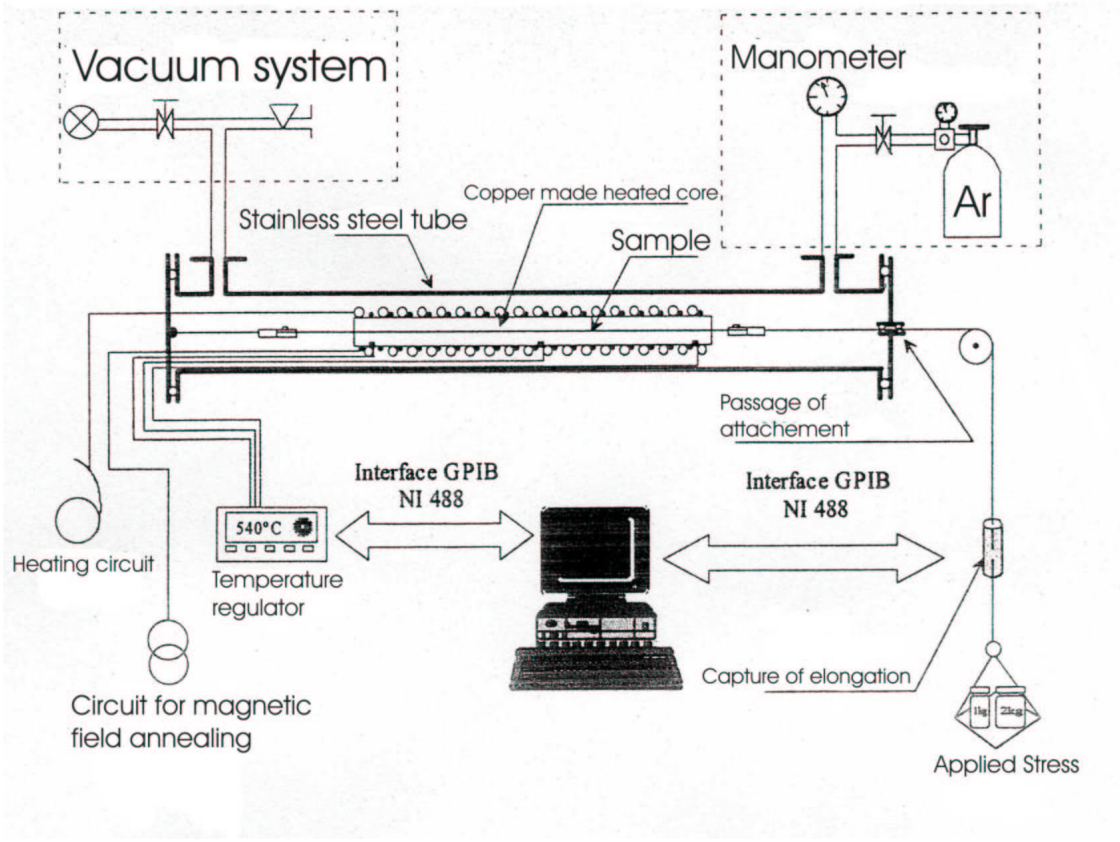

Figure 4.11: The scheme of horizontal arranged furnace. Elongation is captured at each second in order to have very high data density for further mathematical analysis (derivation for instance).

of applied field is one order of magnitude smaller compared to that in Sec. 4.7 the inner field is found to be high enough to expose its influence due to the much smaller demagnetization factor (length of sample is about 1 m). All thermal treatments were done under Ar protecting atmosphere. Ribbon was attached to a thin stainless steel bar which has a passage at one end of tube (see 4.11). The desired mechanical stress is applied using weights of known mass.

Frame of measurement allows capture of the signal of thermocouple and elongation (using linear variable differential transformer) employing PC linked voltmeters by GPIB standard card. In order to allow digital derivation of $(\frac{dl}{l})$ vs. T curves, a high density of data points is required: 1 point / sec was recorded using voltmeters controlled by a qbasic program, written for this purpose.

5 Results and Discussion

5.1 Crystallization and structure

5.1.1 $(Fe_{100-x}Co_x)_{73.5}Si_{13.5}Nb_3B_9Cu_1$

In order to choose the proper annealing treatment, differential thermal analysis (DTA) investigations were performed (Fig. 5.1). T_{x1} shows that the variation of Co content affects the stability of alloys against crystallization. The crystallization onset temperature of specimens increases slightly up to x = 30, however, for higher Co-containing alloys, the thermal stability of both amorphous and nanocrystalline samples decreases continuously (for exact values see in Table 5.1).

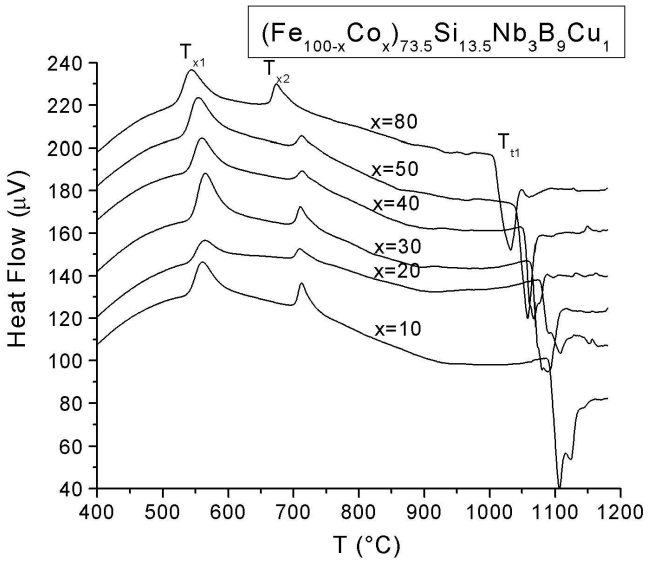

Figure 5.1: Heat flow as a function of temperature obtained by means of DTA. Heating rate was 20°C/min. Baseline is shifted to eye view.

Conventional X-ray diffractometry was used to estimate the lattice structure, grain size and crystallized fraction of precipitated phases during the first (T_{x1}) crystallization stage. X-ray results of samples annealed at 530°C for 1 hour are plotted in Fig. 5.2. BERTA [59] X-ray software was used for computing data. The precipitated nanograins have an average size of 11-13 nm whereas the crystallized phase is in the range of 50-60 % for 10% $<$ x $<$ 50%, $v \approx$ 30% for x=80%. Table 5.2 summarizes the results of annealing on the structural parameters. For all cases the lattice is body centered cubic (BCC) structure is observed by

Table 5.1: Transformation temperatures of $(Fe_{100-x}Co_x)_{73.5}Si_{13.5}Nb_3B_9Cu_1$alloys.

x (%)	T_{X1}(°C)	T_{X2}(°C)	T_{t1}(°C)
0	525	620	-
10	529	712	1107
20	524	709	1107
30	542	709	1080
40	533	714	1067
50	529	713	1058
80	503	675	1033

XRD, however the presence of DO_3 superstructure (for x=0, it was reported in [70]) was found in all Co containing alloys using WAXS technique (Fig. 5.3). In this structure (for x=0) the Fe atoms are located at two nonequivalent $(\frac{1}{4},\frac{1}{4},\frac{1}{4})$ and $(\frac{1}{2},\frac{1}{2},\frac{1}{2})$ and the Si atoms in the (0,0,0) crystallographic positions and due to this lower symmetry of DO_3, the diffractogram contains extra reflections as compared to single BCC phase. It must be noted, that the presence of DO_3 could not be detected by XRD, which can be attributed to the similar scattering factor of Fe and Co element. The higher inclusion of Co atom in the DO_3 structure causes changes in relative intensities, as reported in [71], using neutron-diffraction technique. Fig. 5.3 b) also shows the shift in the peak position to higher angles as a function of Co content, denoting the decrease in lattice parameter (see Table 5.2). The presence of DO_3 structure in these Co-doped alloys assumes that the soluting Co atoms replace the Fe elements only in the nanophase not inflecting the position of Si atoms in the superlattice.

Table 5.2: Grain sizes, lattice parameters and crystallized fraction of $(Fe_{100-x}Co_x)_{73.5}Si_{13.5}Nb_3B_9Cu_1$alloys.

	530°C for 1 hour		
x (%)	D_{XRD} (nm) (±1)	a (Å) (±0.005)	v_X (%)(±5)
10	11.5	2.835	53
20	12	2.832	52
30	12.5	2.829	51
40	11	2.826	58
50	12	2.823	60
80	11	2.811	40

The beginning of a second crystallization stage (T_{x2}) can be observed around 700°C (see Fig. 5.1). These phases might be the same magnetically hard refractory borides like Fe_2B, $(FeCo)_2B$, Fe_3B and $(FeCo)_3B$, which were reported earlier in the original Finemet $(Fe_{73.5}Si_{13.5}Nb_3B_9Cu_1)$ alloy. At more elevated temperature, negative heating flow i. e. endothermic reaction is found, which is a sign of melting. Interestingly it can be observed, that there are two peaks close to each other in the curves around this T_{t1} temperature. This fact may be a sign of two nanocrystalline phases with similar chemical compositions, nevertheless

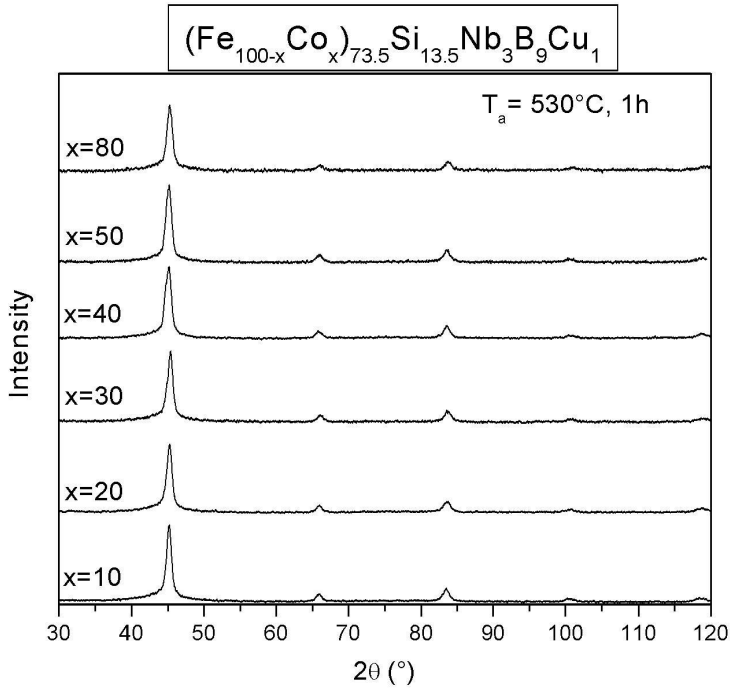

Figure 5.2: X-ray patterns of $(Fe_{100-x}Co_x)_{73.5}Si_{13.5}Nb_3B_9Cu_1$alloys. Baseline is shifted to better view.

DTA could not distinguish the two very close T_{x1} crystallization events. However considering the high temperature at which the phenomenon is observed, decomposition of $\alpha - FeCoSi$ cannot be excluded either. The above described crystallization occurrences are listed in Table 5.1.

Fig. 5.5 shows the images of samples taken by transmission electron microscopy (TEM) from dark field geometry. After statistical treatment of the dark field TEM pictures, it is clear that for specimens with lower Co content, there is a smaller distribution in grain size around the average value compared to higher Co content alloys (Fig. 5.4). Furthermore, it seems that for the sample with a Co ratio x=80%, nanocrystals tend to form aggregates, which is an important point, since the coercive field depends drastically on the grain size.

Using Mössbauer spectroscopy in transmission geometry, we can have element specific analysis in the amorphous and crystalline fractions, since this method is only sensitive for the Fe element while X-ray can not distinguish the Fe and Co atoms due to its very similar scattering behaviors. Mössbauer spectra were fitted using MOSFIT evaluation program[72]. Fig. 5.6 shows the Mössbauer spectra recorded at 300 K of nanocrystalline samples having different Co-content obtained by annealing at 530°C for 1 hour. Examination of Fig. 5.6 shows that the Co content significantly affects the hyperfine structure: the outer part of Mössbauer spectra suggests that the variation in Co content in the parent alloy leads to the formation of different phases after nanocrystallization.

Fig. 5.7 (on the left) shows that $< B_{\mathrm{hf}} >$ for both crystalline and amorphous phases vary with Co content, indicating differences in the environments around Fe-atom in the studied

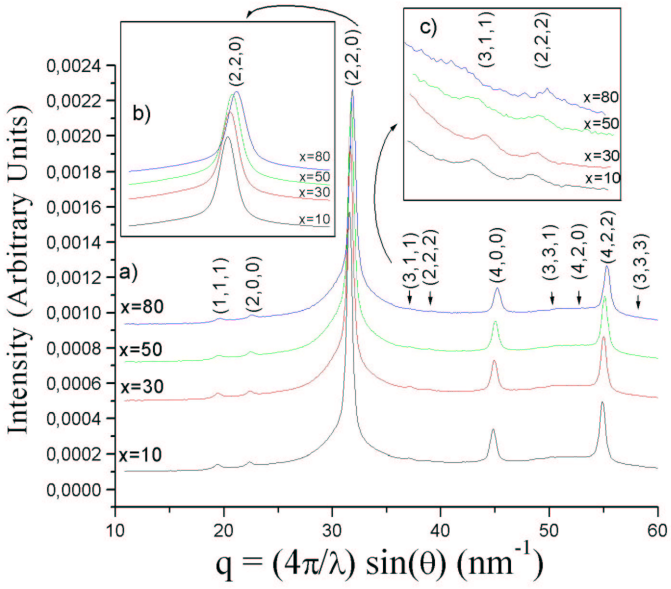

Figure 5.3: WAXS result of $(Fe_{100-x}Co_x)_{73.5}Si_{13.5}Nb_3B_9Cu_1$ (annealed at 530°C, 1h) samples. Extra reflections of DO_3 superstructure are observed in all compositions.

specimens. The low values of $< B_{hf} >$ observed for the residual amorphous matrix (as compared to nanocrystalline phase) are consistent with the presence of boron as near-neighbors of Fe [73]. Other authors correlate this smaller hyperfine fields to an interphase region around the nanocrystallites [74, 75]. The high surface volume is due to small grain size, which makes a relevant contribution to the spectra. The hyperfine field of the crystalline component suggests that below 20% of Co in the parent alloy, very small amount of Co is diffused into the crystalline phase. Increasing from 20 to 30 % of Co in the parent alloy, the hyperfine field of both components shows an increase of about 4 - 5 T. One can distinguish two main domains: for x $<$ 20 %, the shape of outer lines is consistent with the presence of a Fe(Co)Si phase while a bcc-FeCo phase can be suggested for x $>$ 20%. Fig. 5.6 shows the variation of hyperfine

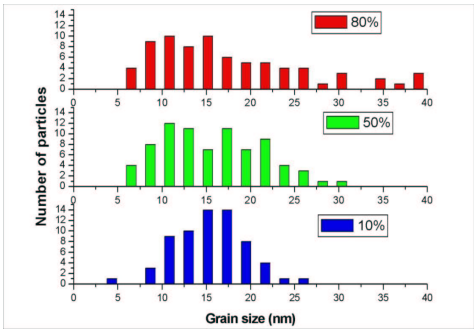

Figure 5.4: Distribution of grain size of $(Fe_{100-x}Co_x)_{73.5}Si_{13.5}Nb_3B_9Cu_1$ alloy annealed at 530°C for 1 hour.

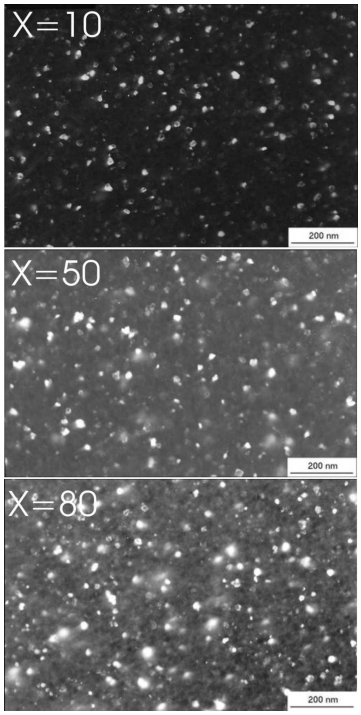

Figure 5.5: Dark field TEM pictures of selected $(Fe_{100-x}Co_x)_{73.5}Si_{13.5}Nb_3B_9Cu_1$ samples annealed at 550°C/1h.

field $< B_{\mathrm{hf}} >$ for both crystalline phase and residual amorphous matrix. The Mössbauer spectra of nanocrystalline samples exhibit a complex hyperfine structure, which generally can be attributed to amorphous, interphase and crystalline regions, with well separated peaks in hyperfine field distribution. Nevertheless, in the case of Co-free and Co-added Finemet alloys, the presence of non-ferrous Si element lowers the hyperfine field contribution of nanophase resulting in an overlap with the amorphous and interphase contributions.

Fig. 5.7 (on the right) shows the relative fraction of Fe in the crystalline phase estimated from Mössbauer spectra and volumetric fraction of the nanograins estimated from the areas of XRD as a function of Co content. It is found that the relative fraction of Fe in the nanocrystalline phase decreases with x=10, 20 and 30. As for $x > 30\%$, the larger the Co content, the higher the relative fraction of Fe in the crystalline phase. This can be understood in terms of migration of more and more Fe to the crystalline phase in order to precipitate the more stable $Fe_{70}Co_{30}$ like compound. Once the percentage of Co in the parent alloy rises above 30%, the lattice parameter of the precipitated crystalline phase is close to the stable stoichiometric Fe_7Co_3 like phase (K_1=100$\frac{kJ}{m^3}$). Thus in the studied alloys, there is a tendency to form and to stabilize $Fe_{70}Co_{30}$ like phase which is magnetically harder than $Fe_{80}Si_{20}$ phase (K_1=8$\frac{kJ}{m^3}$). This suggestion is confirmed by the increase of Hc, see in Sec. 5.2. It is worth noting that as shown in Fig. 5.7, for above 30% of Co in the parent alloy one can observe a considerable increase of relative fraction of Fe in the crystalline phase, which is also consistent with the presence of $Fe_{70}Co_{30}$ like phase. Indeed, more Fe atoms migrate to crystalline phase, thus almost leaving the residual amorphous matrix without Fe atoms. For higher Co content in the parent alloy, the relative fraction of Fe in crystalline grains is rather

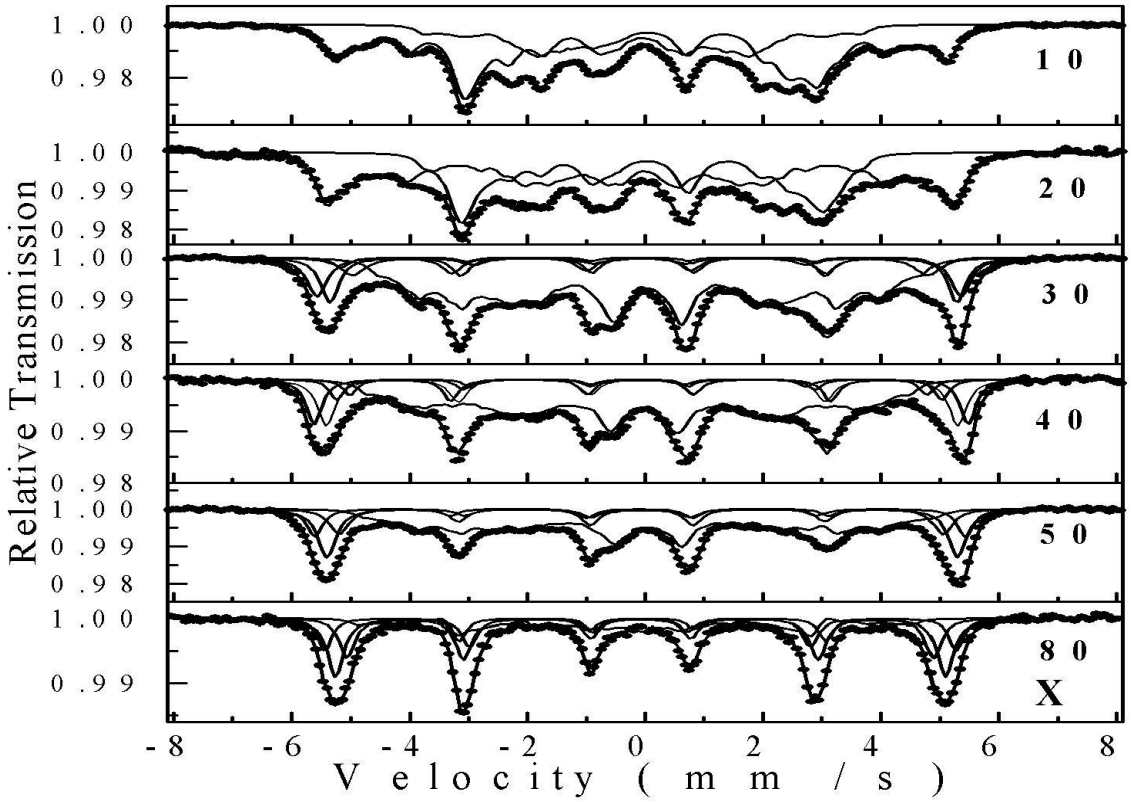

Figure 5.6: Mössbauer spectra of $(Fe_{100-x}Co_x)_{73.5}Si_{13.5}Nb_3B_9Cu_1$ alloys recorded at 300 K of nanocrystalline samples having different Co-content obtained by annealing at 530°C for 1 hour

high, which can be explained in terms of the amorphous matrix almost exhausted in Fe in the process of nanocrystallization, as suggested in an earlier work [75].

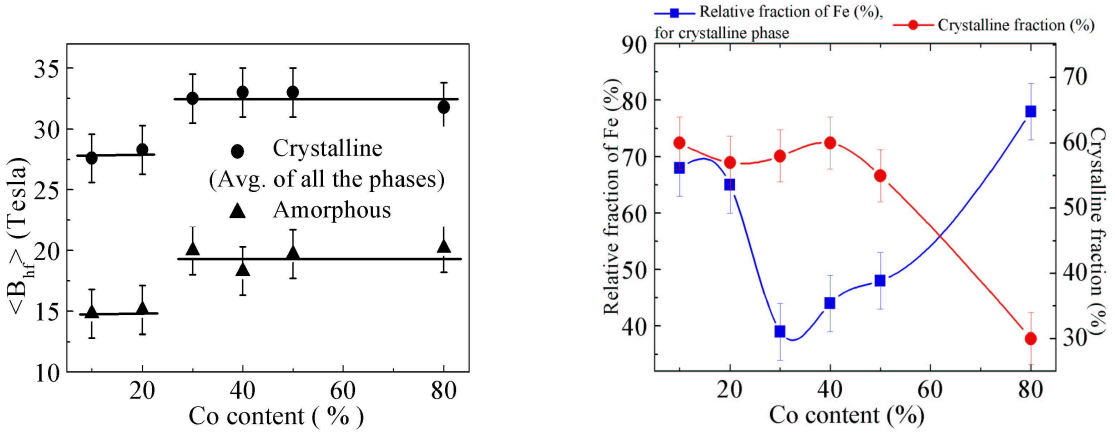

Figure 5.7: On the left: Variation of hyperfine field($< B_{\rm hf} >$) of the residual amorphous component and for crystalline components (average $< B_{\rm hf} >$ of all the crystalline components). On the right: variation of relative fraction of Fe and volumetric fraction present in the nanocrystalline $(Fe_{100-x}Co_x)_{73.5}Si_{13.5}Nb_3B_9Cu_1$ alloys ($T_a = 530°C$, $1h$) with varying Co content, calculated from Mössbauer spectra. Continuous lines are guides to the eye.

5.1.2 $(Fe_{100-x}Co_x)_{78}Si_9Nb_3B_9Cu_1$

As DTA records show in Fig.5.8, the first crystallization temperature (T_{x1}) varies little (about 30K) with the Co content, similar to previous alloy systems, however the crystallization onset temperature of specimens decreases continuously with Co addition (see for values in Table 5.3). X-ray diffractometry was used to identify the lattice structure of this precipitating phase. For this purpose samples were annealed at 530°C for 1 hour. Diffractograms were fitted using BERTA [59] X-ray evaluation software. The structure of the nanocrystallized phase was identified as body centered cubic (BCC) lattice, however the presence of DO_3 superstructure is not excluded, similarly to above discussed alloys. Fig. 5.9 (a) and (b) show the relevant parameters obtained after fitting of the diffractograms. It can be said that the tendency of lattice parameters lowers as the Fe replaced with Co. Unfortunately, both Si and Co have the same influence on lattice parameter in the solid solution of Fe (see for instance in [76]), thus it is difficult to determine the Si and Co concentration in the nanocrystalline phase, however its increasing presence in the nanophase is certain.

Grain size has a tendency to increase up to x=75% with a diameter from about 13 to 17 nm and after that clearly decreases. As for the crystallized fraction, it stays practically constant up to x=80% with about 60 % of precipitated fraction (v). For higher Co content compositions v decreases down to about 40%. This is due to the effect mentioned above, namely the Fe atoms migrate to crystalline phase, thus almost leaving the residual amorphous matrix without Fe atoms. With the evaluation of crystallization the nanophase is exhausted in Fe, which stops the nanocrystallization process. Within experimental errors the first near

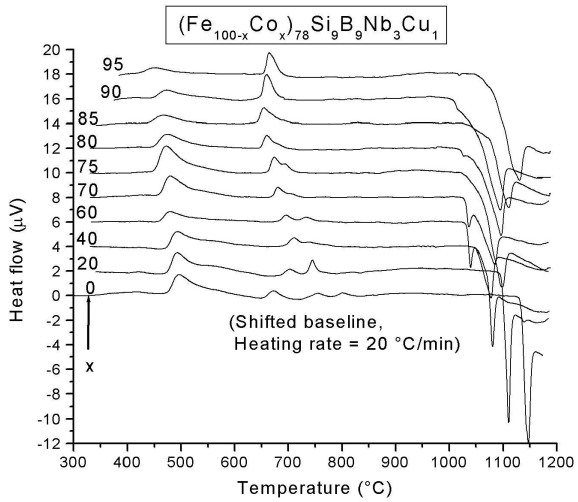

Figure 5.8: DTA results of $(Fe_{100-x}Co_x)_{78}Si_9Nb_3B_9Cu_1$alloys.

neighbor distance in the residual amorphous matrix remains unchanged (0.249 nm) showing that the studied samples have similar mass density.

Signs of second crystallization (T_{x2}) can be observed at around 700°C (see Fig. 5.8). For the sample x=0, participation of several new phases are indicated by small humps. These phases are probably the same magnetically hard refractory borides like Fe_2B and Fe_3B which are also present in $(Fe_{100-x}Co_x)_{73.5}Si_{13.5}Nb_3B_9Cu_1$ alloys. At more elevated temperature negative heating flow i. e. endothermic reaction is found, similarly to $(Fe_{100-x}Co_x)_{73.5}Si_{13.5}Nb_3B_9Cu_1$ alloys.

5.1.3 $(Fe_{100-x}Co_x)_{84}Nb_{3.5}Zr_{3.5}B_8Cu_1$

These alloys are derivated from $Fe_{44}Co_{44}Zr_7B_4Cu_1$ (Hitperm) composition firstly reported in [20]. The advantage of this particular composition is very high induction and Curie temperature (unfortunately its coercivity is huge compare to that of Finemet). It is also important to notice that Hitperm is a direct evolution of Nanoperm ($Fe_{86}Zr_7B_6Cu_1$) alloys.

DTA results in Fig. 5.10 indicate the crystallization temperatures of $(Fe_{100-x}Co_x)_{84}Nb_{3.5}Zr_{3.5}B_8Cu_1$ alloys. Events of first crystallization occur at 522°C and decrease continuously with Co addition. X-ray diffractometry results (Fig. 5.11) carried out on samples annealed at 510°C during 1 hour reflect the presence of BCC lattice structure in the nanocrystalline phase. Size of nanocrystals changes from 7.2 nm for x=10 down to 6.5 nm in x=50 while crystallized fraction increases with Co. Average atomic distance seems to have the tendency to increase with x, while the short range order (SRO) distance clearly increases with more Co element. Later behavior can be explained by the fact that crystallization temperature decreases with x. This can be also the reason for the increase of crystallized fraction. It must be noted that despite the above reported similar tendencies of v , atomic distance in amorphous and SRO distance the size of nanograins exhibits opposite i. e. decreasing trend (see in Table 5.4).

The lattice constant was found to be higher compared to atomic distance in FeCo crystals (see in Fig. 5.12) as described in [76] (however these data also need correction! i.e. $a_{Fe} = 2.866$

x	T_{x1}(°C)	T_{x2}(°C)	T_{x3}(°C)
0	496	672	755
20	493	703	745
40	492	710	738
60	478	695	733
70	479	681	703
75	472	673	693
80	473	660	-
85	466	654	-
90	473	659	-
95	450	664	-

Table 5.3: Crystallization, melting and Curie temperatures of $(Fe_{100-x}Co_x)_{78}Si_9Nb_3B_9Cu_1$ alloys.

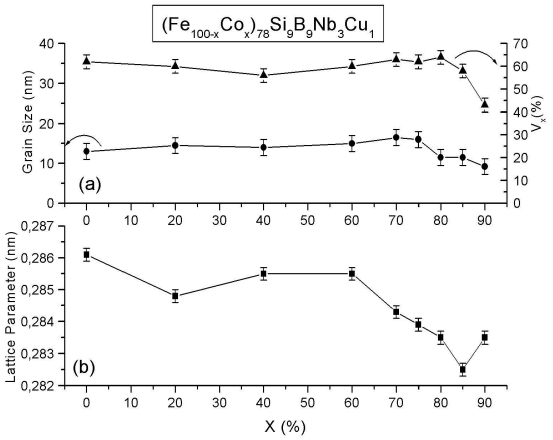

Figure 5.9: Lattice parameters, grain sizes and crystallized fraction as a function of Co content. Annealing temperature was 530°C for 1h.

x	Lattice Parameter (Å)	D (nm)	V_x (%)	Atomic distance in amorphous (Å)	SRO distance (nm)
10	2.878	7.2	47	2.53	1.1
20	2.877	7.1	52	2.55	1.3
30	2.876	6.8	55	2.55	1.4
40	2.875	6.8	65	2.55	1.4
50	2.874	6.5	65	2.6	1.5

Table 5.4: Parameters deduced from X-ray spectra of $(Fe_{100-x}Co_x)_{84}Nb_{3.5}Zr_{3.5}B_8Cu_1$ alloys annealed at 510°C for 1 hour.

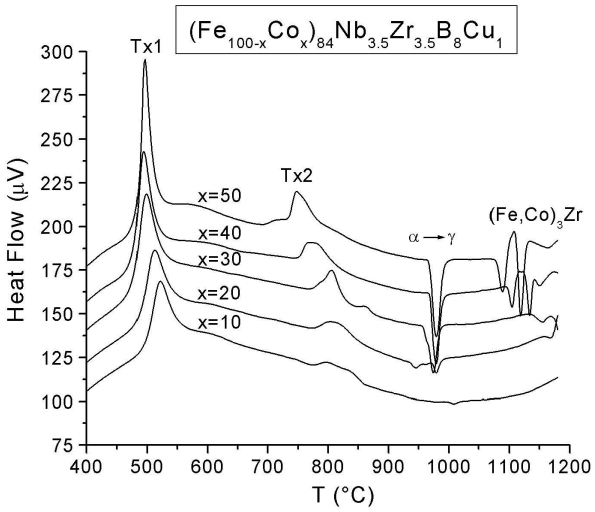

Figure 5.10: Differential thermal analysis (DTA) curves of $(Fe_{100-x}Co_x)_{84}Nb_{3.5}Zr_{3.5}B_8Cu_1$ alloys. Two discrete peaks and a lattice transition can be clearly observed. Baseline is shifted.

and not $a_{Fe} = 2.860$, etc.). Only Fe and Co elements are expected to compose the nanophase in BCC form, therefore another annealing treatment was made at 600°C for 1 hour and measured by XRD in order to compare and interpret this phenomena. Structural data from X-ray diffractograms are shown in Table 5.5. Interestingly the lattice parameters of these samples (600°C, 1 hour) correspond to atomic distance in FeCo crystals described in [76]. T. Kemény et. al. [73] reported the presence of B and Nb in the Fe nanocrystal (Nanoperm), which was concluded from hyperfine field components found in the region from ~ 20 to $\sim 32\,T$. Indeed, atom-probe experiments showed rejection of Nb to the matrix, but detect $\sim 5\,at\%$ B in the nanocrystal [77]. Others assign the higher contribution of this hyperfine region to interface effect, due to the small size of nanocrystalline grains [75].

These anomalous results in lattice parameter of crystallized phases could be explained by the soluted presence of B, Nb and Zr elements in the nanocrystalline, distorting the BCC solid state structure. Annealing the material at 600°C for 1 hour, which results in much higher diffusion speed compared to 510°C can cause these impurities to be expelled from the nanophase to residual amorphous phase. In our case, the XRD results may assume the presence of that Nb, B and Zr elements nanograins indicated by the larger lattice parameter of samples, annealed at lower temperature, without measuring the hyperfine distribution of Fe element by Mössbauer spectrometry. Indeed, Mössbauer investigations to distinguish the contribution of three soluted non ferromagnetic components are in progress.

It is important to notice that the calculated contribution of nanophase is around 90 %, which is overestimation since Fe and Co contribution in the whole alloy is only 84 %. This phenomenon is preliminary because the interfered X-rays from atoms in amorphous are suppressed by the order of higher signal from lattice, secondly due to high B content in the residual phase which provokes much smaller scattering intensity of X-ray (I) in as much as $I \sim \rho$ and $\rho \sim Z$, where $\rho(r)$ is the electron density and Z is the atomic number.

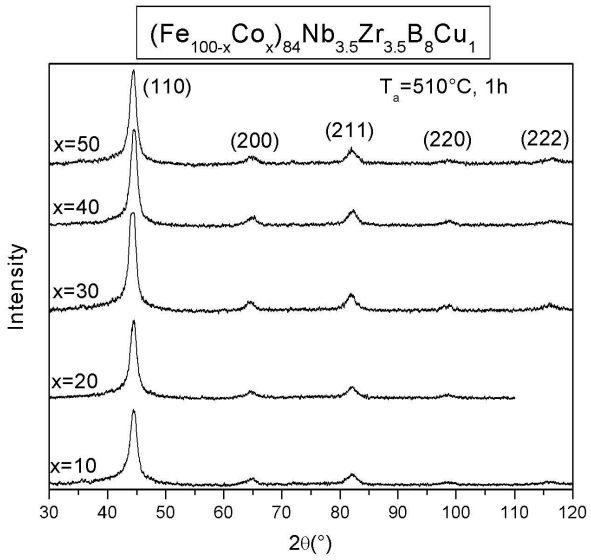

Figure 5.11: X-ray patterns of $(Fe_{100-x}Co_x)_{84}Nb_{3.5}Zr_{3.5}B_8Cu_1$alloys. Baseline is shifted to better view. The precipitated phase nanophase is BCC for all cases, the corresponding (hkl) planes are indicated above peaks.

T_{x2} shows the same trend as T_{x1}, namely it slightly decreases with Co addition (see Table 5.6). We have no information about the precipitated phases at that temperature. In [17] these events are attributed to the precipitation of $(Fe, Co)_3Zr$ phases which is probably also the case for our alloys. Magnetic transition ($\alpha \Rightarrow \gamma$) is indicated by endothermic DTA peaks at around 1000°C as in Si containing alloys. For x=50 this transition takes place at 980°C, exactly at the same value as reported for Hitperm [20], attesting that the composition of precipitated nanophase is presumably the same.

x	Lattice Parameter (Å)	D (nm)	V_x (%)
10	2.862	22	90
20	2.868	21	90
30	2.865	23	95
40	2.858	24	95
50	2.856	25	92

Table 5.5: Extracted parameters form X-ray spectra of $(Fe_{100-x}Co_x)_{84}Nb_{3.5}Zr_{3.5}B_8Cu_1$ alloys annealed at 600°C for 1 hour. Obtained values indicate that the annealing temperature was too high. There is a very small contribution of residual amorphous after the heat treatment.

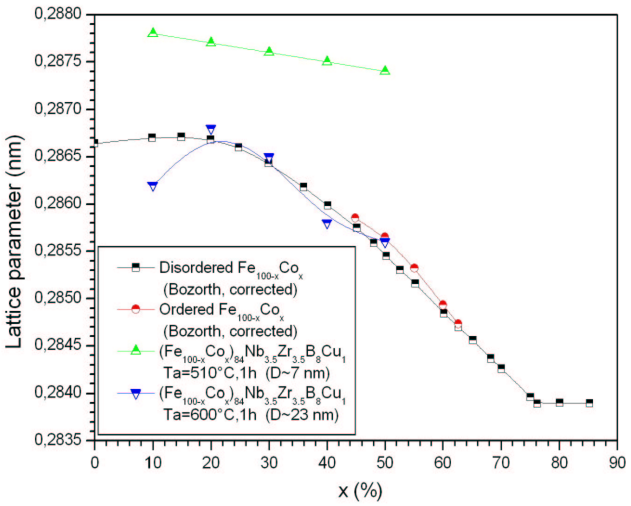

Figure 5.12: Lattice parameter of FeCo crystal phase versus Co content in $(Fe_{100-x}Co_x)_{84}Nb_{3.5}Zr_{3.5}B_8Cu_1$ alloys annealed at various temperatures and compared with $(Fe_{100-x}Co_x)_{100}$ binary alloy (after correction from [76]).

x	T_{x1}(°C)	T_{x2}(°C)	$\alpha \Rightarrow \gamma$ (°C)
10	522	770	1008
20	512	770	980
30	498	768	975
40	492	748	979
50	496	730	980

Table 5.6: Crystallization temperature values of $(Fe_{100-x}Co_x)_{84}Nb_{3.5}Zr_{3.5}B_8Cu_1$alloys extracted by meaning of DTA. The heating rate was 20 °C/min.

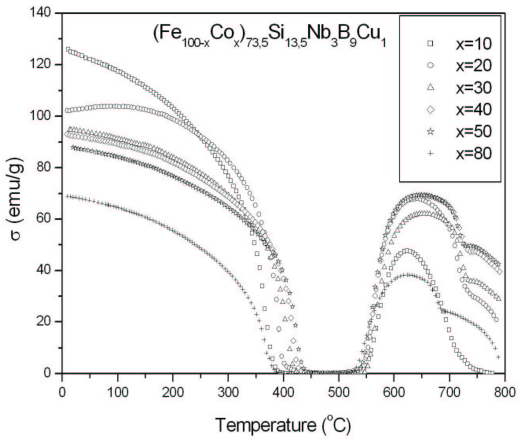

Figure 5.13: Thermo-magnetization curves of as-cast $(Fe_{100-x}Co_x)_{73.5}Si_{13.5}Nb_3B_9Cu_1$ alloys recorded at a heating rate of 10°C/min.

5.2 Magnetic properties

5.2.1 $(Fe_{100-x}Co_x)_{73.5}Si_{13.5}Nb_3B_9Cu_1$

Thermo-magnetic curves obtained by Faraday balance drawn in Fig. 5.13 show that the crystallization temperature varies little (about 20 K) with the cobalt content (evidently DTA curves reflect same result). As suggested by the Curie point around 720-750°C, the first crystalline phase has a composition that is almost independent of that of the amorphous precursor at least while $x \leq 50\%$ (see also Tab. 5.7). In contrast, the second crystalline phase has a Curie point varying from 800 to almost 900°C as far as it can be linearly extrapolated from a $\sigma^{1/\beta}$ plot (with $\beta = 0.36$). For x=0, 10% the second crystallization stage (Fe_2B) is close to the first one, thus T_{C2}^{cryst} can not be deduced from the thermomagnetic curves.

x (%)	T_C^{am}(°C)	T_{C1}^{cryst}(°C)	T_{C2}^{cryst}(°C)
0	318	600	-
10	367	700	-
20	392	720	811
30	415	732	859
40	406	729	847
50	427	722	876
80	365	681	788

Table 5.7: Transformation temperatures of $(Fe_{100-x}Co_x)_{73.5}Si_{13.5}Nb_3B_9Cu_1$alloys evaluated from the results of Faraday balance.

The compositional dependence of the specific magnetization is represented in Fig. 5.14 (top). As it is established in Fe-Co based amorphous alloys, the magnetization of as-quenched samples continuously decreases with increasing Co content. In contrast, annealing produces a

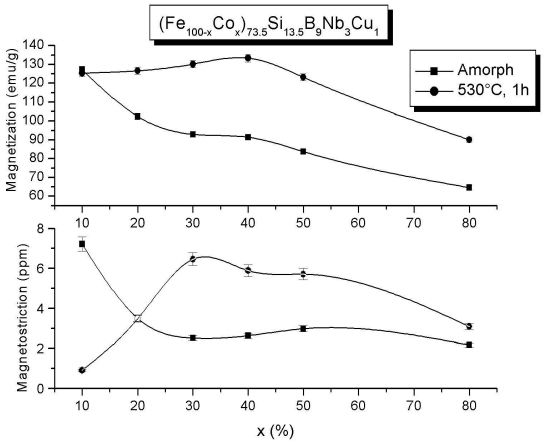

Figure 5.14: Influence of Co in $(Fe_{100-x}Co_x)_{73.5}Si_{13.5}Nb_3B_9Cu_1$ alloys for saturation magnetization (top) and magnetostriction (bottom).

dramatic change in the curve which has a maximum around 20-40% which is in line with the well established maximum magnetization around 35% in the Fe-Co system. The evolution of the saturation magnetostriction coefficient in Fig. 5.14 (bottom) is also consistent with what is well established in Fe-Co based metallic glasses.

As it is seen Fig. 5.15, the shape of the hysteresis loops is strongly affected by the Co content. The so called engineering induction measured at 1 kA/m continuously decreases as a function of x due to the higher anisotropy which cancels the benefit of the Co addition on the saturation magnetization (see also in Fig. 5.16). The coercivity plot in Fig. 5.16 exhibits a clear step-up around x=30%. Indeed, the coercive field remains below 10 A/m for the lowest Co concentrations and jumps to 40 A/m.

As it was mentioned in Sec. 5.1 this gap in coercivity above 20% of Co can be understood in terms of the precipitation of a more stable $Fe_{70}Co_{30}$ like compound. Since the anisotropy constant of $Fe_{70}Co_{30}$ like phase is an order of magnitude higher (K_1= 100 $\frac{kJ}{m^3}$) than the Co free alloy ($Fe_{80}Si_{20}$ phase, K_1= 8 $\frac{kJ}{m^3}$), thus it gives a rise of coercivity considering from the RAM model ($H_c \sim K_1^4$).

Moreover, it is clear that the high Co content promotes the formation of aggregates as observed by TEM. The twin crystals in the aggregates should be weakly disoriented in order to minimize the interfacial energy. Consequently, the effective anisotropy (as deduced from the random anisotropy model) should no longer depend on the crystal size but on that of aggregates and would impede the coercivity to be suppressed. Additionally, in a recent work [78], it was pointed out that the coercivity depends not on the average grain-size but the distribution of the grain-size, namely the longer the width of grain size distribution the higher the measured coercivity, even the mean grain size is constant. This fact also can effect the coercivity, since the width of distribution is found to be increased by Co addition (see Fig. 5.4).

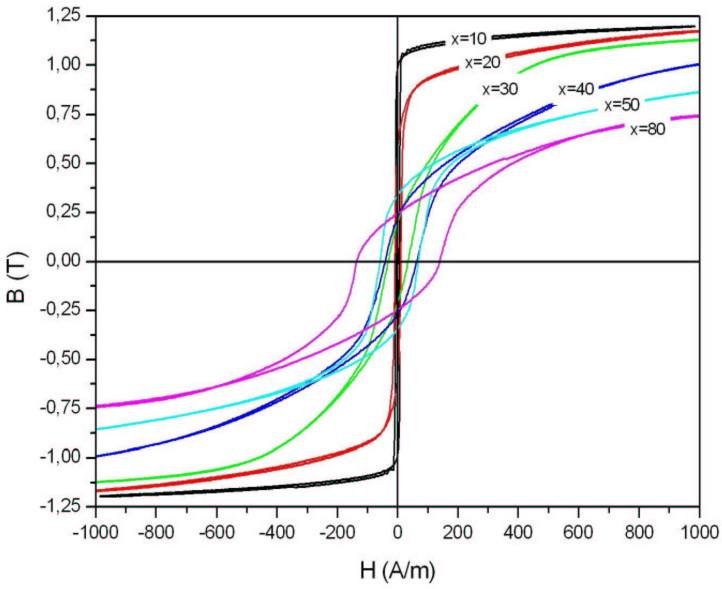

Figure 5.15: Hysteresis loops of $(Fe_{100-x}Co_x)_{73.5}Si_{13.5}Nb_3B_9Cu_1$samples annealed at 530°C/1 h.

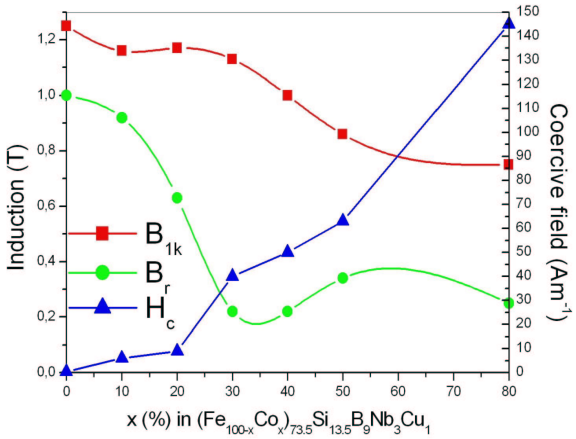

Figure 5.16: Dependence upon Co content of maximum induction, remanent induction and coercive field recorded under a maximum field of 1 kA/m ($T_a = 530°C$, 1hour).

5.2.2 $(Fe_{100-x}Co_x)_{78}Si_9Nb_3B_9Cu_1$

Magnetic saturation as a function of Co content obtained by VSM is shown in Fig. 5.17 (top). Results reflect that magnetic saturation of as-quenched material decreases continuously from 158 emu/g (x=0) down to 88 emu/g (x=95). Interestingly in $(Fe_{100-x}Co_x)_{73.5}Si_{13.5}Nb_3B_9Cu_1$ alloys constant or even slight increase of σ was experienced for $x \leq 40$ (see in Fig. 5.14). As for nanocrystalline samples, the magnetic saturation also decreases continuously similarly to that of amorphous alloys.

The evolution of the saturation magnetostriction coefficient in Fig. 5.17 (bottom) lower with x for as-cast amorphous alloys, while for nanocrystallized samples it shows a discrete maximum at x=70, which predicts an increase in the coercivity in those samples.

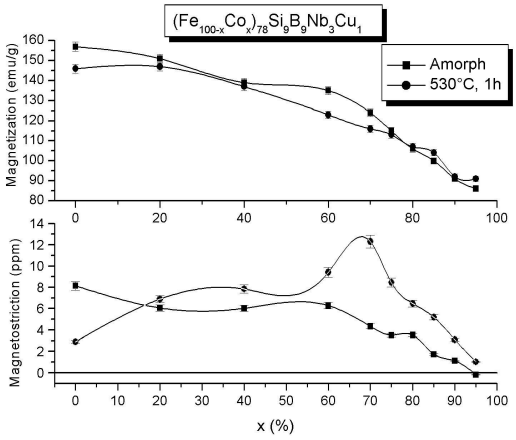

Figure 5.17: Influence of Co in $(Fe_{100-x}Co_x)_{78}Si_9Nb_3B_9Cu_1$ alloys for saturation magnetization (top) and magnetostriction (bottom).

The coercivity plot in Fig. 5.37 (on the right) exhibits a clear step-up above x=70%. The hysteresis properties are discussed with stress/magnetic field annealing results in Sec. 5.4.

5.2.3 $(Fe_{100-x}Co_x)_{84}Nb_{3.5}Zr_{3.5}B_8Cu_1$

The Curie temperature of as-quenched $(Fe_{100-x}Co_x)_{84}Nb_{3.5}Zr_{3.5}B_8Cu_1$ alloys increases with Co addition, namely $T_c^{am} = 243°C$ for x=10 and $T_c^{am} = 365°C$ for x=20. For cases where $x \geq 30$, the first crystallization event (T_{x1}) occurs before the amorphous phase becomes paramagnetic ($T_c > T_{x1}$) and the precipitating Fe-Co nanophase enhances the magnetization, thus the material is always in ferromagnetic state during the annealing treatment. As far as it can be linearly extrapolated from a $\sigma^{1/\beta}$ plot (with $\beta = 0.36$), the Curie point of first crystalline phase exceedingly increased with Co addition. Virtual Curie temperature of precipitated nanophase (FeCo) in $(Fe_{100-x}Co_x)_{84}Nb_{3.5}Zr_{3.5}B_8Cu_1$ alloys deduced from thermomagnetic curves is shown in Fig. 5.18. It is established (see Sec. 5.1), that the precipitated FeCo nanophase changes its lattice structure, from ferromagnetic BCC to paramagnetic FCC at around 1000°C. Therefore these extrapolated values are only virtual for $x > 30\%$, but clearly reflect the high magnetic stability of these alloys against temperature. Saturation magnetization measured by the meaning of VSM plotted in Fig. 5.18 shows that Co addition in these

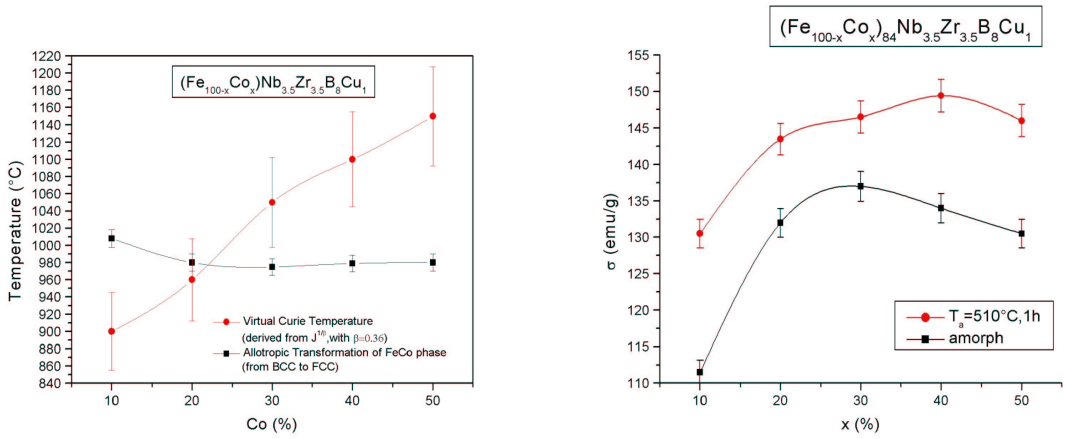

Figure 5.18: On the left: Curie temperature of precipitated nanophase (FeCo) in $(Fe_{100-x}Co_x)_{84}Nb_{3.5}Zr_{3.5}B_8Cu_1$ alloys deducted from thermo-magnetic curves. On the right: Saturation magnetization of $(Fe_{100-x}Co_x)_{84}Nb_{3.5}Zr_{3.5}B_8Cu_1$ amorphous and heat treated samples

alloys increases the magnetic moment per mass volume in both amorphous and nanocrystalline states up to about 50%. These results are in complete accordance with the well known behaviors in microcrystalline FeCo alloys (see for instance in [76]). The coercive field of samples annealed at 510°C for 1 hour increases with Co addition but stays in a relatively low region ($H_c \sim 25 - 50\frac{A}{m}$) (see Fig. 5.19) compared to samples annealed at 600°C for 1 hour ($H_c > 150\frac{A}{m}$) where the ribbons were almost completely nanocrystallized with much higher grain size (as for comparison, see Tab. 5.4 and Tab. 5.5). Interestingly in all Hitperm concerned issues (see for instance in [17]) the annealing temperature was chosen at 600°C 1 hour, which does not seem to be the optimal from magnetic softness point of view, but needed for a higher thermal stability.

5.2.4 Conclusion

From all the investigated Co-based as-quenched alloys bi-phased composite nanomaterial can be obtained after appropriately chosen annealing temperature. We have found by detailed XRD, DSC and Mössbauer structural investigations, that in all 3 Co-doped alloys, the cobalt is partitioned in the nanoprecipitate forming BCC solid solution with a lattice parameter as expected from the usual bulk Iron-Cobalt binary alloys. The DO_3 structure (actually a superlattice of BCC structure) characteristic of the Finemet alloy remained after Co addition in all $(Fe_{100-x}Co_x)_{73.5}Si_{13.5}Nb_3B_9Cu_1$ alloys. This fact assumes that the Co atoms replace the Fe elements only in the nanophase not inflecting the position of Si atoms in the superlattice.

As for higher Co content Finemet type alloys, Fe atoms migrate to crystalline phase, thus almost leaving the residual amorphous matrix without Fe atoms. The relative fraction of Fe atoms in crystalline grains is rather high, which can be explained in terms of amorphous matrix almost exhausted in Fe element, hindering the nanocrystallization process (small amount of crystalline fraction).

In Hitperm type $(Fe_{100-x}Co_x)_{84}Nb_{3.5}Zr_{3.5}B_8Cu_1$ alloys the Curie temperature can be

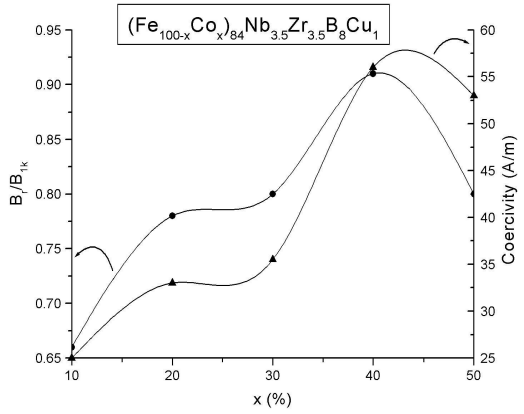

Figure 5.19: Dependence upon Co content of relative induction and coercive field recorded under a maximum field of 1 kA/m ($T_a = 510°C$, 1hour).

increased drastically by Co addition, even this temperature is only virtual for cases where $x \geq 30$, because nonmagnetic phase transition occurs (from BCC to FCC) around 980°C. The higher lattice parameter found in $(Fe_{100-x}Co_x)_{84}Nb_{3.5}Zr_{3.5}B_8Cu_1$ alloys annealed at 510°C for 1 hour ($D \approx 7nm$) as compared to those annealed at 600°C for 1 hour ($D \approx 22nm$) (see in Fig. 5.12) can be understood in terms of soluted presence of Nb, Zr and B elements in the smaller grain size represented nanophase.

5.3 Temperature-time evolution of magnetic properties

ALBEN, BECKER and CHI [38] described the effective magnetic anisotropy energy of the amorphous materials based on the "random walk" statistical considerations and HERZER [4, 39] applied it for nanocrystalline systems. This model has been employed to explain the origin of magnetic softness of various nanocrystalline structures. However, in the originally proposed random anisotropy model only single-phase system is explained, thus various magnetic behaviors which come from the two-phase nature cannot be interpreted. Magnetic hardening at the initial stage of nanocrystallization and the decay of exchange interaction in the intergranular amorphous region near the T_C^{am} of amorphous interphase were explained in the frame of an extended model proposed by HERNANDO [41]. However, this modified model can interpret the latter problems, but it failed to describe the magnetic hardening with temperature forward T_C^{am}, which is the case for Nanoperm alloys. The lack of this model was solved by SUZUKI et. al. [43], who deduced the effective anisotropy taking into account the different exchange stiffness of amorphous and nanocrystalline phases (see Eq. 3.16). This improved model has also a limitation: when the amorphous phase becomes paramagnetic, thus $A_{am} = 0$, the above mentioned equation results in infinitive value. In order to clear up this singularity above T_C^{am}, Varga et al. [3] induced a new parameter taking into account the dipolar interaction between the developing ferromagnetic nanograins as individual magnetic moments in the paramagnetic residual matrix (see in more detail in Sec. 3.2.4). In situ hysteresis measurements during the annealing procedure which is carried out above the Curie temperature of the amorphous phase ($A_{am} = 0$) can bring new evidences of the correctness of proposed theory. Moreover, we are analyzing evolution of coercivity during the nanocrystallization corresponding to various magnetic states as a function of time ($T_{ann} = const.$).

For this purpose various types of amorphous alloys with different compositions were in situ measured. The details of investigation method are discussed in Sec. 4.7. Cobalt modified Finemet type $(Fe_{100-x}Co_x)_{73.5}Si_{13.5}Nb_3B_9Cu_1$ (x=10,20,30,40,50 and 80) alloys where the precipitated nanophase is FeCoSi, compared with Hitperm type $(Fe_{100-x}Co_x)_{84}Nb_{3.5}Zr_{3.5}B_8Cu_1$, (x=10,20,30,40 and 50) alloys with FeCo nanoprecipitation were annealed and in situ measured.

Additionally, investigations on alloys with similar but copper free ($Fe_{59}Co_{25}Nb_7B_9$ and $Fe_{67}Co_{17}Nb_7B_9$) and copper doped ($Fe_{58}Co_{25}Nb_7B_9Cu_1$ and $Fe_{60}Co_{25}Nb_6B_8Cu_1$) compositions were also carried out.

5.3.1 Results

Fig. 5.20a,b show the results of in-situ measurements acquired from amorphous $(Fe_{100-x}Co_x)_{73.5}Si_{13.5}Nb_3B_9C$ during the annealing treatment. On the top, the magnetic saturation as a function of annealing time is seen, whereas on the bottom, the evolution of coercivity with time is plotted. The coercivity results show very different behaviors with composition, a decrease in coercivity with increasing temperature can be observed for all the as-quenched state alloys, which is a consequence of the diminishing K_1 value and the thermal relaxation of internal stress. Paramagnetic state of the amorphous material is indicated by the disappearing of both magnetic saturation and coercivity. No more exchange interaction is present, which can force the magnetic moment of atoms for collective movement. Further sample heating brings on the nanocrystallization with a moderated but continuous increase in coercivity for alloys where x=10, 30 and 80. This behavior is identical with the results of Co free (x=0) Finemet alloy

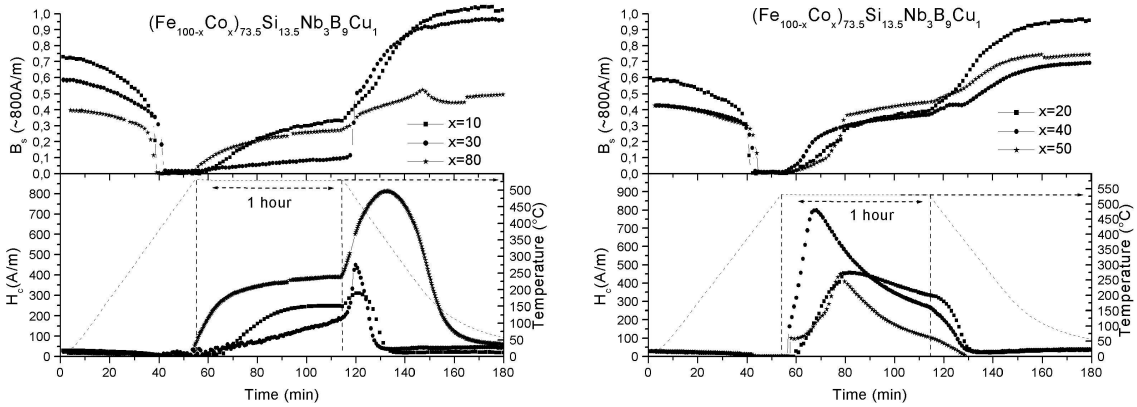

Figure 5.20: a,b Evolution of coercivity and magnetic induction in $(Fe_{100-x}Co_x)_{73.5}Si_{13.5}Nb_3B_9Cu_1$ (x=10, 20, 30, 40, 50 and 80) alloys.

as it was previously reported in [79]. When the end of isothermal annealing is reached and temperature falls, further increase in coercivity gathers pace and only (far) below the isothermal annealing temperature ($\sim 470°C$ for x=10 and $\sim 325°C$ for x=80) it drops, exhibiting a peak in coercivity. As for alloys with x=20, 40 and 50 a continuous increase of coercivity followed by a persistent decrease was found during the 1 hour isothermal annealing period, while magnetic saturation augments moderately with annealing time.

Results collected from the Hitperm type $(Fe_{100-x}Co_x)_{84}Nb_{3.5}Zr_{3.5}B_8Cu_1$ alloys also show two well-distinguished behaviours of coercivity during annealing, plotted in Fig. 5.21. Hitperm type alloys with x=10, 20 and 30 show a sharp increase in coercivity in the beginning of nanocrystallization followed by a continuous descending part similarly to the previous $(Fe_{100-x}Co_x)_{73.5}Si_{13.5}Nb_3B_9Cu_1$ samples with x=20, 40 and 50. This behavior is not observed for the higher cobalt content alloys (x=40 and 50), where coercivity increases only slightly supposing that the whole nanocrystalline-interfacial amorphous ferromagnetic system remained coupled during crystallization.

The third group of similar composition samples with ($Fe_{58}Co_{25}Nb_7B_9Cu_1$, $Fe_{60}Co_{25}Nb_6B_8Cu_1$) and without ($Fe_{59}Co_{25}Nb_7B_9$, $Fe_{67}Co_{17}Nb_7B_9$) copper alloying element exhibits very similar behavior (see Fig. 5.22). Evolution of magnetic saturation increases strongly in the first few minutes of isothermal annealing supposing a very fast crystallization process and a simultaneously sharp increase in coercivity is observed in both Cu-free and Cu-added alloys. In situ synchrotron (SAXS and WAXS) investigations, made in Grenoble (ESRF) by S. N. Kane PhD, pointed out that, this very fast increase in crystalline fraction is only an artifact due to the insufficient applied magnetic field ($\sim 1kAm^{-1}$) to saturate the material.

5.3.2 Discussion

There is a large set of magnetic and structural parameters on which the measured magnetic behavior depends such as A_{am}, A_{cryst}, K_1, D, T_C^{am}, T_{Ccryst}, T_B, etc. during thermal treatment. Reviewing the results obtained from various alloys, two main groups of results offer itself to be defined taking into account the magnetic state of amorphous matrix when crystallization

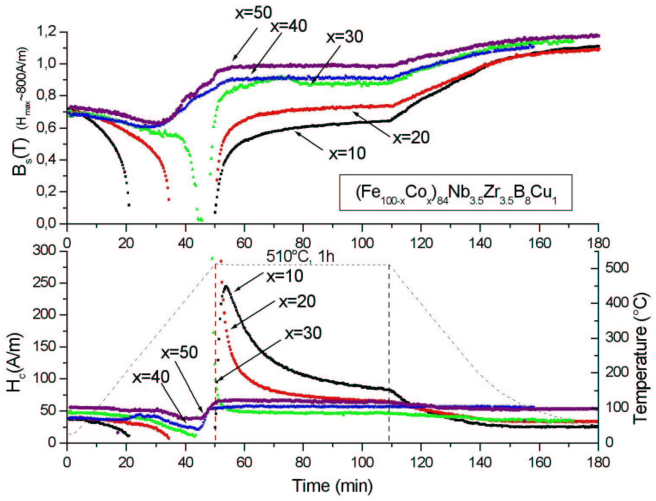

Figure 5.21: Coercive field and magnetic induction as a function of annealing time in $(Fe_{100-x}Co_x)_{84}Nb_{3.5}Zr_{3.5}B_8Cu_1$, where x=10, 20, 30, 40 and 50 alloys.

occurs:

i) $T_{x1} > T_C^{am}$

The as-quenched amorphous precursor is already in paramagnetic state in the temperature of crystallization. Above T_C^{am} the exchange energy, which is responsible for the collective behavior of magnetic moment is overcome by the thermal energy ($\ll k_BT$). When crystallization occurs within that paramagnetic amorphous matrix the precipitating and growing nanograins can be in pure ($H_c = 0$) superparamagnetic (SP) or in blocked (by magnetostatic interaction) superparamagnetic state tending toward a high coercivity presented single-domain (SD) state.

ia) Superparamagnetic state

Non-interacting particle consideration

The crystallization temperature is high enough to disalign the otherwise applied field directed magnetic moments, the particle is in pure superparamagnetic (SP) state.

If one calculates the blocking temperature for *non-interacting* FeSi nanograins in Finemet alloys using Eq. 3.5, it turns out that the nanoparticle has very low T_B. Taking an $Fe_{80}Si_{20}$ particles with $K1 = 8\frac{kJ}{m^3}$ and D=12nm, the T_B is found to be 40K. If the measuring time is also taken into account (37Hz), this blocking temperature is still only $\sim 60K$. In addition, ZENER [80] have shown that the magnetocrystalline anisotropy of a material with cubic symmetry depends on the 10th power of magnetic saturation, thus

$$K_1(T) = K_{10}\left(\frac{J_S(T)}{J_{S0}}\right)^{10}. \tag{5.1}$$

The exact K_1 values of FeCoSi nanograins in the investigated Co-doped Finemet type

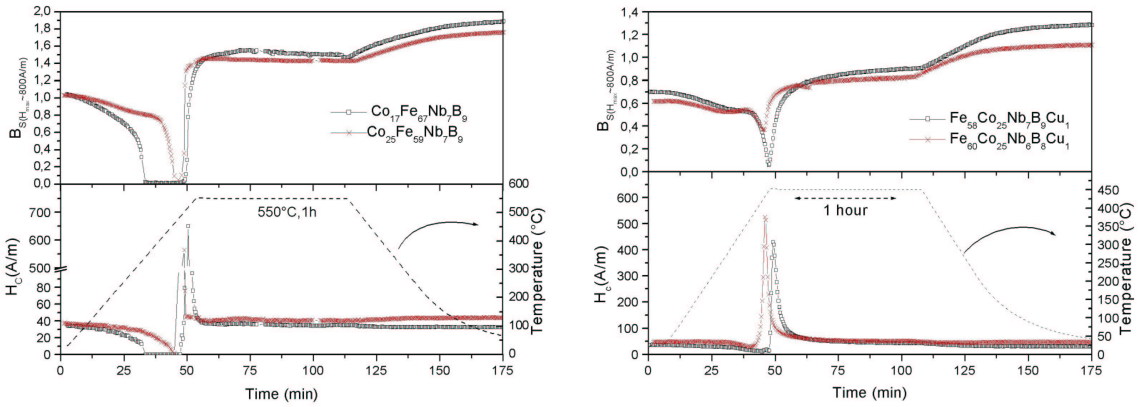

Figure 5.22: On the left (a), evolution of coercivity and magnetic induction of $Fe_{59}Co_{25}Nb_7B_9$ and $Fe_{67}Co_{17}Nb_7B_9$ alloys, on the right (b) same figures for $Fe_{58}Co_{25}Nb_7B_9Cu_1$ and $Fe_{60}Co_{25}Nb_6B_8Cu_1$ alloys.

alloys are unknown, however $\left(\frac{J_S(T_{ann})}{J_{S0}}\right)^{10}$ always results 10^{-4} to 10^{-3} order of magnitude values at the annealing temperature. It reflects that neither very high ($K_{10} \sim 100\frac{kJ}{m^3}$) initial magnetocrystalline anisotropy can be effective in T_{ann}. These calculations suggest that in nanocrystalline magnetic alloys the nanophase is practically always in superparamagnetic state. However samples always show coercivity at the early stage of crystallization, as expected for $(Fe_{100-x}Co_x)_{73.5}Si_{13.5}Nb_3B_9Cu_1$, where x=0 [79], and x=10 (Fig. 5.24,a).

Superparamagnetism in *interacting* particles

In order to solve the conflict between the theoretical deduction and measurements, the nanograins must be considered as *interacting* particles, which means that magnetostatic interaction arises between particles. In latter case pure SP state can be reached if both exchange and dipole-dipole interactions are thermally canceled. If the exchange interaction is not relevant ($T_{x1} > T_C^{am}$), we can assume that the transition is mainly governed by dipole-dipole interactions and the balance between thermal and this magnetostatic energy can calculated as ([81]):

$$T_B = \frac{H_i J_s V^3}{k_B} = \frac{H_i J_s D^3}{6k_B}, \tag{5.2}$$

where H_i internal field depends on the demagnetizing factor (1/3) and the sum of contributions of all dipoles, i.e. Lorentz' field (H_L). Substituting $H_i = \frac{1}{3}H_L = \frac{vJ_s}{9\mu_0}$ into Eq. 5.2, one can write

$$T_B = \frac{\pi v D^3 (J_s^{cryst}(T_{ann}))^2}{54\mu_0 k_B}. \tag{5.3}$$

Structural investigations are made on all in-situ measured samples (see Sec. 5.1), thus values of D and v are known after the annealing treatment, but for appropriate calculations the value of $J_s^{cryst}(T_{ann})$ is to be determined.

The magnetic moment of the two phase system can be calculated as a sum of amorphous

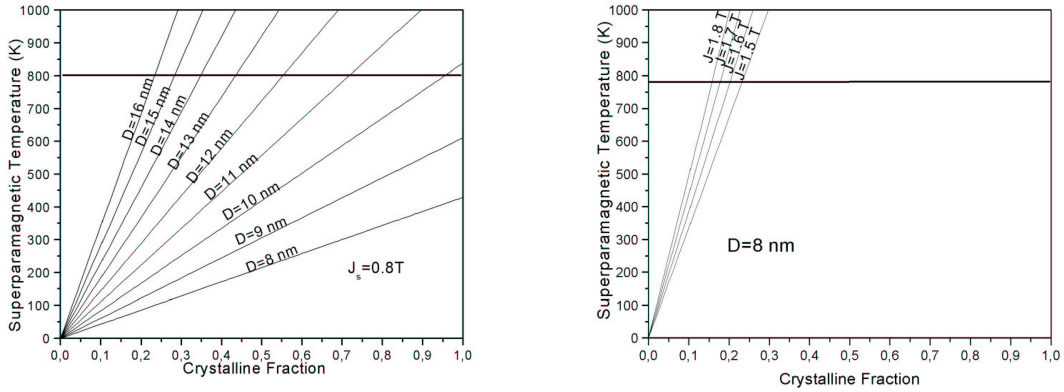

Figure 5.23: a, calculated superparamagnetic transition temperature using Eq. 5.3. On the right (b), same calculations for $(Fe_{100-x}Co_x)_{84}Nb_{3.5}Zr_{3.5}B_8Cu_1$ alloys for different $J_s^{cryst}(T_{ann})$.

and nanocrystalline moments, thus

$$\sigma_{sum} = \upsilon\sigma_{cryst} + (1-\upsilon)\sigma_{am}. \tag{5.4}$$

If the amorphous phase is paramagnetic at the annealing temperature (i.e. $\sigma_{am} = 0$), it can be written as $J_{sum} = J_{cryst} = \mu_0\rho(\upsilon\sigma_{cryst})$ (where ρ is volume density) and in a given temperature (T_{ann}) $\mu_0\rho\sigma_{cryst} = const.$, thus $J_s \sim \upsilon$. This means that the measured magnetic saturation is proportional to the crystallized phase and plotting it with annealing time especially gives information about the evolution of crystallization (kinetics). Later calculations made in this chapter are based on the evolution of crystalline fraction (υ) deduced from the measured magnetic saturation (J_s) results. It must be noted that when the material has high coercivity (in SD state for instance) the applied $\sim 800\ A/m$ magnetic field is not enough to saturate the material, thus the deduced crystalline fraction value is overestimated. $J_s^{cryst}(T_{ann})$ can be deduced by a simple consideration: the magnetic saturation of partially nanocrystallized substance is known at the end of isothermal annealing from in-situ results (let us call it $J_s(\upsilon)$), while the crystallized fraction (υ) is known from X-ray investigations. Now, if the entire material would be nanocrystalline, thus υ=1⇒100%, the magnetic saturation of nanocrystalline phase ($J_s(100\%)$) can be calculated as follows: $\frac{1}{\upsilon} = \frac{J_s(100\%)}{J_s(\upsilon)}$.

Taking the cobalt modified Finemet type $(Fe_{100-x}Co_x)_{73.5}Si_{13.5}Nb_3B_9Cu_1$ (x=10,20,30,40,50 and 80) alloys, the magnetic saturation of that nanocrystalline phase at the annealing temperature ($T_{ann} = 530°C$) is within $0.6T < J_s(T_{ann}) < 1T$ depending on Co addition. A representative calculation for blocking temperatures using Eq. 5.3 as a function of crystallized fraction (υ) with different grain size taking an average, $J_s = 0.8T$ values of precipitated nanophase in T_{ann} is shown in Fig. 5.23a. The continuous horizontal line indicates the annealing temperature (803K) and divides the graph into two regions: below the line the particle is in unblocked SP state whilst above it is in blocked SP state toward to hard SD state. Calculated superparamagnetic transition temperature increases with both nanocrystalline size and fraction assuming that the material is in pure SP state in the beginning of crystallization.

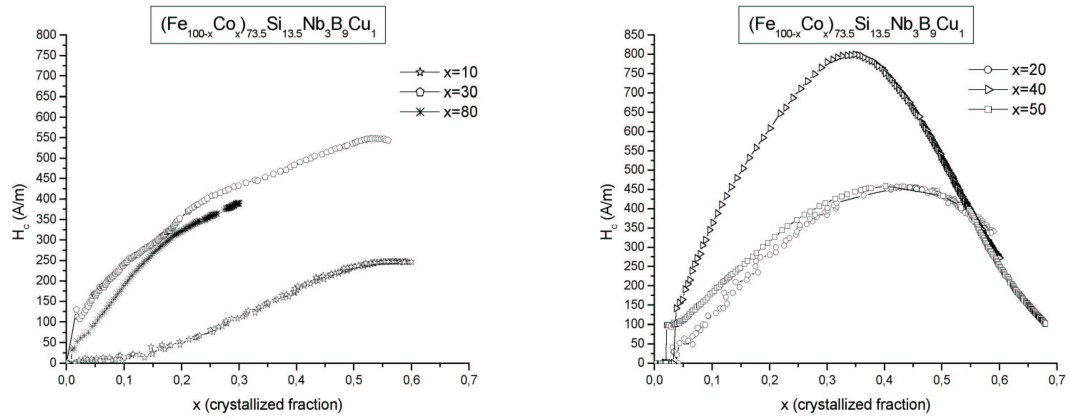

Figure 5.24: a,b. Evolution of coercivity with crystalline fraction of $(Fe_{100-x}Co_x)_{73.5}Si_{13.5}Nb_3B_9Cu_1$ alloys.

With the evolution of crystalline phase and grain growth the superparamagnetic material exceeds T_B and coercivity appears progressively. Unfortunately, SP state with zero coercivity is present when the magnetic saturation is low due to the small amount of crystalline fraction and the inductive method used for investigations requires a minimum ferromagnetic volume for accurate results, thus after heavy digital data processing pure SP state is only observed for x=10.

The reduced coercivity h_c using Eq. 5.3 can be written as

$$h_c = 1 - \sqrt{\frac{T}{T_B}} = 1 - \sqrt{\frac{54\mu_0 k_B T_{ann}}{\pi \upsilon D^3 J_s(T_{ann})^2}}. \tag{5.5}$$

Fig. 5.25 shows the calculated h_c for different D values, taking $J_s(T_{ann}) = 0.6$. Usually, the size of nanograins are considered to be monodisperse (D=const.), however introducing a distribution in grain size, using the results shown in Fig. 5.4 for x=10, the theoretical calculations meet better with measured results (see for comparison in Fig. 5.24a).

All cobalt modified Finemet type $(Fe_{100-x}Co_x)_{73.5}Si_{13.5}Nb_3B_9Cu_1$ (x=10, 20, 30, 40, 50 and 80) alloys reflect the above described blocked superparamagnetic behavior during crystallization at T_{ann} (see Fig. 5.20a, b). As for x=10, 30 and 80 alloys, the coercivity increases moderately with time, i.e. crystalline fraction and grain size, assuming that to align the thermally excited magnetic moment of particles into the direction of applied field is more and more difficult due to the arisen magnetostatic energy of dipolar interaction. The nanograins, which otherwise in *non-interacting* case would be instable, here are close enough to each other to *interact* and block the magnetic moment, thus enhancing the coercivity. Plotting the evolution of coercivity with crystalline fraction in Fig. 5.24a, one can see that coercivity increases moderately from the beginning of crystallization. When temperature falls at the end of isothermal period (1 hour) the coercivity increases exceedingly because of the increase in J_s^{cryst} and K_1 confirming the blocked SP state. Only later on, when temperature is low enough for the nanograins to exchange interact and become coupled, the random anisotropy model can take place, drastically decreasing the coercivity.

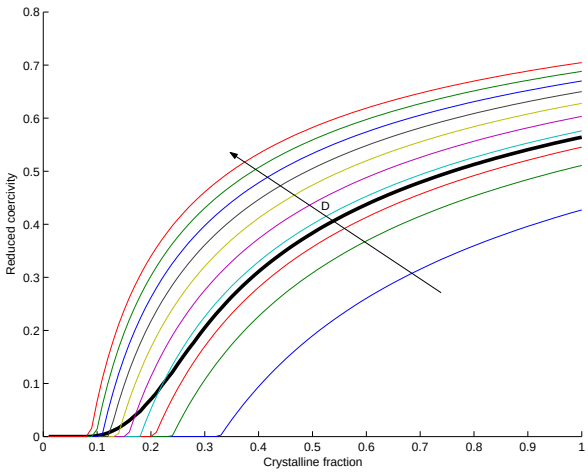

Figure 5.25: Effect of grain size distribution on reduced coercivity as a function of crystalline fraction. Introduced grain size distribution shows better result with measurements (podgy line).

In $(Fe_{100-x}Co_x)_{73.5}Si_{13.5}Nb_3B_9Cu_1$ alloys with x=20,40,50 (Fig. 5.20b), the coercivity rises dynamically with crystalline fraction at T_{ann}, similarly to x=10, 30 and 80. However the further increase of crystalline fraction (see in Fig. 5.24,b), results in smaller and smaller interphase (t) distance between particles, thus they become more and more coupled and the random anisotropy model can be effective in decreasing the coercivity (for interpretation see later in this section). Here the RAM model takes place even during the isothermal annealing period at T_{ann}.

The same behavior is observed for $(Fe_{100-x}Co_x)_{84}Nb_{3.5}Zr_{3.5}B_8Cu_1$ with x=10 alloy, where coercivity rises dynamically with crystalline fraction in the beginning of crystallization (see in Fig. 5.23b)). $J_s^{cryst}(T_{ann})$ value of sample is $\sim 1.5T$, and the calculated blocking temperature (in Fig. 5.23,b) using Eq. 5.3 becomes smaller than the annealing temperature for $v \sim 0.2$, which can explain the transitional behavior.

ib) Single domain state

If the developing particle has high magnetocrystalline and magnetostatic energies, which stand against the thermal energy to fluctuate its magnetic moment, therefore $T_B \gg T_{ann}$ the nanoparticle exhibits high coercivity in the beginning of crystallization. This means that each nanograin has a magnetic moment mostly directed in the easy axis of each individual nanocrystal, thus randomly in the residual matrix. It should be noted that the transition from blocked SP to hard SD state is continuous and depends on the time window of observation.

$J_s^{cryst}(T_{ann})$ values of higher Co containing $(Fe_{100-x}Co_x)_{84}Nb_{3.5}Zr_{3.5}B_8Cu_1$ samples are within $1.5T - 1.8T$, which is not surprising, because it is well established that FeCo crystalline materials exhibit the highest magnetic saturation ($\sim 2.45T$). The calculated T_B values are even higher for small crystalline fraction (v) than T_{ann}, thus no pure SP is present in the higher Co doped samples (Fig. 5.23b). The SD state of nanograins during crystallization is more obvious in $(Fe_{100-x}Co_x)_{84}Nb_{3.5}Zr_{3.5}B_8Cu_1$ alloy with x=20 (see in Fig. 5.21). A very sharp (almost discrete) increase in coercivity is observed, followed by a continuous diminishing

where RAM is valid (this part is discussed later in this chapter).

$Fe_{67}Co_{17}Nb_7B_9$ must also be included in this group, where the precipitation of FeCo nanocrystalline causes a sharp uprise in coercivity, indicating the hard SD state at the early stage of crystallization from paramagnetic precursor (see in Fig. 5.22a).

ii) $T_{x1} < T_C^{am}$

In the first crystallization temperature (T_{x1}) the as-quenched amorphous precursor is still in exchange-coupled ferromagnetic state. The case ia), where the nanoparticles are in superparamagnetic state during the crystallization process, is not valid if $T_{x1} < T_C^{am}$. This is because the nanograin is surrounded by a ferromagnetic substance which will polarize the particle, so the intrinsicly SP nanograin becomes stable. Therefore, if the precipitation and growth happen from the ferromagnetic matrix the following scenarios can be considered:

iia) Single domain state

Similar to case ib), the nanograins show SD behavior, increasing drastically the coercivity from the very beginning of crystallization. The evolution of coercivity with crystalline fraction during the 1 hour isothermal annealing of $(Fe_{100-x}Co_x)_{84}Nb_{3.5}Zr_{3.5}B_8Cu_1$ alloys is demonstrated in Fig. 5.26. For alloy x=30, the uprise in coercivity happens when v is still practically zero, which assumes that the precipitating nanograins are in hard SD state in the very beginning of crystallization, skipping over completely the superparamagnetic transition. Here the magnetostatic energy of FeCo nanocrystallits (high $J_s(T_{ann})$ in Eq. 5.3) is high enough to overcome the thermal energy keeping the magnetic moment (mostly) in the direction of K_1. In Fig. 5.21, the phenomenon is followed by a sharp decrease in coercivity, correspondingly to case ib). Further concerned samples are the $Fe_{59}Co_{25}Nb_7B_9$ (Fig. 5.22a), and both copper doped $Fe_{58}Co_{25}Nb_7B_9Cu_1$ and $Fe_{60}Co_{25}Nb_6B_8Cu_1$ alloys in Fig. 5.22b. The analogous magnetic behavior observed in these samples is due to the very close relative amount of Fe and Co element in the as-cast alloys ($(Fe_{100-x}Co_x)_{84}Nb_{3.5}Zr_{3.5}B_8Cu_1$ with x=30 $\Rightarrow$ $Fe_{58.8}Co_{25.2}Nb_{3.5}Zr_{3.5}B_8Cu_1$), which result in the precipitation of Fe_2Co hard magnetic phases. The drop in coercivity is the consequence of RAM, discussed below.

iib) Exchange-coupled RAM state

In all the above discussed nanocrystalline alloys, after the blocked SP and SD magnetic states, with the evolution of crystalline fraction the particles become exchange-coupled and the random anisotropy model can effectively average out the magnetocrystalline anisotropy, thereby drastically decreasing the coercivity.

However in some particular cases, when both the amorphous and the nanophase have high exchange stiffness, therefore $T_C^{am} \gg T_{ann}$ the whole system is exchange-coupled during the entire crystallization process. The later mechanism predicts only moderate increment in coercivity, which is mainly brought about by the higher fraction of precipitating nanocrystalle. Examples for this exchange-coupling crystallization case, are the high Co content (x=40,50) $(Fe_{100-x}Co_x)_{84}Nb_{3.5}Zr_{3.5}B_8Cu_1$ alloys in Fig. 5.21, where the as-cast amorphous phase is far from T_C^{am} and the developing, nearly equiatomic nanograins have the highest known ($A =\sim 2.4 \times 10^{-11}\frac{J}{m^2}$) exchange constant value (for virtual Curie temperatures see in Fig. 5.18). In addition, due to the nearly zero K_1 of nanograin ($\sim Fe_{50}Co_{50}$) [76] the exchange length ($l_k > 50nm$) is far higher than grain size ($\sim$ 8nm).

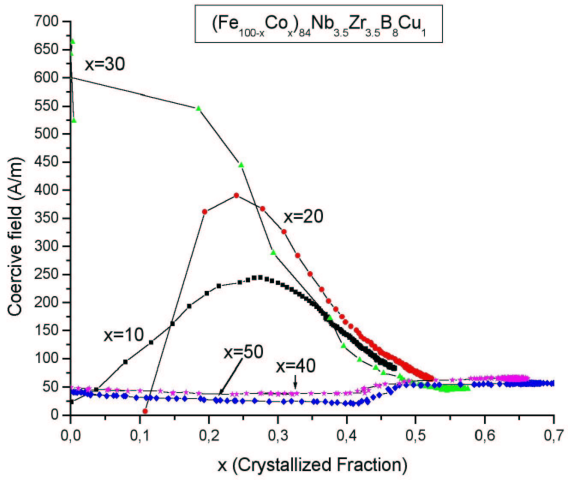

Figure 5.26: Evolution of coercivity with crystalline fraction of $(Fe_{100-x}Co_x)_{84}Nb_{3.5}Zr_{3.5}B_8Cu_1$ alloys.

Dipolar interaction extended two-phase random anisotropy model

The two-phase RAM model, taking into account the different exchange stiffness of amorphous and nanocrystalline phases (see Eq. 3.16, proposed in [43]), predicts an initial increase of K_{eff} during crystallization for alloys where the ratio between the amorphous and nanocrystalline exchange stiffness is $\frac{A_{am}}{A_{cr}} \leq 0.05$. However for cases, where T_C^{am} is much lover than the crystallization temperature, A_{am} is strictly 0, resulting in a singularity in this model.

A new approach, to take into consideration the dipole-dipole interaction between the developing ferromagnetic nanograins in that paramagnetic matrix phase proposed in [3] can solve the lack of this model.

Substituting Eq. 3.15 into Eq. 3.16, the effective anisotropy can be expressed as follows:

$$< K > \approx \frac{1}{\varphi^6} v^4 K_1^4 D^6 \left[\frac{1}{\sqrt{A_{cr}}} + \frac{v^{-1/3} - 1}{\sqrt{A_{am} + A_d}} \right]^6 . \tag{5.6}$$

As it was pointed out by Eq. 5.1 the magnetocrystalline anisotropy (K_1) is not relevant at elevated temperatures. Nevertheless another important effect, which is not considered in HERZER's model must also be taken into account: the shape anisotropy of magnetic particles (K_d).

Shape anisotropy (K_d)

Shape anisotropy can be expressed as

$$K_d = \frac{N_{||} - N_{\perp}}{2\mu_0} J_s (Tann)^2, \tag{5.7}$$

where $N_{||} - N_{\perp}$ is the effective demagnetizing factor ($N_{eff} = N_{||} - N_{\perp}$) for non-spherical nanoparticles. In the theoretical calculations the shape anisotropy of a particle is supposed

to be 0, however the imperfection of the nanograin from spherical shape is uncontested in this scale. The following calculations point out that only a slight distortion of shape can add important contribution for anisotropy.

The demagnetizing factor $N_{\|}$ for ellipsoidal shapes can be approached as

$$N_{\|} = \frac{1}{3}(1 - \frac{4}{5}\varepsilon), \tag{5.8}$$

where $\varepsilon = 1 - \frac{a}{b}$; a and b are the long and short axes of ellipsoidal, respectively. The relations among the demagnetizing factors for different directions of an ellipsoid is $N_x + N_y + N_z = 1$, thus one can write

$$N_{eff} = N_{\|} - N_{\perp} = \frac{3N\| - 1}{2} = -\frac{2}{5}\varepsilon. \tag{5.9}$$

Using Eq. 5.7 and Eq. 5.9, the shape anisotropy is deduced as

$$K_d = -\frac{\varepsilon}{5\mu_0}J_s^2.$$

Thus, the shape anisotropy becomes dominant, if

$$5\mu_0\frac{|K_1|}{J_s^2} < \varepsilon.$$

In our cases $K_1(T_{ann}) \sim 0$, therefore the shape contiribution is the main source of anisotropy in these alloys at T_{ann}. For order of magnitude calculations of K_d, the nanograins were supposed to be slightly ellipsoidal, thus $N_{eff} = 0.02$, which assumes only 2 lattice parameters difference (!) between the long a and short b axis: $N_{eff} = 0.02 = -\frac{2}{5}\varepsilon$ and $\varepsilon = 1 - \frac{a}{b}$, therefore $\frac{a}{b} = 1 - \varepsilon = 1 + \frac{0.02\times5}{2} = 1.05$. It means, if the long axis (a) of nanograin is 10.5 nm, then the short one b is 10 nm, and the shape anisotropy is already a relevant factor at this scale.

Furthermore, taking into account the different magnetic saturation of amorphous and nanocrystalline phases, Eq. 5.7 becomes

$$K_d = \frac{N_{eff}}{2\mu_0}(J_{cr}(T_{ann}) - J_{am}(T_{ann}))^2. \tag{5.10}$$

Simulations

Taking $J_{cr}(T_{ann}) = 0.6T$, $J_{am}(T_{ann}) = 0$ and $N_{eff} = 0.02$ for $(Fe_{100-x}Co_x)_{73.5}Si_{13.5}Nb_3B_9Cu_1$ alloys, $K_d =\sim 2000\frac{J}{m^3}$. Hitperm type (FeCo nanocrystals) alloys have higher $J_{cr}(T_{ann})$ (see above), thus the calculated values of K_d using Eq. 5.10 are mostly in an interval of $10\frac{kJ}{m^3} < K_d < 20\frac{kJ}{m^3}$. Values of K_d are substituted into Eq. 5.6 replacing K_1 for the evaluation of K_{eff}.

Similarly, in $(Fe_{100-x}Co_x)_{73.5}Si_{13.5}Nb_3B_9Cu_1$ alloys with x=20,30,40 and 50 (Fig. 5.20), in $(Fe_{100-x}Co_x)_{84}Nb_{3.5}Zr_{3.5}B_8Cu_1$ alloys with x=10 and 20 (Fig. 5.21), and in $Fe_{67}Co_{17}Nb_7B_9$ (Fig. 5.22a) alloy, the Curie temperature of amorphous precursors is clearly below the first crystallization temperature (T_{x1}), indicated by the passage toward zero magnetization during heating. Thus, in all these samples the exchange stiffness of amorphous phase is strictly zero ($A_{am} = 0$).

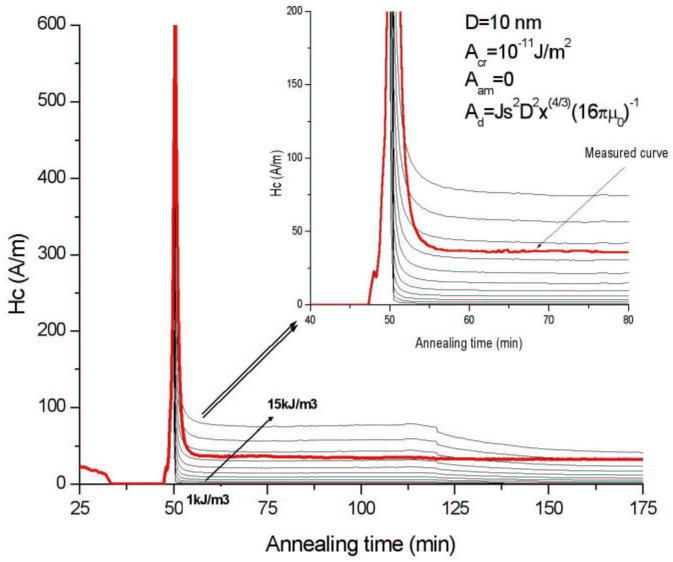

Figure 5.27: Measured coercive field of $Fe_{67}Co_{17}Nb_7B_9$ as a function of annealing time plotted with simulated coercivity results for different K_1 values.

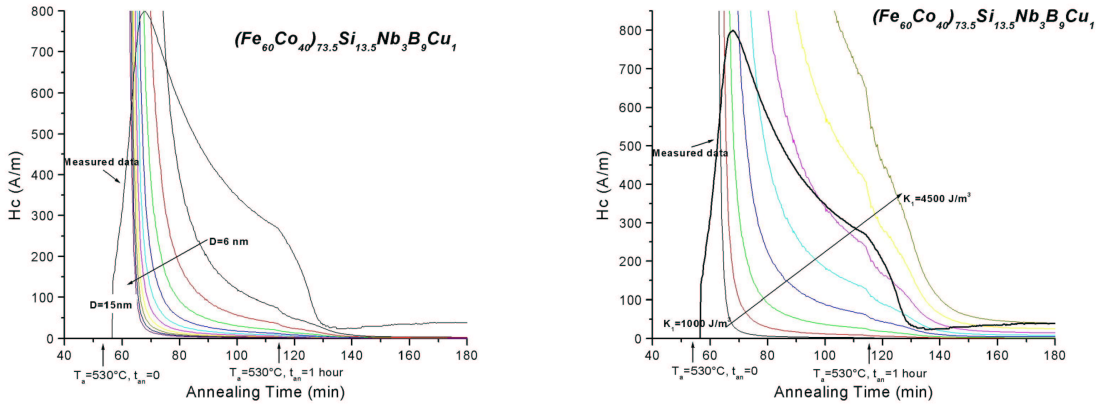

Figure 5.28: a) Simulations made with different D values ($K_1 = 3500 \frac{J}{m^3}$)

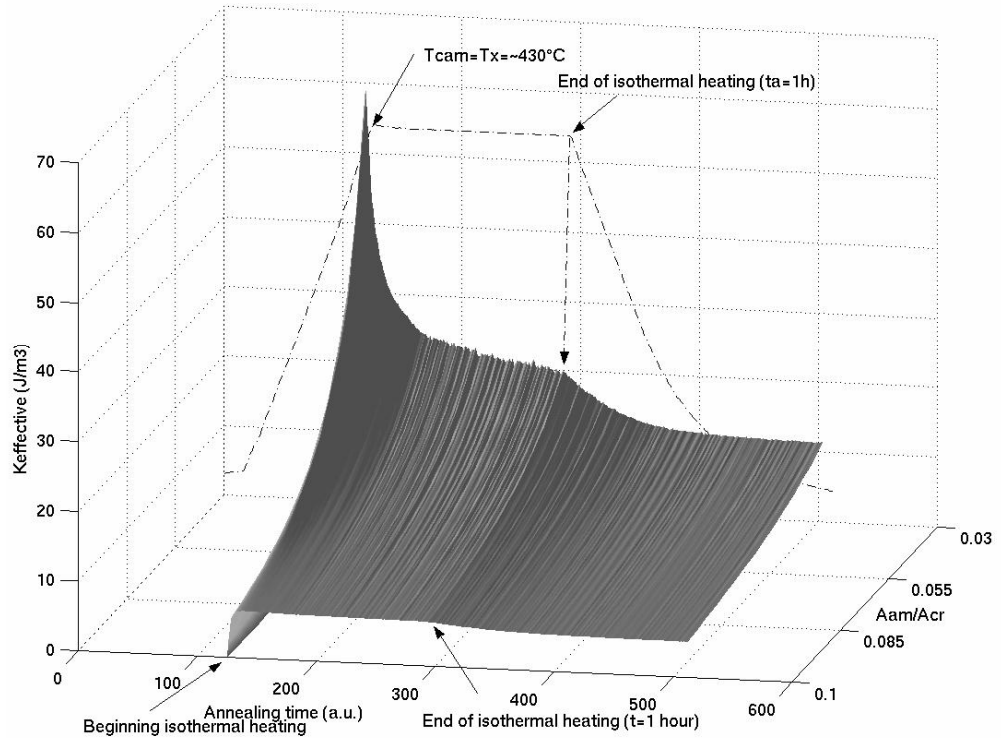

Figure 5.29: Calculated effective anisotropy of $Fe_{60}Co_{25}Nb_6B_8Cu_1$alloy. Crystalline fraction was calculated from J_s. For small $\frac{A_{am}}{A_{cr}}$ ratios, simulations made by Eq. 5.6 shows sharp increase in K_{eff} , therefore in coercivity being in full agreement with measured results.

Calculations made by Eq. 5.6 on $Fe_{67}Co_{17}Nb_7B_9$ (see in Fig. 5.22a) alloy with the parameters of $A_{cryst} = 2.4 \times 10^{-11} \frac{J}{m^2}$, and $D = 10nm$ (obtained from X-ray investigation). The crystallized fraction is calculated from magnetic saturation values knowing that the $v_{final} = 60\%$ at the end of isothermal annealing and only the nanocrystallized phase has magnetic contribution, thus $J_s \propto v$. Fig. 5.27 shows the simulated evolution of coercive field with annealing time (using time dependence of crystallized fraction deduced from magnetic saturation). Since only the order of magnitude of K_1 is known, this parameter was also a variable and was changed from 5 to 15 $\frac{kJ}{m^3}$ by 1.5 $\frac{kJ}{m^3}$ in order to observe its influence. Results obtained from simulation are in good agreement with the in-situ measured data, even though the growth of the magnetic nanograins was not considered in calculations.

The same calculations were made on $(Fe_{60}Co_{40})_{73.5}Si_{13.5}Nb_3B_9Cu_1$ alloy with $A_{cryst} = 10^{-11} \frac{J}{m^2}$, $D = 12nm$ and $v_{final} = 58\%$ known parameters. Coercivity calculated by the dipolar exchange stiffness extended RAM model with different K_1 values (Fig. 5.28b) exhibits similar behaviour as the measured data. The growth of nanograins (D) with time is not taken into account, i.e. we assumed that nucleation is instantaneous, however its inclusion could result in a better fit. The influence of D on K_{eff} is visualized in Fig. 5.28a keeping K_1 at constant 3500 $\frac{J}{m^3}$ value. Results show that with higher grain size the coercive force drops more tendentiously with annealing time.

In several cases where $T_{x1} < T_C^{am}$, the crystallization occurs just below the Curie temperature of amorphous matrix, which assumes a very small but certainly non zero value of A_{am}. Unfortunately this concrete value of A_{am} is unknown, nevertheless approximative calculation is made for $Fe_{60}Co_{25}Nb_6B_8Cu_1$ alloy using Eq. 3.19. Taking the hyperfine fields measured at 298K, which are 35.27 T and 21.89 T for the crystalline phase and for the residual amorphous matrix, respectively [82]. Moreover using $T_{Cam} \sim 723K$, $T_{Ccryst}^{virtual} \sim 1100K$ and the average atomic distance in amorphous ~ 2.55Å, with the lattice parameter of nanocrystalline $a = 2.868$Å, the amorphous-nanocrystalline ratio of exchange stiffness is calculated to be $\frac{A_{am}}{A_{cr}} \sim 0.23$ in room temperature. It is easy to assume that this ratio drastically decreases toward T_{Cam}, where the FeCo nanophase still has high exchange stiffness (A_{cr}) being far from $T_{Ccryst}^{virtual} \sim 1100K$. Effective anisotropy calculations of $Fe_{60}Co_{25}Nb_6B_8Cu_1$ alloy using Eq. 5.6 and taking into account the $\frac{A_{am}}{A_{cr}}$ ratio in an interval from 0 to 0.1 are presented in Fig. 5.29. A drastic initial increase in K_{eff} with annealing time (thus with crystallized fraction, v) followed by continuous decrease is found for $\frac{A_{am}}{A_{cr}} \leq 0.08$. The magnitude of this peak is smaller and smaller for higher $\frac{A_{am}}{A_{cr}}$ values, indicating that for alloys where A_{am} is still relevant ($T_{x1} \ll T_{Cam}$), only moderate increase in coercivity is expected due to completely exchanged coupled behavior. These expectations match with measured coercivity: for alloys (see the related samples in Fig. 5.21 and 5.22) where $T_{x1} \sim T_{Cam}$ or in other words the $\frac{A_{am}}{A_{cr}}$ ratio is small, high initial increase of coercive field is observed, whereas for alloys $(Fe_{100-x}Co_x)_{84}Nb_{3.5}Zr_{3.5}B_8Cu_1$ (x=40 and 50) with high $\frac{A_{am}}{A_{cr}}$ values ($T_{x1} \ll T_C^{am}$) no peak in coercivity is measured during crystallization.

These order of magnitude calculations, taking into account the magnetostatic interaction between developing nanograins within the amorphous matrix, are convincing to assume the importance of dipolar ferromagnetic interaction in these two-phase soft magnetic alloys.

5.3.3 Conclusions

The precipitating nanocrystalline phase can be in different magnetic states during isothermal annealing depending on several parameters. It is dominant whether the amorphous phase is still ferromagnetic or already in paramagnetic state when crystallization occurs.

It was found that at least two cases should be distinguished: (i) $T_{x1} > T_C^{am}$ and (ii) $T_{x1} < T_C^{am}$. For each of the above two cases, we have found subcases depending on the particular values of the K_1, J_s, A and D values of the nanoprecipitate.
Case ia) corresponds to the change of magnetic state from unblocked superparamagnetic ($T_B \geq T_{ann}$) to magnetostatic interaction blocked superparamagnetic ($T_B \leq T_{ann}$) state during nanocrystallization, showing continuous increase in coercivity. Taking into consideration the size distribution of nanograins results in better correspondence with experimental results.
In case ib), the precipitating nanograins are in hard single domain state in the beginning of crystallization skipping over the superparamagnetic phase due to their higher magnetocrystalline K_1 and magnetic saturation J_s values, which produces a sudden jump in coercivity at the first stage of crystallization.
Case iia) corresponds to the non-effective exchange coupling due to the fact that the distance of ferroparticles is larger than the exchange length ($t > l_{ex}$), therefore high coercivity in material is present.
In case iib), the exchange coupling is effective ($t < l_{ex}$) during crystallization, due to the high exchange stiffness of both crystalline (A_{cr}) and amorphous phases (A_{am}) and the low value of magnetocrystalline anisotropy (K_1). Only a slight coercive field increase is found, linked to the higher value of D.

For higher crystalline fraction, the drop in coercivity after the initial increase due to *interacting superparamagnetic* and *single domain* states can be successfully explained by taking into account the dipolar interaction, which resolves the singularity of K_{eff} above T_C^{am} in the two-phase random anisotropy model by the introduction of effective dipolar stiffness A_d. Simulation results are in full agreement with the data measured in situ, bringing further evidence of the softening mechanism proposed in [3] showing that the increasing dipole-dipole interaction between nanograins can efficiently replace the role of exchange interaction in averaging out the local magnetocrystalline anisotropy. This mechanism, however, is only active when the intergranular distance (t) is very small, i.e. $t \approx l_{ex} = 3 - 4nm$.

Furthermore, calculations assume the important contribution of shape anisotropy (K_d) at elevated temperature in these materials.

5.4 Induced magnetic anisotropy

In the first part of this section, a novel method to determine transversal induced magnetic anisotropy with some selected results is discussed. The second part of the section presents the induced magnetic and stress annealed results on the present thesis related samples.

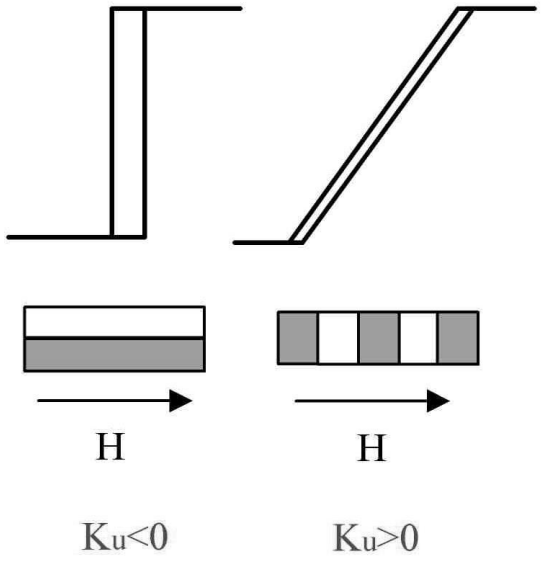

Figure 5.30: Different form of obtained hysteresis loops and corresponding domain structures for cases when induced anisotropy is negative (on left side) and positive (on right side).

In order to determine the magnitude of uniaxial induced magnetic anisotropy (K_u) in a material, two cases must be distinguished (see in Fig. 5.30):

1. If $K_u > 0$, the induced anisotropy is transverse and the hysteresis loop is flatten (F-type). Magnetic energy density (W) stored in the material can be calculated as the area between the hysteresis cycle and vertical (J) axis and the value of K_u can be deduced by different methods presented in Sec. 3.4.

2. For $K_u < 0$ which means that induced anisotropy is longitudinal and the hysteresis loop is squared (Z-type). In the case of longitudinal induced anisotropy, the square hysteresis loop is clearly unsuitable for this evaluation because the magnetization reversal takes place by a single large Barkhausen jump at $\pm H_C$. The coercive force in this case corresponds to the domain wall nucleation energy which is indirectly linked to K_U through the domain wall energy. However many other parameters e.g. surface roughness are involved and finally K_U cannot be deduced from H_C.

5.4.1 A novel method for determining longitudinally induced anisotropy

Isotropic samples

For the purpose of determining K_U when its value is negative, a method originally proposed by Weber et al. [83] was adapted. The sweeping field (H) is applied along the easy axis which

is longitudinal in this case. The hysteresis loop is obtained by integration of the pick-up coil voltage within the same axis. If a transversal bias field (H_B) is applied, the hysteresis loop is slightly flattened until a critical value is reached at which the magnetization switch is shifted at $H_S \pm H_C$ (see Fig. 5.31).

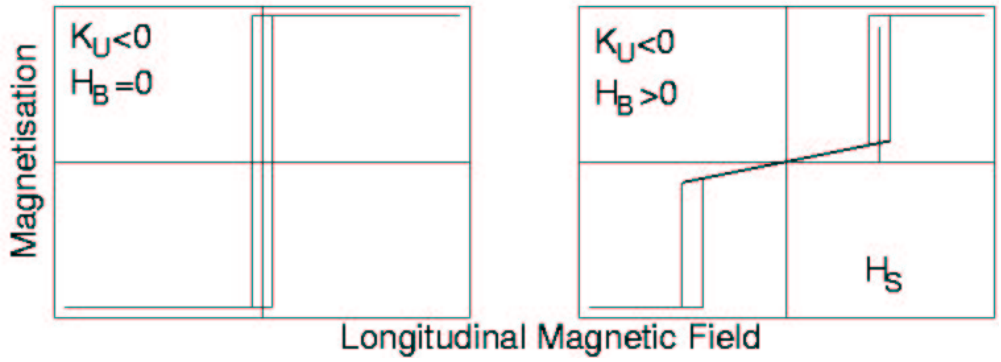

Figure 5.31: For better understanding the method to determinate longitudinally induced anisotropy

The total magnetic energy depends on the angle φ between the magnetization and the measurement direction for a given angle θ between the easy axis and the measurement direction. When two perpendicular fields are applied and the easy axis is parallel to the measurement direction (θ=0), we have:

$$E(\varphi) = K_U \sin^2 \varphi - \mu_0 M_S H \cos \varphi - \mu_0 M_S H_\perp \sin \varphi \tag{5.11}$$

In this case, there is 3 stable positions of the magnetization $\varphi = 0$ and $\varphi = \pm\pi/2$ and the magnetization switches from one position to another (at $H = H_S$) when:

$$E(0) = -\mu_0 M_S H = E(\pi/2) = K_U - \mu_0 M_S H_\perp$$

For a constant $H_\perp$, $E(0) = E(\pi/2)$ so the anisotropy constant is: $K_U = \mu_0 M_S (H_S - H_\perp)$ and the anisotropy field is:

$$H_K = 2(H_S - H_\perp) \tag{5.12}$$

For circular samples with in-plane applied fields, K_U is deduced from a single split hysteresis loop because the demagnetizing factors are equal in both direction ($N_{||} = N_\perp$), so H_K comes from Eq.5.12.

Anisotropic samples

In the case of long samples the longitudinal field is the applied one because of the negligible demagnetizing effect, but the perpendicular inner field is much smaller than the applied bias field: $H_\perp = H_B - N_\perp M_\perp$. The magnetization can be substituted if the field is smaller or equal to the switching field: as there is no domain, permeability is basically due to a rotational magnetization process and thus depends linearly on the field: $M_\perp = \chi H_B$, so

$$H_K = 2[H_S - (1 - N_\perp \chi) H_B] = 2(H_S - \alpha H_B) \tag{5.13}$$

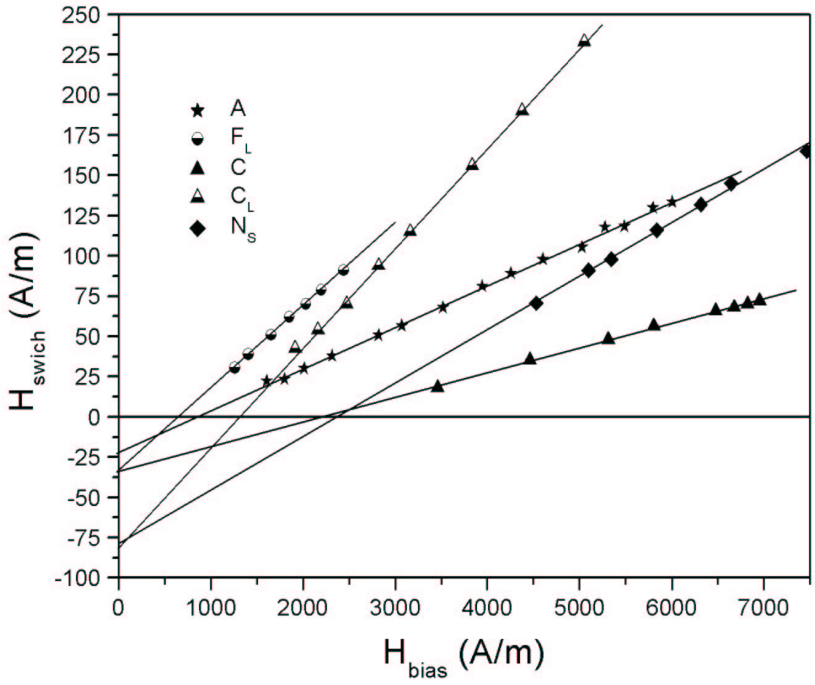

Figure 5.32: The switching fields plotted as a function of bias field. Extrapolation to H_B=0 yields $H_K/2$.

Of course the parameter α is highly dependent on the the demagnetizing factor which cannot be determined for most of the samples with sufficient accuracy. This difficulty is eliminated by using a plotting strategy: several hysteresis loops are recorded with various values of the bias field. The linear plot of H_S as a function of H_B allows the determination of H_K by extrapolation as

$$H_B = 0 \Rightarrow H_K = 2 \cdot H_S(0). \tag{5.14}$$

The experimental set-up is composed of a 0.52 m long solenoid generating the longitudinal sweeping field in the homogeneous part of which the 7 cm long pick up coil and the sample are positioned and a perpendicular 0.3 m in diameter Helmholtz coils set (see Fig. 5.33a). In our case the set of coils is about 35 kg and H_B ($H_{Bmax} = 20kAm^{-1}$) is sufficient only for the amorphous wire sample. (Same coils set was employed to realize transversal field annealing, see for in Fig. 7.5.) The $N_\perp$ demagnetizing factor can be expressed by the geometry of ribbon as $N_\perp \sim \frac{t}{w}$, where t is the thickness and w is the width of sample. Taking a usual thickness value of $t = 20 \times 10^{-6}m$ and the ribbon width's generally scales from $10^{-3}m$ to $10^{-2}m$, therefore the calculated $N_\perp$varies from 2×10^{-3} to 20×10^{-3} , representing an order of magnitude in difference. It means, if $5kAm^{-1}$ field is needed to split the loop, $50kAm^{-1}$ applied field is required.

For cases, where the transversal applied field is sufficient to split the loop, another set-up was used, composed of two perpendicular iron cores (see Fig. 5.33b). This device was already used for magnetostriction measurements by small angle magnetization rotation method [66]. The longitudinal field is known from Ampère's theorem, because $N_{||}$ is strictly zero. On the

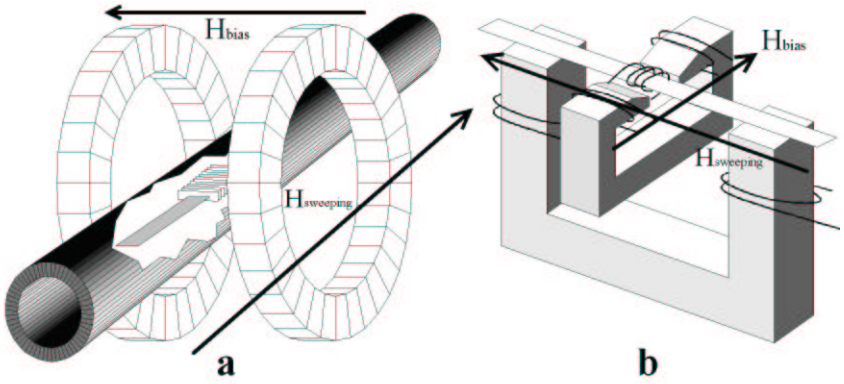

Figure 5.33: Different methods to produce the perpendicular H_B field.

Table 5.8: Anisotropy fields measured by the present technique (except for $K_U > 0$)

Material	Sample	Annealing	H_k(A/m)	J_s(T)	K_u(J/m^3)	H_c(A/m)
$Fe_{77.5}B_{15}Si_{7.5}$ (wire)	A	As-cast	-44±3	1.57	-35±3	19
$Fe_{90}Zr_7B_3$	N_s	Stress	-154±6	1.63	-126±5	36.5
$Fe_{73.5}Si_{13.5}B_9Nb_3Cu_1$	F_L	Longit. H	-66±5	1.24	-41±3	5.5
$(Fe_{90}Co_{10})_{73.5}Si_{13.5}B_9Nb_3Cu_1$	C_L	Longit. H	-158±2	1.16	-92±1	8
$(Fe_{90}Co_{10})_{73.5}Si_{13.5}B_9Nb_3Cu_1$	C_s	Stress	+331±15	1.16	+192±10	13.5
$(Fe_{90}Co_{10})_{73.5}Si_{13.5}B_9Nb_3Cu_1$	C_T	Transver. H	+40±4	1.16	+23±2	5.8

other hand, the perpendicular field ($H_{Bmax} \approx 100kAm^{-1}$) depends strongly on the position of the ribbon in the gap (see for details in [84]). This field, in a given position is $H_\perp = \sigma n I_B/d$, where σ is Hopkinson's leakage coefficient, if the yoke is far from saturation. Eq. 5.13 becomes $H_K = 2(H_S - \alpha' I_B)$, where α' is again eliminated by the plotting of $H_s = f(H_B)$.

Results of applied method on various selected samples

Different type of nanocrystalline alloys were produced and annealed with or without longitudinal (800 A.m^{-1}) fields or under a 100 MPa stress according to Table 5.8. A first important point is to verify the independence of H_S upon the maximum sweeping field H_{max} in particular if the sample is not fully saturated. For this purpose, several loops were recorded with a constant H_B and varying H_{max}. H_S was proved to be independent of H_{max} if the latter is sufficient to cause the switching of the magnetization (Fig. 5.34a). The relevance of this is illustrated in Fig. 5.34b, where it is visible that the samples are not saturated for the largest bias fields. From these split loops, the values of H_S are extracted and plotted as a function of H_B in Fig. 5.32. The perfect alignment of points allows an accurate extrapolation to zero which gives the values of H_K by a least means square linear fit with a remarkably low standard deviation. Table 5.8 summarizes the H_k and K_u values of selected materials.

The anisotropy associated to the single longitudinal core domain of amorphous $Fe_{77.5}B_{15}Si_{7.5}$ was measured with the present method. The result is a quite low value compared to the perpendicular anisotropy associated with the shell suggesting quite a small quenched-in tensile stress in the core (~2 MPa). The stress annealed Nanoperm alloy (N_S) exhibits only a -154 J/m^3 anisotropy which is very low compared to that of Finemet (~+1000 J/m^3) annealed in

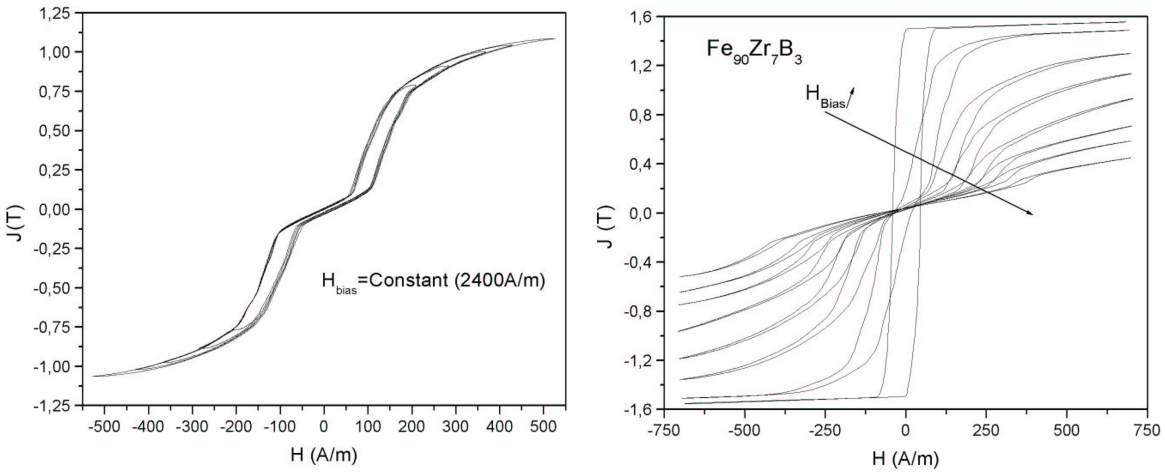

Figure 5.34: On the left (a): The independence of H_S upon the maximum sweeping field H_{max}. On the right (b): the shape of the hysteresis cycle as a function of increasing bias field.

the same conditions. This result suggests a weaker back-stress effect and opens new investigation fields on stress induced anisotropy. Concerning the field annealed materials, the F_L sample exhibits a slightly higher value of K_U compared to transversal field annealing (10-20 J/m^3) [85], which can be explained by a shape contribution to anisotropy.

The coercive fields are also reported in Table 5.8. It is important to note that there is no clear relationship between the magnitude of the anisotropy fields and the coercivity of different materials. For instance, the results obtained with Fe-Co based nanocrystalline alloys suggest that the coercivity is basically linked to the magnetization process (rotation or domain wall displacement) and weekly to the magnitude of induced anisotropy.

In conclusion, Weber's approach [83] has been adapted to the determination of uniaxial magnetic anisotropy in anisotropic samples: the plot of $H_S = f(H_B)$ overcome the demagnetizing effect. This method allows for the first time to measure directly the longitudinal induced anisotropy in amorphous or nanocrystalline ribbons and wires.

5.4.2 Results

The aim of this work is to study the mechanism of long range uniaxial anisotropy (see Sec. 3.3.3) by thermomagnetic and thermomechanical annealing on magnetic properties in the present Co-based alloys. For the purpose of stress and/or longitudinal magnetic field annealing, the horizontal arranged furnace described in Sec. 4.10 was employed, while for transversal field annealing a Helmholtz coil set is used (see in Ch. 7 Fig. 7.5). These investigations are important from an application point of view, i.e. to produce magnetic materials with high saturation and low permeability to store energy in materials such as fly-back converter (the hysteresis shapes required for various applications are summarized in Table 7.2 in Ch. 7).

5.4.2.1 Magnetic field induced anisotropy

The transverse field annealed samples of $(Fe_{100-x}Co_x)_{73.5}Si_{13.5}Nb_3B_9Cu_1$ alloys for which $x \leq 30$ show very similar values compared to samples annealed in longitudinal field (shown in Fig. 5.35). In fact the values are systematically 10-20 J/m^3 smaller (with opposite sign) probably due to a shape contribution. Above x=20, K_U increases quite rapidly and decreases again at 80%.

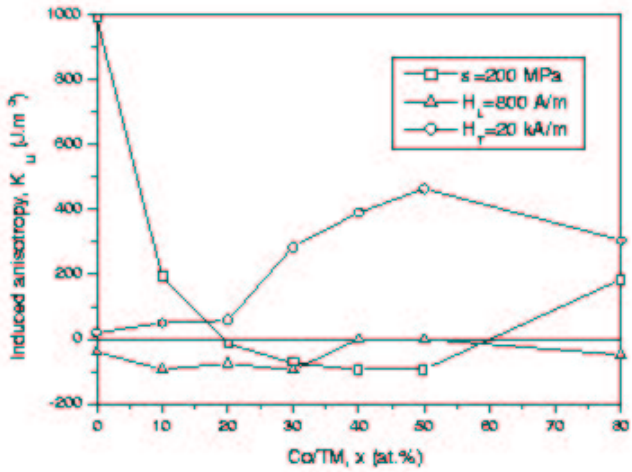

Figure 5.35: Comparison between field and stress anisotropy in $(Fe_{100-x}Co_x)_{73.5}Si_{13.5}B_9Nb_3Cu_1$ alloys.

This situation is quite surprising compared to the results of Yoshizawa [86]. In spite of a sensitively different composition, we should expect a similar behavior in the whole compositional range and not only in the low concentration range (see Fig. 5.36). In order to check this, we have transverse field annealed a series of $(Fe_{100-x}Co_x)_{73.5}Si_9Nb_3B_9Cu_1$ alloy and the results of Yoshizawa was recovered only up to 50% (see some representative hysteresis loop in Fig. 7.2). The huge difference between our measurements and Yoshizawa's is undoubtably explained by the inadequate applied field. In order to be effective, the field applied during annealing must exceed $NM_S(T_A)$ the demagnetizing field at the annealing temperature, a value which is easily reached in the case of low Co samples having a Curie point close to the annealing temperature. This explains why much smaller field are necessary for longitudinal field annealing ($N_\perp \sim 10^{-2} - 10^{-3} \gg N_{||} \sim 10^{-7}$). Indeed, it is clear that the samples with high magnetization and Curie point ($x > 50\%$) are less sensitive to field annealing. As for $(Fe_{100-x}Co_x)_{84}Nb_{3.5}Zr_{3.5}B_8Cu_1$ alloys, no effect of magnetic field annealing was found due to above mentioned reason. Recently, F. Johnson et. al. [87] published induced anisotropy results on FeCo based alloys, but the transversal field applied during annealing was far high (17 T!) as compared to ours.

Squareness ratio of $(Fe_{100-x}Co_x)_{73.5}Si_9Nb_3B_9Cu_1$ samples is efficiently decreased by transversal field annealing, shown in Fig. 5.37. As for the coercivity, it is clearly seen in Fig. 5.37 that transversal magnetic field annealed alloys have lower H_c as compared to reference (applied field free) samples. This behavior can be attributed to the different domain

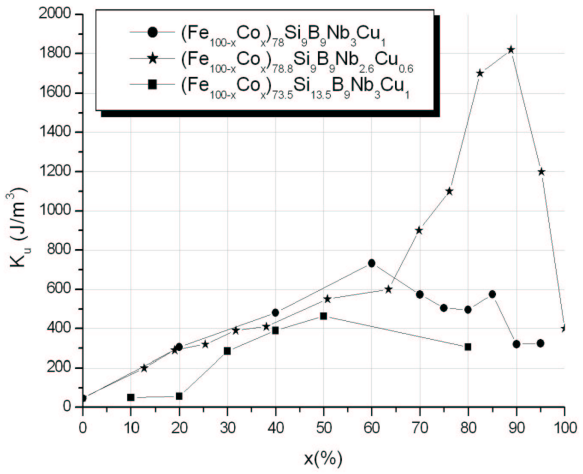

Figure 5.36: Co content dependence of the transversal field induced anisotropy (stars data from [86])

configuration and therefore different magnetization process. In reference samples the domain are longitudinal to the ribbon axes and the dominant magnetization mechanism is the wall motion, whereas in transversal field annealed samples the domains are perpendicular to ribbon axis and magnetization occurs by rotation avoiding wall pinning [88].

5.4.2.2 Stress induced anisotropy

For amorphous alloys, it was found that the easy axis could be either parallel or perpendicular to the tensile stress- annealing axis [89], depending on the sign of the magnetostriction and the heat treatment. For nanocrystalline Finemet ($(Fe_{100-x}Co_x)_{73.5}Si_{13.5}Nb_3B_9Cu_1$, x=0), alloy easy axis perpendicular to the tensile stress is found and the transversally induced anisotropy ($K_u \sim 8000 J/m^3$) [55, 90] is two orders of magnitude higher than that induced by transverse field annealing ($K_u \sim 10 - 40 J/m^3$) [91]. At the present time, two concurrent explanations exist for stress induced anisotropy: the tensile back-stress theory proposed by Herzer [50] and Néel's model of atomic pair ordering adapted by Hofmann and Kronmüller [55]. In order to check these two different theories, not only the present thesis-related Co-added alloys but other nanomaterials with different intrinsic properties were prepared and investigated.

Fig. 5.38 shows the hysteresis loops and the corresponding anisotropy distributions obtained for the nanocrystalline Finemet and for the bulk amorphous $Fe_{62}Nb_8B_{30}$ alloys, respectively. The composition of the remaining amorphous phase in Finemet after annealing at optimal temperature ($v \approx 0.75$) can be approximated as $Fe_{63}Nb_9Si_1B_{27}$ which is very close to the present bulk amorphous alloy (exact composition could not be quenched).

The distribution of anisotropy field is sharp for the reference sample ($\sigma = 0$) and widens and shifts to higher H_k values with increasing applied stress during annealing. The constant slope $\frac{\Delta K_u}{\Delta \sigma}$ is about 8.6 ppm for nanocrystalline Finemet and 2 ppm for bulk amorphous alloy. It must be noted, that typical values of K_u in usual transition metal-metalloid type amorphous alloys are smaller by one order of magnitude [89] similar to the residual amorphous state of

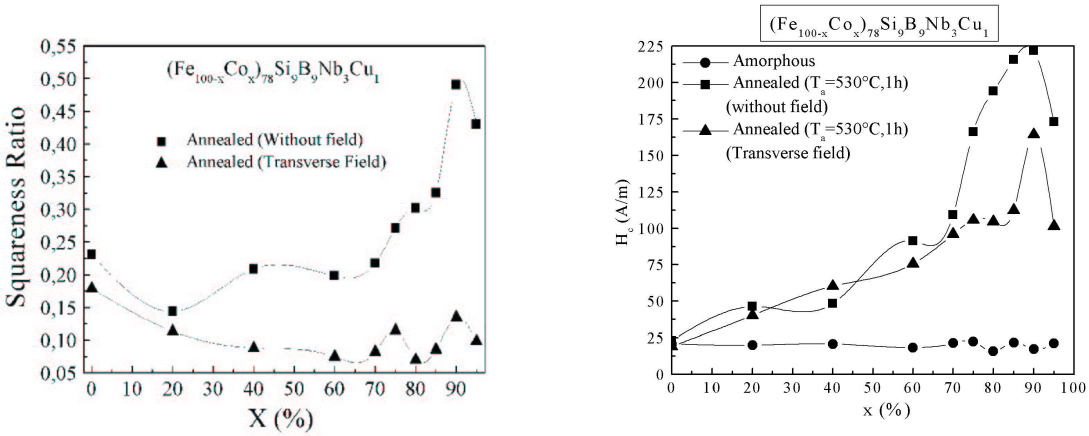

Figure 5.37: Variation of squareness ratio (on the left) and coercive field (on the right) with Co content for with and without magnetic field annealed samples.

Finemet. In order to check if this deviation may be outside the ribbon plane, the intensity ratio between the 2nd and 5th Mössbauer lines ($I_{2,5}$) to 1st and 6th ($\frac{I_{2,5}}{I_{1,6}}$) were investigated (see Eq. 4.8). As shown in Table 5.9, $\frac{I_{2,5}}{I_{1,6}}$ was found to be 3 for as cast amorphous state indicating a preferred orientation parallel to the ribbon plane. With increasing induced anisotropy however, this value steadily decreases, indicating the rotation of magnetization out of plane as it is forced by the distributed induced anisotropy field. For comparison, the reduced half height w/H_k of the anisotropy distributions fitted with a Gaussian function is also represented in Table 5.9. To facilitate the comparison, the results were normalized as (w/H_k)*=3 for the reference sample. Although both methods need heavy digital processing, the reduced width of anisotropy distribution strikingly correlates with the Mössbauer results. This confirms that the widening of the anisotropy distribution indicates the deviation of spontaneous magnetization from the transversal direction.

State	As cast	$\sigma = 0$	$\sigma = 20.5MPa$	$\sigma = 61MPa$	$\sigma = 124MPa$
$I_{2,5}/I_{1,6}$	3	2.88	2.82	2.21	1.70
(w/H_k)*		3	3.1	2.24	1.84

Table 5.9: $I_{2,5}/I_{1,6}$ values set against with reduced width of anisotropy distribution (w/H_k)* for stress annealed (550°C,1h) Finemet.

As for cobalt substituted $(Fe_{100-x}Co_x)_{73.5}Si_{13.5}Nb_3B_9Cu_1$ alloys (see hysteresis loops in Fig. 7.4 in Ch. 7), the value of stress induced transversal anisotropy rapidly diminished and drops to around zero at v=20%. Higher Co concentrations exhibit rather low longitudinal K_U (see for values in Fig. 5.35) up to at least 50% whereas it becomes transversal again for the sample having $v = 80\%$.

Fig. 7.3 shows the effect of stress annealing on Nanoperm ($Fe_{86}Zr_7B_6Cu_1$) and FeCo based Hitperm ($Fe_{44}Co_{44}Zr_7B_4Cu_1$). For all these alloys Z-loops have been obtained after stress annealing, i.e. the induced anisotropy is longitudinal (K_u<0). The negative K_u of

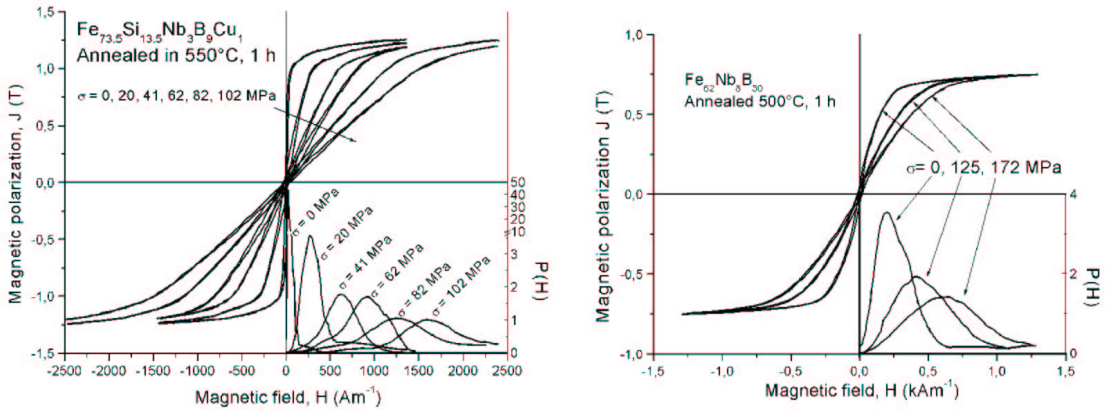

Figure 5.38: Flat hysteresis loops of Finemet (on the left) and $Fe_{62}Nb_8B_{30}$ (close to residual amorphous composition, see on the right) as a function of applied stress during annealing with the corresponding magnetic anisotropy distributions.

Nanoperm cannot be explained by pair ordering (the crystallites being composed of Fe only). Indeed, the creep in Nanoperm was found to be twice that of Finemet at the same temperature and stress [69].

Interpretation of results in the terms of back-stress theory

In order to explain the different response of various type nanocrystalline alloys, induced stress hypothesis was adopted. For single phase amorphous alloys, the shape of stress annealed hysteresis loop can be predicted from the sign of magnetostriction using Eq. 3.3, assuming that the amorphous ribbon is always under compression ($\sigma_a < 0$) after removing the external stress. To interpret the result for two phase systems, Herzer used the magnetostriction coefficient of the nanocrystalline phase (λ_S^{cr}) in this model, which is $\lambda_S^{cr} = -8\times10^{-6}$ for the nanoprecipitate ($Fe_{80}Si_{20}$), therefore the obtained hysteresis is F-type ($K_u > 0$), however in Nanoperm alloys, where $\lambda_S^{cr} = -5\times10^{-6}$ (pure iron is the nanophase) experiments show squared loop after stress annealing.

In order to resolve this contradiction, the induced magneto-elastic anisotropy for the two phase system is considered as

$$K_u = -\frac{3}{2}(v\lambda_S^{cr}\sigma_{cr} + (1-v)\lambda_S^{ac}\sigma_{am}), \tag{5.15}$$

where σ_{cr} and σ_{am} denote the stresses located in the volume fraction of nanograins and amorphous phase, respectively.

In the case of Finemet, one can estimate from XRD the crystal fraction ($v \approx 70\%$) and composition of nanograins ($Fe_{80}Si_{20}$) corresponding to $\lambda_S^{cr} = -8\times10^{-6}$, the composition of the remaining amorphous phase can be approximated as $Fe_{63}Nb_9Si_1B_{27}$ very close to the present bulk amorphous sample ($Fe_{62}Nb_8B_{30}$) for which $\lambda_S^{am} = +10\times10^{-6}$ was measured by means of SAMR.

According to Herzer, the stress induced anisotropy is correlated to the magnetostriction coefficient of the crystals (λ_S^{cr}) but in the case of $(Fe_{100-x}Co_x)_{73.5}Si_{13.5}Nb_3B_9Cu_1$ alloys, it is extremely difficult to evaluate it. In a first step, the magnetostriction of the as-cast

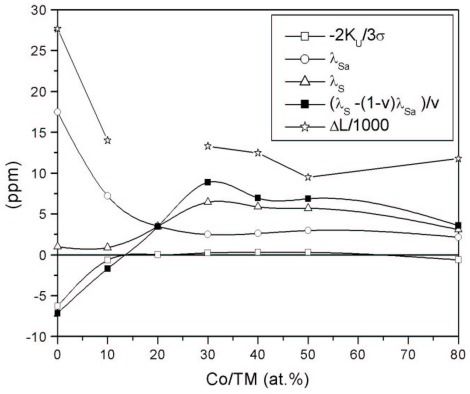

Figure 5.39: Magnetostriction coefficients compared to the reduced anisotropy and the elongation produced by stress annealing in $(Fe_{100-x}Co_x)_{73.5}Si_{13.5}Nb_3B_9Cu_1$ alloys.

material λ_S^{ac} was measured, it decreases continuously with increasing Co content. This was not expected since a low Co substitution in Fe-based amorphous alloys usually yields a sensitive enhancement of it. This may be due to a lack of saturation in the measurement process or to the effect of Nb which modifies the magnetostrictive behavior even at low concentrations. In a second step, the coefficients of the nanocrystallized samples λ_S^{nX} were measured, and λ_S^{cr} was calculated by

$$\lambda_S^{cr} = \left[\lambda_S^{nX} - (1 - v_X)\,\lambda_S^{ac}\right] / v_X \tag{5.16}$$

which has to be taken only as a tendency. After comparison with K_U reduced to the applied stress, $3K_U/2\sigma$, one can observe that the correlation is found quantitatively only for x=0 and 10% and qualitatively up to 50% (see in Fig. 5.39).

In the Hitperm alloy, the nanocrystalline phase is composed of $Fe_{50}Co_{50}$, while the remaining amorphous phase being more or less $Fe_{31}Co_{31}Zr_{24}B_{14}$. Although this composition cannot be melt-spun due to the high Zr content, λ_S^{cr} is so strongly positive ($+65 \times 10^{-6}$) that regardless of the value of λ_S^{ac}, K_u is negative.

The magnetostriction value (λ_S^{nX}) of Nanoperm alloy ($v =\sim 66\%$) after being annealed at 600°C for 1 hour is slightly positive ($+0.2 \times 10^{-6}$ [2]). In these alloys the nanocrystalline phase is pure Fe, which has $\lambda_S^{cr} = +5 \times 10^{-6}$ for applied magnetic fields up to $\sim 40\frac{kA}{m}$, where it changes its sign to negative [76]. However, in these alloys the individual nanograins are saturated within the magnetic domain, therefore the inner magnetic field is much higher than $\sim 40\frac{kA}{m}$, assuming negative sign of magnetostriction ($\lambda_S^{cr} = -5\times10^{-6}$[76]). The magnetostriction of amorphous residual phase calculated by Eq. 5.16 is $\lambda_S^{ac} = +10 \times 10^{-6}$.

The elongation of ribbons ($\Delta\ell$) in Fig. 5.40 (on the left) moderately increases up to the glass transition temperature (T_g). Above T_g the amorphous material is in *supercooled-liquid state* and extends by a viscous flow process up to the crystallization temperature (T_{x1}) at which the process is practically stopped due to the mechanical hard nanophase precipitation (no dislocation in the nanocrystal), the smaller fraction of amorphous and its compositional change. It is found experimentally, that the larger the temperature gap between T_{x1} and T_g

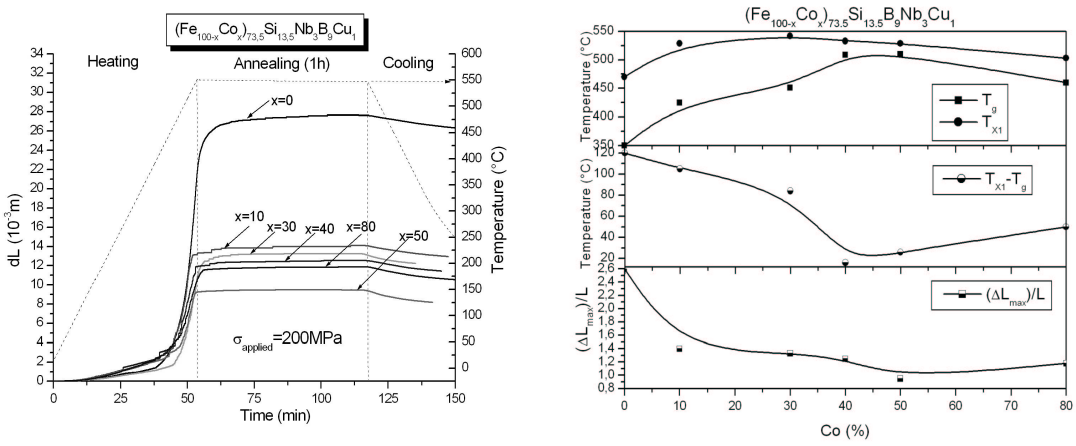

Figure 5.40: On the left: In-situ elongation result of $(Fe_{100-x}Co_x)_{73.5}Si_{13.5}Nb_3B_9Cu_1$ alloys. On the right: Glass transition temperatures (T_g) deduced from elongation measurement (derivative) and maximal change in length ($\Delta\ell_{max}/\ell$) of material during annealing.

the more the elongation of material is observed (see on the right in Fig. 5.40).

Fig. 5.41 (upper box) shows the measured elongation of $Fe_{59}Co_{25}Nb_7B_8$ ribbon at different temperatures as a function of annealing time. (These ribbons were purchased from L. KRAUS's Lab in Czech Republic having a very good quality and a large width ($10mm$), which allowed an increase in the precision of measurement .) The applied stress during heat treatment was $\sigma = 200MPa$. The derivatives of these data (Fig. 5.41 bottom) show a clear raise in $d(\Delta\ell)/dt$ at the same temperature in all cases indicating the glass transition temperature (T_g). The position of $d(\Delta\ell)/dt$ peaks of samples annealed at $500°C$ and at $550°C$ are the same, reflecting the crystallization temperature in the alloy (T_{x1} found to be $\sim 475°C$ with 10°C/min heating rate). As for the sample annealed at $450°C$, it shows continuous increase in change length during isothermal annealing and the peak of the derivative is found at lower temperature, when isothermal temperature is reached ($T_{ann} = 450°C$). This behavior is because at 450°C the elements need longer activation time for crystallization and the break in the speed increase of $\Delta\ell$ is brought on by the temperature, which then became constant and not by the effect of crystallization.

At the end of heat treatment (in room temperature) the stress is unloaded but a compression (σ_a>0) remains in anelastically strained amorphous matrix. At the same time, the non-deformed nanograins within the deformed substance stand against this force, therefore an inner tension (σ_{cr}<0) is created.

Table 5.10 summarizes the predicted effect of stress annealing on the shape of hysteresis (sign of K_U) in various types of nanocrystalline soft magnetic materials taking into account the sign of magnetostriction and forces in both amorphous and nanocrystalline phases by Eq.5.16. For most of the alloys, the amorphous phase and the nanograins have opposite signs of K_U but the crystallized fraction is higher than 50% generally, therefore the crystalline phase is dominant in most alloys. The exception under this behavior the $(Fe_{100-x}Co_x)_{73.5}Si_{13.5}Nb_3B_9Cu_1$ alloy with x=80, where v is only $\sim$ 30% (see Fig. 5.7), thus the induced anisotropy of amorphous phase prevails. The large transverse anisotropy found in $(Fe_{100-x}Co_x)_{73.5}Si_{13.5}Nb_3B_9Cu_1$

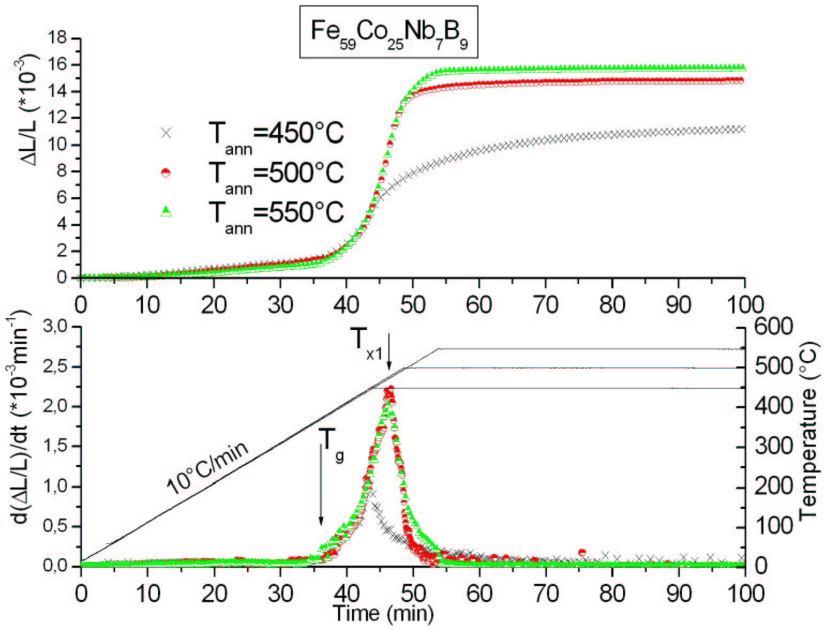

Figure 5.41: On the top: Elongation of $Fe_{59}Co_{25}Nb_7B_8$ ribbon during stress annealing at various temperatures. The applied stress during heat treatment was $\sigma = 200MPa$, respectively. The derivative $d(\Delta\ell)/dt$ (on the bottom) indicates the glass transition (T_g) and crystallization (T_{x1}) temperatures of alloy.

x=0 and x=10 alloys can be attributed to the combination of the same sign of K_U found in the two phases.

Composition	Phases	σ	λ_S	$\sigma\lambda_S$	K_u
$(Fe_{100-x}Co_x)_{73.5}Si_{13.5}Nb_3B_9Cu_1$, x=0	amorphous	-	+	-	
	crystalline	+	-	-	+
$(Fe_{100-x}Co_x)_{73.5}Si_{13.5}Nb_3B_9Cu_1$,x=10	amorphous	-	+	-	
	crystalline	+	-	-	+
$(Fe_{100-x}Co_x)_{73.5}Si_{13.5}Nb_3B_9Cu_1$,x=20	amorphous	-	+	-	
	crystalline	+	+	+*	-
$(Fe_{100-x}Co_x)_{73.5}Si_{13.5}Nb_3B_9Cu_1$,x=30	amorphous	-	+	-	
	crystalline	+	+	+*	-
$(Fe_{100-x}Co_x)_{73.5}Si_{13.5}Nb_3B_9Cu_1$,x=40	amorphous	-	+	-	
	crystalline	+	+	+*	-
$(Fe_{100-x}Co_x)_{73.5}Si_{13.5}Nb_3B_9Cu_1$,x=50	amorphous	-	+	-	
	crystalline	+	+	+*	-
$(Fe_{100-x}Co_x)_{73.5}Si_{13.5}Nb_3B_9Cu_1$,x=80	amorphous	-	+	−*	+
	crystalline	+	+	+	
Hitperm ($Fe_{44}Co_{44}Zr_7B_4Cu_1$)	amorphous	-	+	-	
	crystalline	+	+	+*	-
Nanoperm ($Fe_{86}Zr_7B_6Cu_1$)	amorphous	-	+	-	
	crystalline	+	-	−*	+†

Table 5.10: Expected hysteresis behavior in various stress annealed soft magnetic alloy by back-stress model (Eq.5.16). *Dominant phase. † The model predicts positive induced anisotropy $K_U > 0$, however squared hysteresis loop $K_U < 0$ is found experimentally.

5.4.3 Conclusion

An experimental method was developed in order to measure the longitudinally induced anisotropy. This method allows for the first time direct measurement of the longitudinal induced anisotropy in amorphous or nanocrystalline ribbons and wires.

Coercivity, therefore magnetic loss at low frequency can be lowered by transversal magnetic field annealing. Unfortunately, the applied magnetic field was only effective in inducing high magnetic anisotropy in alloys which have a Curie point close to the annealing temperature, because the field applied during annealing must exceed $NM_S\,(T_A)$ the demagnetizing field at the annealing temperature. Samples with high magnetization and Curie point ($x > 50\%$) are less sensitive to field annealing.

The tensile back-stress model proposed by Herzer in order to explain stress-induced anisotropy is applicable for two-phase nanocrystalline soft magnetic materials, however the diverse response of stress annealed Nanoperm alloy is still unclear. The large transverse anisotropy found in $(Fe_{100-x}Co_x)_{73.5}Si_{13.5}Nb_3B_9Cu_1$ x=0 and x=10 alloys results from a combination of the sign of the magnetostriction coefficients and stresses, adding the contributions of the two phases.

6 Conclusions

This work, conducted in the frame of HiT-Fcore European Commission GROWTH program, includes new results of crystallization process, magnetic properties, induced anisotropy and high temperature behavior of FeCo-based nanocrystalline soft magnetic alloys.

The main result of this thesis are the following:

1. We have found by detailed XRD, DSC and Mössbauer structural investigations, that in all 3 Co-doped alloys, the cobalt is partitioned in the nanoprecipitate, forming BCC solid solution with a lattice parameter as expected from the known bulk Iron-Cobalt binary alloys. The DO_3 structure (a superlattice of BCC structure) characteristic for the Finemet alloy remained after Co addition in all $(Fe_{100-x}Co_x)_{73.5}Si_{13.5}Nb_3B_9Cu_1$ alloys. This fact assumes that the soluting Co atoms replace the Fe elements only in the nanophase not inflecting the position of Si atoms in the superlattice. For high Co content Finemet type alloys, Fe atoms migrate to crystalline phase, thus almost leaving the residual amorphous matrix without Fe atoms. The relative fraction of Fe atoms in crystalline grains is rather high, which can be explained in terms of amorphous matrix almost exhausted in Fe element, hindering the nanocrystallization process (small amount of crystalline fraction). In Hitperm type $(Fe_{100-x}Co_x)_{84}Nb_{3.5}Zr_{3.5}B_8Cu_1$ alloys the Curie temperature can be increased drastically by Co addition, even this temperature is only virtual for cases where $x \geq 30$, because ferromagnetic to paramagnetic phase transition occurs (from BCC to FCC) around 980°C. The higher lattice parameter found in $(Fe_{100-x}Co_x)_{84}Nb_{3.5}Zr_{3.5}B_8Cu_1$ alloys annealed at 510°C for 1 hour ($D \approx 7nm$) as compared to those annealed at 600°C for 1 hour ($D \approx 22nm$) (see in Fig. 5.12) is still unclear, which needs further investigations. However, it could be understood in terms of solute Nb and Zr elements in the nanophase with smaller grain size.

2. Magnetic phase transformations have been followed at the annealing temperature during the nanocrystallization process as a function of time by in-situ hysteresis loop measurements. It was found that at least two cases should be distinguished: (i) $T_{x1} > T_C^{am}$ and (ii) $T_{x1} < T_C^{am}$. For each of the above two cases, we have found subcases depending on the particular values of the K_1, J_s, A and D values of the nanoprecipitate.
   Case ia) corresponds to the change of magnetic state from relaxed superparamagnetism ($T_B \geq T_{ann}$) to magnetostatic interaction blocked superparamagnetic ($T_B \leq T_{ann}$) state during nanocrystallization, showing continuous increase in coercivity. Taking into consideration the size distribution of nanograins, the model matches well experimental results.
   In case ib), the precipitating nanograins are in hard single domain state in the beginning of crystallization skipping over the superparamagnetic phase due to their higher magnetocrystalline K_1 and magnetic saturation J_s values, which produces a sudden jump in

coercivity at the first stage of crystallization.
Case iia) corresponds to the non-effective exchange coupling due to the fact that the distance between ferromagnetic particles is larger than the exchange length ($t > l_{ex}$), therefore high coercivity in material is present.
In case iib), the exchange coupling is effective ($t < l_{ex}$) during crystallization, due to the high exchange stiffness of both crystalline (A_{cr}) and amorphous phases (A_{am}) and the low value of magnetocrystalline anisotropy (K_1). Only slight coercive field increase is found, linked to the higher value of D.

3. For higher crystalline fraction, the drop in coercivity after the initial increase due to *interacting superparamagnetic* and *single domain* states can be successfully explained taking into account the dipolar interactions, which resolves the singularity of K_{eff} above T_C^{am} in the two-phase random anisotropy model by the introduction of effective dipolar stiffness A_d. Simulation results are in full agreement with the data measured in situ, bringing further evidence of the softening mechanism proposed in [3] showing that the increasing dipole-dipole interaction between nanograins can efficiently replace the role of exchange interaction in averaging out the local magnetocrystalline anisotropy. This mechanism, however, is only active when the intergranular distance (t) is very small, i.e. $t \approx l_{ex} = 3 - 4nm$.

4. An experimental method was developed in order to measure the longitudinally induced anisotropy. This method allows for the first time direct measurement of the longitudinal induced anisotropy in amorphous or nanocrystalline ribbons and wires.

5. The tensile back-stress model proposed by HERZER in order to explain stress-induced anisotropy is applicable for two-phase nanocrystalline soft magnetic materials. The large transverse anisotropy found in $(Fe_{100-x}Co_x)_{73.5}Si_{13.5}Nb_3B_9Cu_1$ x=0 and x=10 alloys results from a combination of the sign of magnetostriction coefficients and stresses, adding the contributions of the two phases.

6. The crystallization in a superparamagnetic phase appears as a "sine qua non" (necessary) condition to obtain ultra-soft magnetic properties.
Indirectly, superparamagnetic state during crystallization means that K_1 is sufficiently low to be overcome by the thermal excitation, and, thus to be averaged out (cases of $(Fe_{100-x}Co_x)_{73.5}Si_{13.5}Nb_3B_9Cu_1$, with x=0 and 10).
Directly, strong magnetic interactions at the early stage of crystallization induce preferred direction of local easy axes of particles, nucleating in the course of crystallization process, thus reducing the randomness of local easy axes, which would result in a reduction of the random anisotropy effect (Hitperm type $(Fe_{100-x}Co_x)_{84}Nb_{3.5}Zr_{3.5}B_8Cu_1$ alloys, with x=40 and 50).

The fundamental investigations carried out in these three families of alloys, helped us to select the proper one for applications where the high working frequency and temperature was important:

Applications of stress annealed Finemet based nanocrystalline cores is also developed in SATIE, such as current probe with $I_{max} = 100A$ in the frequency region from 100 Hz to 13 MHz [92], where the size of used tore is reduced by a factor of 30 as compared to ferrites. Prototypes of a 400 W fly-back type converter and forward type converter based of FeCo nanocrystalline tores are currently in progress.

What next?

At the present time the cheap technological method (magnetic field induced anisotropy) is associated with expensive material cost and the cheap raw material (Finemet) cost is associated to the time expensive stress annealing method. Further study should show, which technology is the more favorable from economic point of view. Similar investigations are being undertaken on related Co-doped family of alloys, e.g. Pyroperm composition, in the aim to meet the cheapest material cost with less technological expenses.

7 Appendices

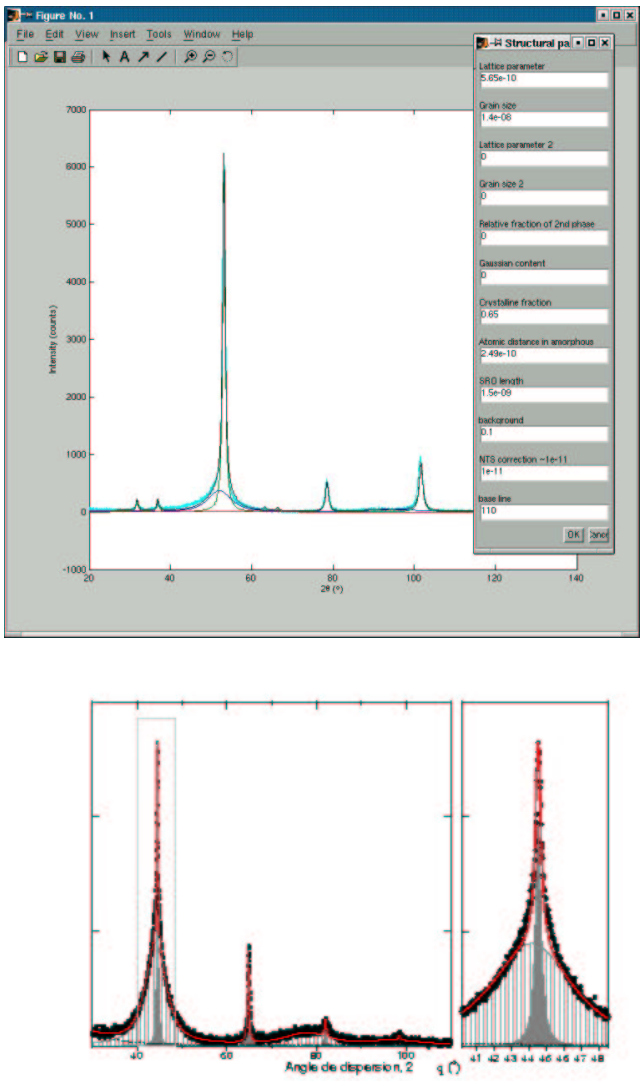

Figure 7.1: Structural parameters from X-ray diffractograms were evaluated using BERTA program [59].

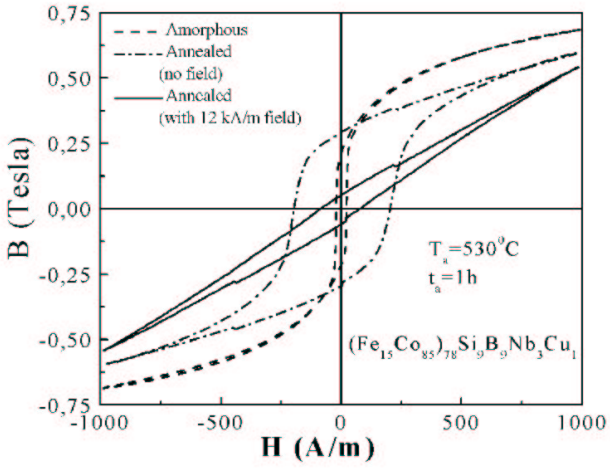

Figure 7.2: Representative hysteresis loops of $(Fe_{15}Co_{85})_{78}Si_9B_9Nb_3Cu_1$ alloy in as-cast state and after annealing with and without transversal magnetic field.

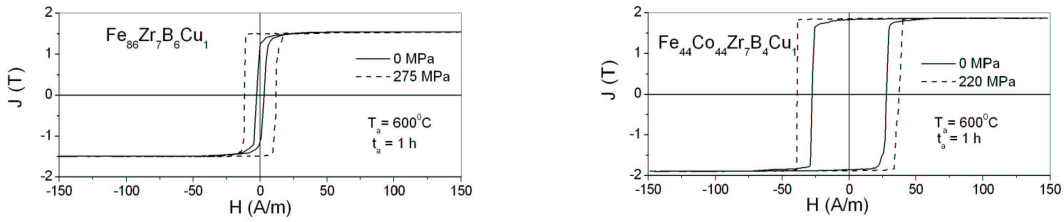

Figure 7.3: Square hysteresis loops of Nanoperm (on the left) and Hitperm (on the right) alloys obtained after stress annealing.

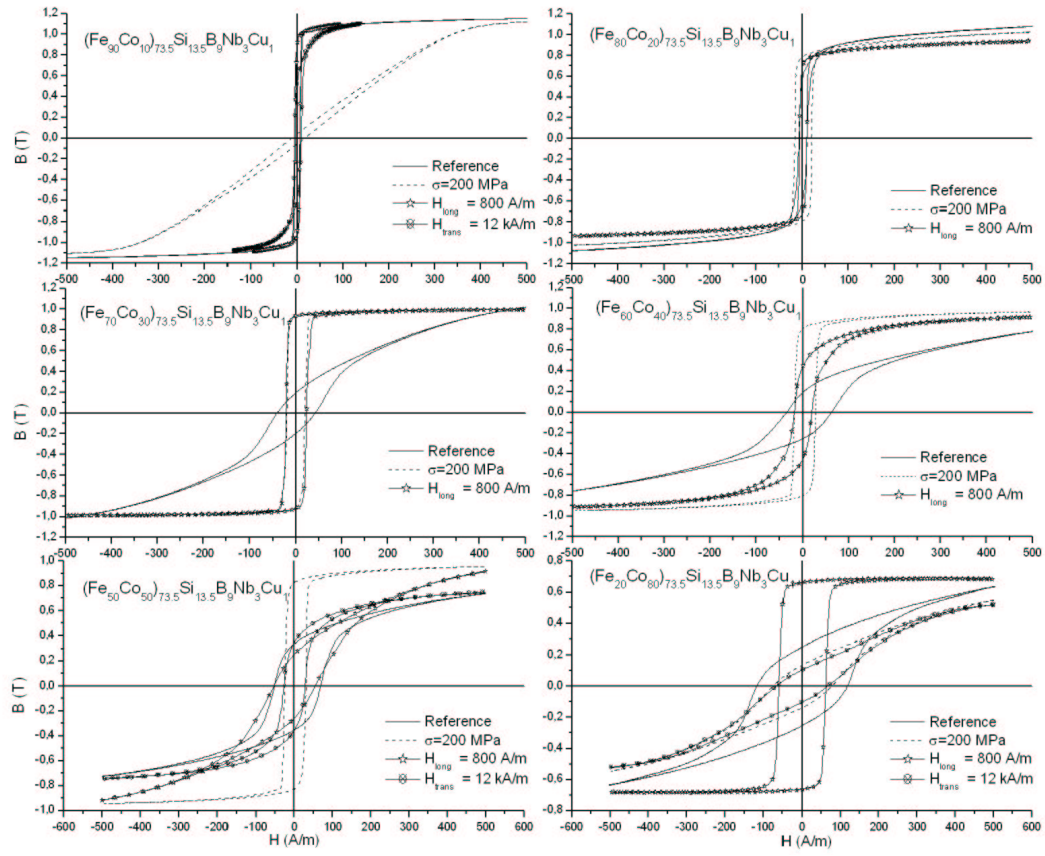

Figure 7.4: Obtained hysteresis loops of stress and magnetic field annealed $(Fe_{100-x}Co_x)_{73.5}Si_{13.5}B_9Nb_3Cu_1$ alloys.

Type of alloy	Original composition	Structure of the nanocrystallized phase	$J_s(T)$	$H_c(A/m)$	$K_1(\frac{kJ}{m^3})$	μ_i	$\lambda_s(\star 10^{-6})$	$T_{c-am}(^\circ C)$	$T_{c-cryst}(^\circ C)$	$T_{x1}(^\circ C)$	$T_{x2}(^\circ C)$
FINEMET	$Fe_{73.5}Si_{13.5}Nb_3B_9Cu_1$	FeSi-BCC, FeSi-DO_3	1.25	0.5-2	8	>100000	2.1	280	630	525	620
NANOPERM	$Fe_{86}Zr_7B_6Cu_1$	Fe-BCC	1.5-1.8	3-10	48	<50000	0.2	392	770	504	747
HITPERM	$Fe_{44}Co_{44}Zr_7B_4Cu_1$	FeCo-BCC, FeCo-B2	1.6-1.8	70-200	~ 7	<2000	8.5	$> T_{x1}$	980	510	700

Table 7.1: Different families of nanocrystalline soft magnetic materials with the most typical chemical composition and with some selected parameters.

Application	Demanded properties
Power transformers	Very low BF losses, very low magnetizing power (X or C)
Broadband transformer	Large band-pass (F)
Flux gate sensor	low H_c, high remanence (Z)
Telecommunication transformers	High initial and max. permeability, large induction (X)
Radio-frequency transformers	Low RF losses, large induction (X,C or F)
Choke coil	High linearity (G or F)
Forward type Switch mode power supplies (SMPS)	Low MF losses, low magnetizing power (X or F)
Fly-back type SMPS	Low MF losses, high induction with low thermal dependence (G)
Magnetic switch	Square loop, low core loss (Z)
Magnetic amplifier	Large excursion of reversible permeability, square loop (Z)
Current transformer	Very high initial permeability, linearity, low coercive field.

Table 7.2: Required magnetic behavior of nanocrystalline soft magnetic materials for various applications.

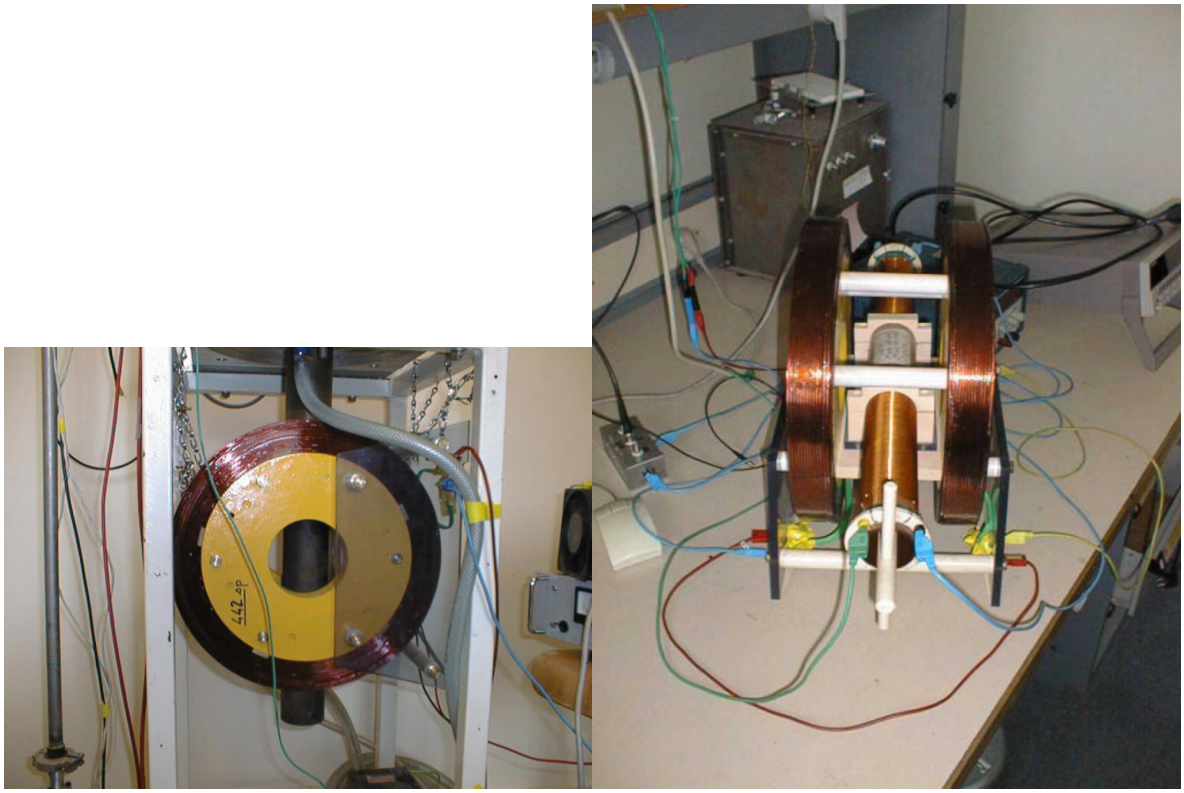

Figure 7.5: Photos of the tubular furnace with Helmholtz coils for transversal magnetic field annealing (on the left). Same attachment was used to determinate longitudinally induced anisotropy in ribbons and amorphous wires (on the right). It can provide continuously a maximum field of 20 kA/m.

Full publication list

1. Stress-induced magnetic anisotropy in nanocrystalline alloys
L. K. Varga, Zs. Gercsi, Gy.Kovacs, A. Kakay and F. Mazaleyrat
J. Magn. Magn. Mater., vol 254-255, pp 477-479, 2003

2. Magnetic and structural study of $(Fe_{1-x}Co_x)_{62}Nb_8B_{30}$ bulk amorphous alloy
Zs. Gercsi, F. Mazaleyrat, S. N. Kane and L.K. Varga
Mater. Sci. and Eng. A, vol 375-377, pp 315-319, 2004

3. Magnetic properties at elevated temperatures of Co substituted Finemet alloys
F. Mazaleyrat, Zs. Gercsi, J. Ferenc, T. Kulik and L. K. Varga
Mater. Sci. and Eng. A, vol 375-377, pp 777-782, 2004

4. Microstructure and magnetic properties of $Fe_{85-x}Co_xNb_5B_8P_2$ high temperature nanocrystalline alloys
L. K. Varga, Gy. Kovacs, A. Kakay, F. Mazaleyrat, Zs. Gercsi, J. Ferenc, E. Fazakas, T. Kulilk and C. Conde
J. Magn. Magn. Mater., vol 272-276, pp 1506-1507, 2004

5. Properties and applications of nanocrystalline alloys from amorphous precursors.
Editors: B. Idzikowski, P. Svec and M. Miglierini
Some specificities of Co-substituted Finemet alloys: Induced anisotropy and magnetic properties at elevated temperatures
F. Mazaleyrat, Zs. Gercsi and L. K. Varga
pp 135-145, 2004

6. A novel method determinig longitudinally induced magnetic anisotropy in amorphous and nanocrystalline materials
F. Mazaleyrat, Zs. Gercsi, L. K. Varga and M. Lécrivain
J. Magn. Magn. Mater., vol 280, pp 391-394, 2004

7. Mössbauer and magnetic studies of $(Fe_{1-x}Co_x)_{62}Nb_8B_{30}$ (x = 0, 33, 50) alloys with wide supercooled region
S. N. Kane, A. Gupta, Zs. Gercsi, F. Mazaleyrat and L. K. Varga
Accepted for publication in J. Magn. Magn. Mater.

8. Influence of composition and thermal treatments on structural, magnetic and magneto-transport properties of $(Fe_{100-x}Co_x)_{78}Si_9Nb_3B_9Cu_1$ alloys
S. N. Kane, F. Mazaleyrat , Zs. Gercsi, D. Rodionov, B. Bernhardt and G. Klingelhöefer
Accepted for publication in J. Magn. Magn. Mater.

9. Study of structural and magnetic studies of $(Fe_{100-x}Co_x)_{78}Si_9Nb_3B_9Cu_1$ alloys
Zs. Gercsi, S. N. Kane, J. M. Grenèche, L. K. Varga and F. Mazaleyrat
Accepted for publication in Physica Status Solidi

Bibliography

[1] Y. Yoshizawa, S. Oguma, and K. Yamauchi, *J. Appl. Phys.*, 1988.

[2] K. Suzuki, M. Kikuchi, A. Makino, A. Inoue, and T. Masumoto, *Materials Transactions, JIM*, 1991.

[3] L. K. Varga and F. Mazaleyrat, *in Properties and Applications of Nanocrystalline Alloys From Amorphous Precursors.* Kluwer Academic Publisher, Dordrecht, 2003, ch. Magnetic Decoupling in Soft Magnetic Nanocrystalline alloys.

[4] G. Herzer, *IEEE Trans. Magn.*, 1989.

[5] K. Suzuki and J. M. Cadogan, *J. Appl. Phys.*, 1999.

[6] R. C. O'Handley, *Modern magnetic materials.* New York: John Wiley and Sons, 2000.

[7] J. Krammer, *Annln. Phys.*, 1934.

[8] A. Brenner and G. Riddell, *J. Res. Natl. Bur. Stand.*, 1946.

[9] P. Duwez, *Trans. Am. Soc. Metals*, 1967.

[10] I. S. Miroshninenko and I. V. Salli, *Ind. Lab.*, 1959.

[11] R. Pond and R. Maddin, *TMS-AIME*, 1969.

[12] A. Gubanov, *Fizika*, 1960.

[13] F. Mazaleyrat and R. Barrué, *in Handbook of Advanced Electronic and Photonic Materials and Devices.* New-York: Academic Press, 2001, ch. Soft Magnetic Amorphous and Nanocrystalline Materials.

[14] H. A. Davies, *in Amorphous Metallic Alloys.* London: Butterworth, 1983, ch. 2. Metallic glass formation.

[15] A. Inoue, *Mater. Trans. JIM*, 1995.

[16] T. Mizushima, A. Makino, and A. Inoue, *IEEE Trans. Magn.*, 1997.

[17] M. E. McHenry, M. A. Willard, and D. E.Laughlin, *Prog. Mat. Sci.*, 1999.

[18] Y. Ogata, Y. Sawada, and T. Miyazaki, *Proceedings of the 4th Conference on Rapidly Quenched Metals*, vol. 2, p. 953, 1981.

[19] K. Suzuki, A. Makino, A. Inoue, and T. Masumoto, *J. Appl. Phys.*, 1991.

[20] M. A. Willard, D. E. Laughlin, M. E. McHenry, D. Thoma, and K. Sickafus, *J. Appl. Phys.*, 1998.

[21] M. A. Willard, M. Q. Huang, D. E. Laughlin, M. E. McHenry, J. Cross, V. G. Harris, and C. Frascetti, *J. Appl. Phys.*, 1999.

[22] H. E. Kissinger, *J. Res. NBS*, 1956.

[23] ——, *Anal. Chem.*, 1957.

[24] M. G. Scott, *in Amorphous Metallic Alloys.* London: Butterworth, 1983, ch. 6. Crystallization.

[25] U. Koster and P. Weiss, *J. Non-cryst. Solids*, 1975.

[26] J. Sestak, *Thermal Analysis : Thermophysical Properties of Solids. Their Measurement and Theoretical Thermal Analysis*, ser. Comprehensive Analytical Chemistry, G. Svehla, Ed. Amsterdam: Elsevier, 1984.

[27] K. Hono, A. Inoue, and T. Sakurai, *Appl. Phys.lett.*, 1991.

[28] K. Hono, K. Hiraga, Q. Wang, A. Inoue, and T. Sakurai, *Acta Metall. Mater.*, 1992.

[29] M. Müller, N. Mattern, and L. Illgen, *J. Mag. Mag. Mater.*, 1992.

[30] T. H. Noh, W. K. Pi, H. J. Kim, and I. K. Kang, *J. Appl. Phys.*, 1991.

[31] T. Kulik, A. Hernando, and M. Vazquez, *J. Mag. Mag. Mater.*, 1994.

[32] Y. Zhang, K. Hono, A. Inoue, and T. Sakurai, *Appl. Phys. Lett.*, 1996.

[33] Y. Zhang, K. Hono, A. Inoue, A. Makino, and T. Sakurai, *Acta Mater*, 1996.

[34] B. D. Cullity, *Introduction to Magnetic Materials.* Addison-Wesley Publishing Company, 1972.

[35] R. Akulov, *Zeits. fur Physik*, 1933.

[36] A. Kàkay, "Numerical investigations of micromagnetic structures," Ph.D. dissertation, Eotvos Lorand University, Budapest, Hungary, 2004.

[37] A. Kàkay and L. K. Varga, *J. Appl. Phys.*, 2004, In Press.

[38] R. Alben, J. J. Becker, and M. C. Chi, *J. Appl. Phys.*, 1978.

[39] G. Herzer, *IEEE Trans. Magn.*, 1990.

[40] R. Yavari and D. Negri, *Nanostruct. Mat.*, 1997.

[41] A. Hernando, M. Vazquez, T. Kulik, and C. Prados, *Phys. Rev. B*, 1995.

[42] T. Kulik and A. Hernando, *J. Magn. Magn. Mater.*, 1994.

[43] K. Suzuki and J. M. Cadogan, *Phys. Rev. B*, no. 5, 1998.

[44] G. Herzer, *Scri. Metall. Mater.*, 1995.

[45] ——, *Mat. Sci. and Eng.*, 1991.

[46] M. Collet and J. P. Delvinquier, *E. P. F.Grenoble*, 1996.

[47] V. Léger, "Contribution à l'élaboration et à la caractérisation de materiaux composites à base de poudres de structure nanocristalline en vue d'application dans le domaine des radiofréquences," Ph.D. dissertation, Ecole Normale Supérieure de Cachan, 1999.

[48] Y. Yoshizawa and K. Yamaguchi, *IEEE Trans. Magn.*, 1989.

[49] ——, *IEEE Trans. Magn.*, 1990.

[50] G. Herzer, *IEEE Trans. Magn.*, 1994.

[51] L. Néel, *J. Phys. Rad.*, 1954.

[52] B. Hofmann, "Spannungsinduzierte magnetische anisotropie in nanokristallinen hochpermeablen leigerungen," Ph.D. dissertation, Max-Planck-Institut für Metallforschung, Institut für Physik, Stuttgart, 1994.

[53] A. A. Glaser, N. M. Kleynerman, V. A. Lukshina, A. P. Patapov, and V. V. Serinkov, *Phys. Met. Metallogr.*, 1991.

[54] M. Ohnuma, K. Hono, T. Yanai, H. Fukunaga, and Y. Yoshizawa, *Appl. Phys. Lett.*, 2003.

[55] B. Hofmann and H. Kronmüller, *J. Magn. Magn. Mater.*, 1996.

[56] L. K. Varga, Z. Gercsi, G. Kovacs, A. Kakay, and F. Mazaleyrat, *J. Magn. Magn. Mater.*, 2003.

[57] J. Barandiaran, A. Hernando, M. Vazquez, J. Gonzalez, and G. Rivero, *IEEE Trans. Magn.*, 1989.

[58] A. Guinier, *X-ray Diffraction.* San Fransisco: W. H. Freeman Comp, 1963.

[59] F. Mazaleyrat, "Basic ex-ray analysis (BERTA) program," ENS de Cachan, Unpublished.

[60] R. L. Mössbauer, *Z. Phys.*, 1958.

[61] L. May, *An Introduction to Mössbauer Spectroscopy.* New York: Plenum Press, 1971.

[62] A. Vértes and D. Nagy, *Mössbauer Spectroscopy of Frozen Solutions.* Budapest: Akadémiai Kiado, 1990.

[63] E. Kuzmann, S. Nagy, and A. Vértes, *Mössbauer Spectroscopy In Chemical Analysis*, ser. Chemical Analysis by Nuclear Methods, Z. B. Alfassi, Ed. John Wiley and Sons Ltd, 1994.

[64] S. Foner, *Review of scientific instruments*, 1959.

[65] J. Moulin, "Elaboration et caractérisation de composites métal-ferrite nanosturcturés, pour applications en moyennes et hautes fréquences," Ph.D. dissertation, Ecole Normale Supérieure de Cachan, 2001.

[66] F. Alves, P. Houée, M. Lécrivain, and F. Mazaleyrat, *J. Appl. Phys.*, 1997.

[67] J.-B. Desmoulins, "Contribution à l'étude de la magnétostriction dans les structures biphasées et des couplages magnétique-thermique-mécanique dans les matériaux nanocristallins de type Finemet, en vue de réalisation de composants inductifs," Ph.D. dissertation, Ecole Normale Supérieure de Cachan, 1999.

[68] "Matlab homepage," *http://www.mathworks.com.*

[69] A. Benchabi, "Contribution à l'optimisation d'un nouveau procédé de recuit rapide de matériaux nanostructuré sous traction pour la réalisation de composants inductifs," Ph.D. dissertation, Ecole Normale Supérieure de Cachan, 2003.

[70] G. Herzer, *J. Magn. Magn. Mater.*, 1992.

[71] C. Gomez-Polo, J. I. Pérez-Landazabal, V. Recarte, J. Campo, P. Marin, M. L. A. Hernando, and M. Vazquez, *Phys. Rev. B*, 2002.

[72] J. Teillet and F. Varret, "MOSFIT program," Le Mans University, Unpublished.

[73] T. Kemény, D. Kaptàs, L. F. Kiss, J. Balogh, L. Bujdoso, J. Gubicza, and I. Vincze, *Appl. Phys. Lett.*, 2000.

[74] J. M. Grenèche and A. Slawska-Waniewska, *J. Magn. Magn. Mater.*, 2000.

[75] J. S. Blazquez, A. Conde, and J. M. Greneche, *Appl. Phys. Lett.*, 2002.

[76] R. Bozorth, *Ferromagnetism*, 3rd ed. New-York: IEEE Press, 1993.

[77] Y. Zhang, J. S. Blazquez, A. Conde, P. J. Warren, and A. Cerezo, *Mater. Sci. Eng. A*, 2003.

[78] T. Bitoh, A. Makino, and A. Inoue, *J. Magn. Magn. Mater.*, 2004.

[79] F. Mazaleyrat, J. C. Faugières, and J. F. Rialland, *J. Magn. Magn. Mater.*, 1996.

[80] C. Zener, *Phys. Rev.*, 1954.

[81] F. Mazaleyrat and L. K. Varga, *IEEE Trans. Magn.*, 2001.

[82] S. N. Kane, "unpublished results."

[83] W. Weber, R. Allensparch, and A. Bischof, *Appl. Phys. Lett.*, 1997.

[84] P. Houée, "Contribution à la mesure du coefficient de magnétostriction de matériaux d'epaisseur micrométrique," *Memoire, Ecole Normale Supérieure de Cachan*, 1996.

[85] G. Herzer, *IEEE*, 1994.

[86] Y. Yoshizawa, S. Fujii, D. H. Ping, M. Ohnuma, and K. Hono, *Scripta Mater*, 2003.

[87] F. Johnson, H. Garmestani, S. Y. Chu, M. E. McHenry, and D. E. Laughlin, "Induced anisotropy in FeCo-based nanocrystalline ferromagnetic alloys (HITPERM) very high filed annealing," *In Press*.

[88] A. Hubert and R. Schafer, *Magnetic Domains*. Springer, 1998.

[89] O. V. Nielsen, L. K. Hansen, A. Hernando, and V. Madurga, *J. Magn. Magn. Mater.*, 1983.

[90] F. Alves, R. Barrué, M. Delage, J. B. Demoulins, N. Lecaude, and J. C. Peron, *Mater. Sci. Forum*, 1999.

[91] A. Lovas, L. F. Kiss, B. Varga, P. Kamasa, I. Balogh, and I. Bakonyi, *J. Phys. IV France*, 1998.

[92] F. Simon, "Contribution à l'étude de nouveaux matériaux nanostructurés, de type (FeCo)SiNbBCu, pour des applications en electronique de puissance, à température élevée de fonctionnement," Ph.D. dissertation, Ecole Normale Supérieure de Cachan, 2004.